Development and Applications of Laminar Optical Tomography for *In Vivo* Imaging

Sean A. Burgess

Submitted in partial fulfillment of the
requirements for the degree of
Doctor of Philosophy
in the Graduate School of Arts and Sciences

COLUMBIA UNIVERSITY
2011

ABSTRACT

Development and Applications of Laminar Optical Tomography for *In Vivo* Imaging

Sean A. Burgess

Laminar optical tomography (LOT) is an optical imaging technique capable of making depth-resolved measurements of absorption and fluorescence contrast in scattering tissue. LOT was first demonstrated in 2004 by Hillman et al [1]. The technique combines a non-contact laser scanning geometry, similar to a low magnification confocal microscope, with the imaging principles of diffuse optical tomography (DOT).

This thesis describes the development and application of a second generation LOT system, which acquires both fluorescence and multi-wavelength measurements simultaneously and is better suited for *in vivo* measurements. Chapter 1 begins by reviewing the interactions of light with tissue that form the foundation of optical imaging. A range of related optical imaging techniques and the basic principles of LOT imaging are then described. In Chapter 2, the development of the new LOT imaging system is described including the implementation of a series of interfaces to allow clinical imaging. System performance is then evaluated on a range of imaging phantoms. Chapter 3 describes two *in vivo* imaging applications explored using the second generation LOT system, first in a clinical setting where skin lesions were imaged, and then in a laboratory setting where LOT imaging was performed on exposed rat cortex. The final chapter provides a brief summary and describes future directions for LOT.

LOT has the potential to find applications in medical diagnostics, surgical guidance, and in-situ monitoring owing to its sensitivity to absorption and fluorescence contrast as well as its ability to provide depth sensitive measures. Optical techniques can characterize blood volume and oxygenation, two important biological parameters, through measurements at different wavelengths. Fluorescence measurements, either from autofluorescence or fluorescent dyes, have shown promise for identifying and analyzing lesions in various epithelial tissues including skin [2, 3], colon [4], esophagus [5, 6], oral mucosa [7, 8], and cervix [9]. The desire to capture these types of measurements with LOT motivated much of the work presented here.

Contents

List of Figures

List of Tables

Acknowledgements

I would like to give my sincerest gratitude to my advisor, Dr. Elizabeth Hillman, for her support throughout my studies. I am grateful that she gave me the opportunity to work in her lab and for the wealth of knowledge she has passed on, both professional and personal. I know that it will serve me well in future endeavors.

I thank the members of my thesis committee, Dr. Andreas Hielscher, Dr. Elisa Konofagou, Dr. Ioannis Kymissis and Dr. Ken Shepard who served as invaluable sources of knowledge during the course of my dissertation.

I owe many thanks to my colleagues and friends in the Laboratory for Functional Optical Imaging. Most, if not all, of this work would not have been possible without your help. I am especially indebted to Brenda Chen who spent countless hours helping with my studies. I may quite literally be in debt to her from our numerous trips the vending machine.

Several people throughout the Columbia community have been instrumental in the success of this research. I thank Dr. Désirée Ratner and her team at the Columbia University Medical Center. They welcomed me into their group and were essential in the collection of clinical data. I thank Keith Yeager who was always willing to help fabricate just about anything out of thin air in the machine shop. I am grateful to Ryan Field - if not for his help designing and building electronic circuits, I would still be soldering.

Most importantly, I would like to thank my family for their love and support. My father's untiring work ethic has always been a source of motivation. My mother has always offered boundless love, including turning her home into a weekend resort for me. I especially would like to thank my older brother, Craig, who has always been my greatest supporter. And of course, I would like to thank my wife, Rachelle. Without her unwavering love and support, this dissertation would not have been possible.

Publications & Presentations Related to the Thesis

Peer Reviewed Publications

- **Burgess, S.A.** and Hillman, E.M.C., *Laminar Optical Tomography*, in *Handbook of Biomedical Optics*, D. Boas, C. Pitris, and N. Ramanujam, Editors. *in press* 2011, Taylor & Francis.

- Chen, B.R., Bouchard, M.B., McCaslin, A.F., **Burgess, S.A**., and Hillman, E.M., *High-speed vascular dynamics of the hemodynamic response.* Neuroimage*,* 54 (2), 1021-1030 (2011).

- **Burgess, S.A.**, Ratner, D., Chen, B.R., and Hillman, E.M.C., *Fiber-optic and articulating arm implementations of laminar optical tomography for clinical applications.* Biomed. Opt. Express, 2010. 1(3): p. 780-790.

- Hillman, E.M.C. and **Burgess, S.A.**, *Sub-millimeter resolution 3D optical imaging of living tissue using laminar optical tomography.* Laser Photon Rev, 2009. 3(1-2): p. 159-179.

- Bouchard, M.B., Chen, B.R., **Burgess, S.A.**, and Hillman, E.M., *Ultra-fast multispectral optical imaging of cortical oxygenation, blood flow, and intracellular calcium dynamics.* Opt Express, 2009. 17(18): p. 15670-8.

- Yuan, B., **Burgess, S.A.**, Iranmahboob, A., Bouchard, M.B., Lehrer, N., Bordier, C., and Hillman, E.M.C., *A system for high-resolution depth-resolved optical imaging of fluorescence and absorption contrast.* Rev Sci Instrum, 2009. 80(4): p. 043706.

- Radosevich, A.J., Bouchard, M.B., **Burgess, S.A.**, Chen, B.R., and Hillman, E.M.C., *Hyperspectral in vivo two-photon microscopy of intrinsic contrast.* Opt Lett, 2008. 33(18): p. 2164-6.

- **Burgess, S.A.**, Bouchard, M.B., Yuan, B., and Hillman, E.M.C., *Simultaneous multiwavelength laminar optical tomography.* Opt Lett, 2008. 33(22): p. 2710-2.

Oral Presentations

- **Burgess, S.A.**, Ratner, D., Chen, B.R., and Hillman, E.M.C. *Fiber-Optic and Articulating Arm Implementations of Laminar Optical Tomography for Clinical Applications*. in *Biomedical Optics. 2010:* Optical Society of America.

- **Burgess, S.A.**, Yuan, B., Bouchard, M.B., Ratner, D., and Hillman, E.M.C. *Simultaneous Multi-Wavelength Laminar Optical Tomography Imaging of Dermal Lesions*. in *Biomedical Optics*. 2008: Optical Society of America.

Conference Abstracts

- Plaisier F, Karagiannis A, **Burgess SA**, Chausson P, Hamel E, Hillman EMC, Cauli B, Identification of putative vasoconstricting neurons in the cerebral cortex. Federation of European Neuroscience Societies (FENS), July 2010, Amsterdam.

- Bouchard MB, Grosberg LE, **Burgess SA**, Hillman EMC, Laser-Scanning Intersecting Plane Tomography (L-SIPT) for high speed 3D optical imaging and microscopy. In: OSA Biomedical Topical Meetings, OSA Technical Digest, Optical Society of America, April 11-14 2010; Miami FL.

- **Burgess SA**, Ratner D, Chen BR, Hillman EMC, Fiber-Optic and Articulating Arm Implementations of Laminar Optical Tomography for Clinical Applications. In: OSA Biomedical Topical Meetings, OSA Technical Digest, Optical Society of America, April 11-14 2010; Miami FL.

- Sun R, Bouchard MB, **Burgess SA**, Radosevich AJ, Hillman EMC A Low-cost, Portable System for High-Speed Multispectral Optical Imaging. In: OSA Biomedical Topical Meetings, OSA Technical Digest, Optical Society of America, April 11-14 2010; Miami FL.

- Bouchard MB, Chen BR, **Burgess SA**, Hillman EMC, Ultra-fast multiwavelength CCD-based optical imaging. Engineering Conferences International meeting: Advances in Optics for Biotechnology, Medicine and Surgery XI. June 2009, Burlington VT.

- Chen BR, McCaslin AFH, Bouchard MB, Radosevich AJ, **Burgess SA**, Cauli B, Hillman EMC, High speed two-photon microscopy of reactive cortical cells in vivo. Engineering Conferences International meeting: Advances in Optics for Biotechnology, Medicine and Surgery XI. June 2009, Burlington VT.

- Bordier, C, Iranmahboob A, **Burgess SA**, Hillman EMC, Monte Carlo Modeling for 3D Optical Imaging of Mesoscopic Volumes. Engineering Conferences International meeting: Advances in Optics for Biotechnology, Medicine and Surgery XI. June 2009, Burlington VT.

- **Burgess SA**, Bouchard MB, Bordier C, Chen BR, Hillman EMC, Fluorescence Laminar Optical Tomography for Imaging Skin. Engineering Conferences International meeting: Advances in Optics for Biotechnology, Medicine and Surgery XI. June 2009, Burlington VT.

- Hillman EMC, Chen B, **Burgess SA**, Radosevich AJ, Bouchard MB, Iranmahboob AK, Das A, Cauli B. Multidimensional functional optical imaging of the brain. In: Proceedings of OSA Frontiers in Optics (FiO) October 19, 2008, Rochester, NY.

- Bouchard MB, **Burgess SA**, Moussazadeh P, Radosevich AJ, Wuskell JP, Loew LM, Pertsov A, Hillman EMC. Electrical and metabolic imaging of cardiac ischemia In: OSA Biomedical Topical Meetings, OSA Technical Digest, Optical Society of America, Washington DC, 2008. March 16-19; St Petersberg FL.

- Radosevich AJ, Bouchard MB, **Burgess SA**, Stolper R, Chen B, Hillman EMC. Hyperspectral in-vivo two-photon microscopy. In: OSA Biomedical Topical Meetings, OSA Technical Digest, Optical Society of America, Washington DC, 2008. March 16-19; St Petersberg FL.

- **Burgess SA**, Yuan B, Bouchard MB, Ratner D, Hillman EMC. Simultaneous Multi-Wavelength Laminar Optical Tomography Imaging of dermal lesions. In: OSA Biomedical Topical Meetings, OSA Technical Digest, Optical Society of America, Washington DC, 2008. March 16-19; St Petersberg FL.

- Hillman EMC, Chen B, **Burgess SA**, Radosevich AJ, Bouchard MB, Iranmahboob AK, Das A, Cauli B. Multidimensional functional optical imaging of the brain. [Invited] In: OSA Biomedical Topical Meetings, OSA Technical Digest, Optical Society of America, Washington DC, 2008. March 16-19; St Petersberg FL.

- Hillman EMC, Bouchard MB, **Burgess SA**, Gossage K, Mansfield JR, Levenson RM, Dynamic Molecular Imaging: Anatomical Co-registration and Dynamic Contrast Enhancement. In: OSA Biomedical Topical Meetings, OSA Technical Digest, Optical Society of America, Washington DC, 2008. March 16-19; St Petersberg FL.

- Hillman EMC, Yuan B, **Burgess SA**, Iranmahboob AK, Bouchard MB. Depth-resolved optical imaging of calcium sensitive dyes in somatosensory cortex in-vivo, Society for Neuroscience 2007. November 3-7; San Diego CA.

- **Burgess SA**, Yuan B, Radosevich AJ, Bouchard MB, Hillman EMC. “High-resolution 3D optical imaging of tissue”, IEEE Proceedings LEOS (2007).

- **Burgess SA**, Yuan B, Pease E, Iranmahboob A, Hillman EMC. “Laminar Optical Tomography for Dermal and Cardiac Imaging”. Engineering Conferences International: Advances in Optics for Biotechnology, Medicine and Surgery, Naples, June 2007.

Chapter 1

Introduction and Background

The ability of light to probe biological materials stems from the numerous interactions light undergoes with its environment. In biological tissues, these interactions include, among others, absorption, scattering, and fluorescence. While scattering can be used as a source of optical contrast, it also presents a significant challenge to optical imaging as it limits the penetration depth of optical techniques by attenuating light and introducing uncertainty in the path that the light travels. In the past few decades, advanced optical imaging techniques have been developed to exploit the value of optical contrast while maximizing resolution and penetration depth. Techniques such as confocal microscopy offer increased resolution and contrast (compared to conventional fluorescence microscopy) by rejecting out of focus light while techniques such as diffuse optical tomography push the penetration depth of optical imaging through innovative instrumentation and advanced tomography algorithms.

Laminar optical tomography (LOT) was developed to record depth sensitive measurements of light in order probe optical properties of tissues beyond the depths of conventional microscopy and with resolution exceeding that of diffuse optical techniques. The technique relies upon scattering to collect backscattered light and is sensitive to absorption and fluorescence contrast.

This chapter starts with an introduction to the light tissue interactions that are relevant to many optical imaging techniques including LOT. A range of related optical imaging techniques that

demonstrate the innovative ways in which light-tissue interactions are exploited or overcome to yield optical contrast will be explored. Knowledge of these interactions and techniques is important for understanding the final section of this chapter which describes the basic principles of LOT imaging.

1.1 Photon Interactions

As light travels through biological tissues, several light-tissue interactions may occur, including absorption, scattering, and fluorescence (Figure 1-1a). The degree to which these interactions occur is governed by the optical properties of the tissue with local differences in optical properties serving as the source of contrast in optical imaging.

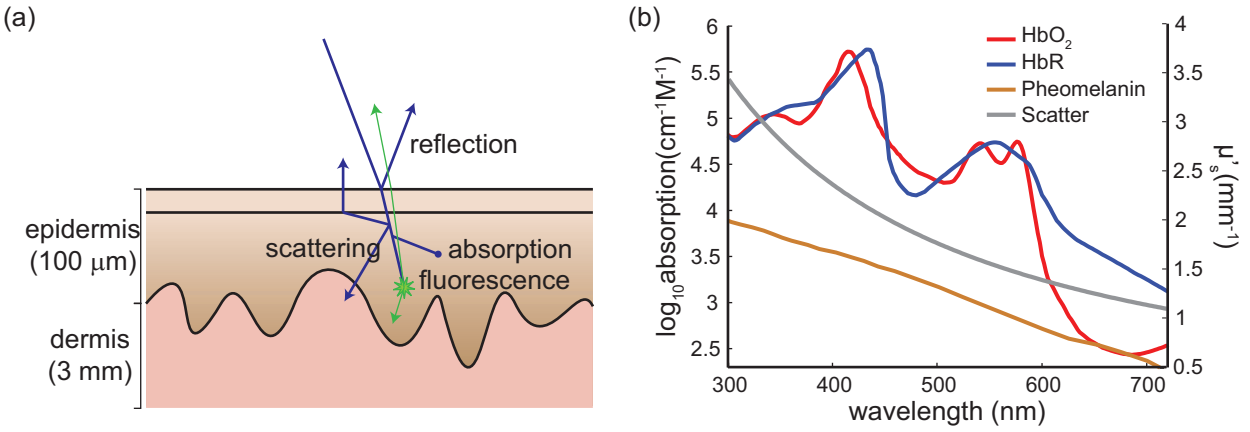

Figure 1-1 (a) Interaction of light with tissue yields several sources of contrast including, scattering, absorption and fluorescence. (b) Absorption spectra of common biological chromophores and scattering spectrum of tissue. Data from [10, 11].

1.1.1 Absorption

During absorption, energy from incident light radiation is transferred to the atoms and molecules of the surrounding system. The overall effect of absorption is a reduction in the transmitted light intensity. The tissue absorption coefficient (μ_a) is a parameter that describes the effectiveness of optical absorption and is the inverse of the average distance a photon travels before being absorbed. The relationship describing light intensity and tissue absorption is given by the Beer-Lambert Law:

$$I = I_0 e^{-\mu_a l} \qquad \textbf{Eq 1-1}$$

where I_0 is the intensity of incident light and l is the path length of light travel in the tissue. The absorption coefficient of a medium is determined by the absorbing substances (chromophores) within the tissue. Each chromophore has a wavelength-dependent extinction coefficient (ε_n) that characterizes their absorption per unit concentration. According to Beer's law, the absorption coefficient of a tissue is a function of the chromophores in the tissue, the individual chromophore concentrations (c), and the wavelength of light (λ):

$$\mu_a'(\lambda) = \sum_n \varepsilon_n(\lambda) c_n \qquad \textbf{Eq 1-2}$$

The higher the concentration of a chromophore, the stronger its relative contribution will be to the overall absorption properties of the tissue. Changes in a chromophore's concentration will therefore result in a change in the light intensity. For a homogeneous medium this change is given by:

$$\log\left(\frac{\Delta I}{I_0}\right) = -\varepsilon(\lambda)\Delta c l\,, \qquad \textbf{Eq 1-3}$$

allowing the concentration change to be calculated given that the extinction coefficient and path length through the medium are known. For a medium having more than one chromophore, measurements at additional wavelengths are necessary and can be used to determine concentration changes by solving for a system of equations.

There are many substances in the body that can absorb light, most notably oxygenated and deoxygenated hemoglobin (HbO_2 and HbR) in blood and melanin in skin. Hemoglobin absorption contrast has been widely used for *in vivo* optical imaging due to its physiological importance and its ability to provide functional information [12]. The absorption spectra of HbO_2, HbR, and melanin are shown in Figure 1-1b. The spectra for HbO_2 and HbR differ significantly at several visible wavelengths, notably red and blue, and intersect at others such as green. Melanin absorption is highest near the UV region as melanin acts to protect skin from damaging UV radiation from the sun [13]. The concentration of individual chromophores within a sample volume can be estimated by taking measurements at several wavelengths and solving the resulting system of simultaneous equations. When using this technique, wavelength selection becomes a significant concern because the calculations rely on the absorption coefficient of each chromophore being different at each wavelength. The effects of scattering, another light-tissue interaction, must also be considered as the exact distance travelled in the tissue becomes unknown.

1.1.2 Scatter & anisotropy

Scattering of light is a process in which light is forced to deviate from a straight trajectory and is responsible for the uncertainty in the path that light travels within the tissue. Scattering in tissue is caused by a relative refractive index mismatch between adjacent structures, e.g. between the extracellular fluid and the cell membrane [14, 15]. Since the behavior of scattered light is a function of the size, density, and shape of the particles causing scattering, scattering is another source of optical contrast [16-18]. As with absorption, scattering in tissue is wavelength dependent. The scattering spectrum of tissue is provided in Figure 1-1b. The typical distance that a photon travels before experiencing a scattering in tissue is 0.05 to 0.2 mm [19]. The inverse of the average distance travelled between scattering events is known as the scattering coefficient (μ_s) and the average cosine of the scattering angle is referred to as the anisotropy factor (g). If the scattering is completely isotropic then g will be equal to 0. As the scattering becomes more forward facing, the average cosine tends towards a value of 1. Biological tissue is a highly forward scattering medium resulting in an anisotropy factor close to 1. Together the scattering coefficient and anisotropy factor effects are described by the reduced scattering coefficient (μ'_s):

$$\mu_s' = \mu_s(1-g) \qquad \textbf{Eq 1-4}$$

1.1.3 Fluorescence

Fluorescence occurs when a molecule absorbs light, causing transition to a high-energy state, and then losing the excess energy by emitting lower energy light as it returns to its initial state. This process can serve as a valuable source of contrast for optical imaging. Numerous molecules *in*

vivo exhibit fluorescence, including structural proteins such as collagen and elastin, and enzymes such as NADH and FAD [20]. In addition to *in vivo* fluorophores, fluorescent dyes and transgenic animal models that express fluorescent proteins in specific cells have been developed and are widely used. Two spectra commonly associated with fluorescence are a molecule's excitation and emission spectra. A fluorescence excitation spectrum is a plot of the fluorescence emission intensity as a function of excitation wavelength and a fluorescence emission spectrum is a plot of the fluorescence emission intensity measured over a range of emission wavelength at a fixed excitation wavelength. The excitation spectrum indicates the likelihood of a molecule fluorescing under a given excitation wavelength, while the emission spectrum provides the likely wavelength of the emitted light. These spectra are important in the design of an optical system that is sensitive to fluorescence contrast and should be considered when selecting the wavelength of the excitation source wavelength and optical filters in the detection path. Example excitation and emission spectra for NADH, an important measure of metabolism, are shown in Figure 1-2. These spectra are characteristic of the fluorescent molecule as well as the tissue micro-environment, such as pO_2, pH and intracellular calcium concentrations [21].

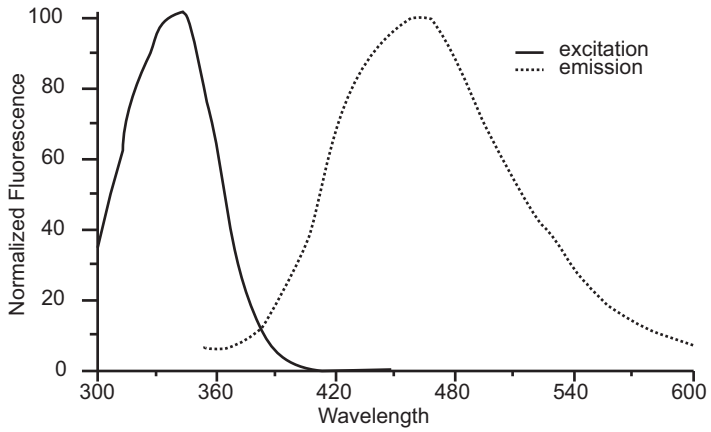

Figure 1-2 NADH excitation and emission spectra. Excitation spectra obtained by exciting at wavelengths from 300 nm to 460 nm. Emission spectra obtained by exciting at 340 nm and scanning the emission wavelength from 350 nm to 600 nm. Data from [22].

1.2 Optical Imaging Techniques

The major challenge associated with *in vivo* optical imaging is to exploit the vast sources contrast that lie within the body, and to image them with sufficient resolution and to sufficient depths. Optical techniques that rely on measuring single-scattered photons are limited to imaging to depths of a few hundred micrometers due to the effects of scattering. Techniques that rely on diffuse light can image to deeper depths but have lower resolution due to the uncertainty in the path that the light has travelled. The mesoscopic imaging regime lies between these two regions, where light has scattered multiple times but is not yet diffuse. In general, mesoscopic imaging is limited to applications where tissues of interest are superficial, such as the skin, eye and oral mucosa. However, mesoscopic optical imaging of internal organs can be achieved via endoscopic, intraluminal or intrasurgical imaging configurations. The desire to image in and around this region has driven the development of LOT and many other optical imaging techniques. An overview of a range of optical techniques is shown in Figure 1-3. A brief description of each follows.

1.2.1 Confocal laser scanning microscopy

Confocal laser scanning microscopy (CLSM) is a technique that can be used to measure tissues with fluorescence or reflectance contrast. CLSM uses a focused, scanning laser beam to form an image. At each position, fluorescent or reflected light from the focal region within the tissue is collected. Light that has undergone several scattering events and is out of focus or off-axis, is rejected by placing a pinhole in a conjugate image plane before the detector. The same optics responsible for scanning the sample simultaneously acts to de-scan the sample allowing a single

stationary pinhole and detector to be used. Optical sectioning is achieved by adjusting the depth of the focus within the tissue. However, as the focal depth increases, it becomes more difficult to maintain a focused beam due to the effects of scattering. The penetration depth is dependent upon the intensity and wavelength of illumination, and the optical properties of the tissue sample. *In vivo* imaging of reflectance contrast in skin to depths of 200-300 μm has been reported [23].

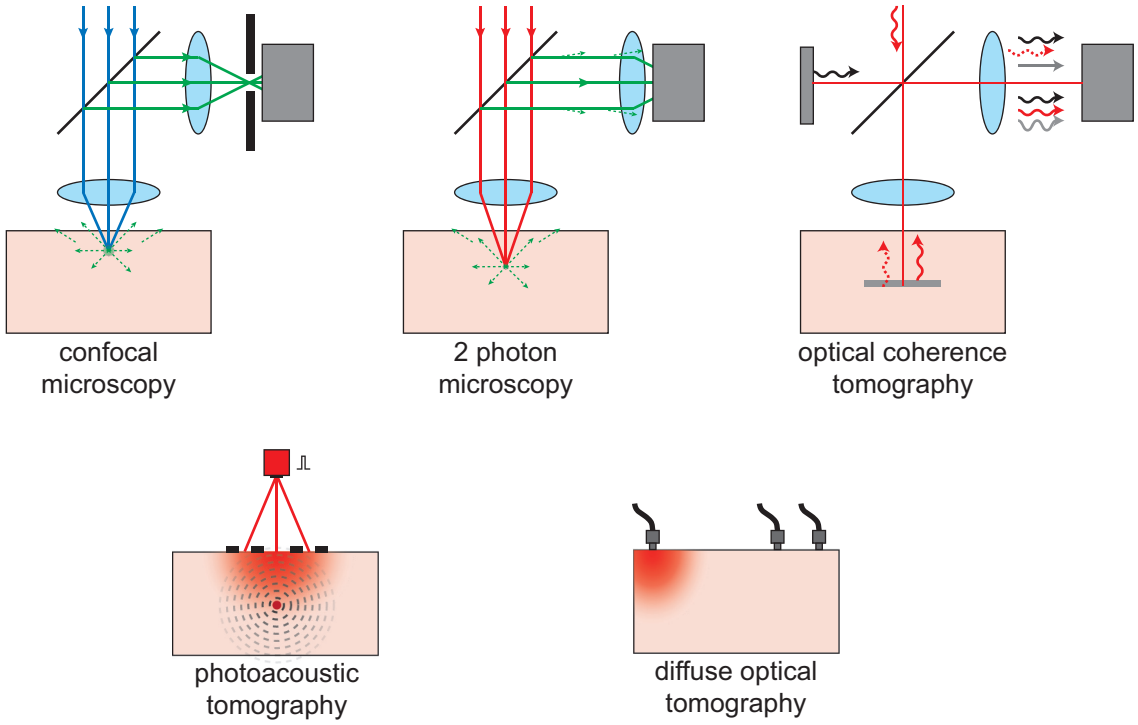

Figure 1-3. Basic configuration for several optical imaging techniques. Confocal microscopy rejects off-axis backscattered or fluorescence light with a pinhole in front of a descanned detector. Two-photon microscopy uses nonlinear excitation to ensure only fluorophores at the focal point of the objective are excited. Optical coherence tomography uses phase differences between a reference beam and reflected light to select imaging depth. Photoacoustic tomography relies on light absorption and subsequent thermal expansion to generate thermo-elastic waves that are detected by ultrasound transducers on the tissue surface. Diffuse optical tomography injects light and utilizes a number of detectors to collect boundary data that are then used for image reconstruction.

1.2.2 Two-photon microscopy

Two-photon microscopy is sensitive to fluorescence contrast and uses a setup similar to CLSM, however longer wavelength, pulsed laser light is used to excite the tissue and a pinhole is not needed in the detection path. Two-photon excitation requires two photons to be absorbed at virtually the same time which is rare at light intensities used for epifluorescence microscopy. To increase the likelihood of a two-photon even, pulsed lasers generating short duration (~100 femtosecond) pulses at a rapid repetition rate (~80 MHz) are used to increase the instantaneous light intensity. The combined energy of the two near infrared photons is approximately equal to that of single photon visible light excitation. As a result, a fluorophore that typically excites near 400 nm will require 800 nm pulsed light for two photon excitation. Since the excitation and subsequent emission only occurs at the focus (where the flux is high enough for two near-simultaneous photons to arrive), all of the fluorescent light collected is known to have originated from the focus alleviating the need for descanning, or a pinhole to reject out of focus light. In fact, two-photon systems ideally will collect all the fluorescence light emitting from the sample. The use of longer wavelength (which has less scattering and absorption in tissue) and lack of out-of-focus absorption allows more of the excitation light to reach the focus. As a result, two-photon microscopy can image to deeper depths than CLSM with imaging up to 500 μm reported [24, 25]. *In vivo* two-photon microscopy has been limited to studying animal models where it has primarily been used to image the brain [26, 27].

1.2.3 Optical coherence tomography

Optical coherence tomography (OCT) is a mesoscopic imaging technique that relies on interference between the collected light and a reference beam to reject multiply scattered light.

Light is split into and recombined from a reference and sample arm respectively. Upon recombining, light that travelled the same distance in the reference and sample arms will be in phase and constructively interfere, while light that has multiply scattered or back reflected at different depths within the tissue will destructively interfere. Depth sections are obtained by moving the reference arm mirror, thereby changing the reference arm path length. OCT contrast is generated mainly from back reflected light. Absorption contrast is limited owing to the deliberately short path length and fluorescence contrast is not achievable. OCT can image to depths of 1-2 mm in tissue with 1-10 μm resolution [28] and has been widely used for clinical imaging of the eye [29, 30].

1.2.4 Photoacoustic tomography

Photoacoustic tomography (PAT) involves irradiating tissue with a short pulsed laser to produce thermal and acoustic impulse responses. Upon light absorption, the energy of the light is converted into heat causing subsequent thermoelastic tissue expansion and the formation of a pressure wave. Ultrasound transducers positioned on the surface of the tissue detect the photoacoustic waves. Ultrasound image reconstruction techniques can thus be applied to form an image. PAT is sensitive to absorption contrast since it relies on light absorption to generate a photoacoustic wave. The effects of light scattering on PAT are reduced as the incident light does not need to be focused and the photoacoustic waves are not affected by optical scattering. The penetration depth of PAT exceeds 1 cm with resolution of 20-50 μm [31, 32].

1.2.5 Diffuse optical tomography

Diffuse optical tomography (DOT) is an optical imaging technique that involves reconstruction of spatially varying absorption and scattering properties as well as fluorophore lifetime and quantum yield in tissues from boundary measurements [33-36]. Unlike microscopy and OCT that attempt to isolate minimally-scattered photons, DOT makes use of multiply scattered light allowing for deeper imaging depths with a trade-off of relatively poor lateral resolution. A typical DOT setup uses several optical fibers positioned on the surface of the tissue to be imaged. Light is injected into the tissue through one optical fiber at a time while a number of optical fibers or fiber bundles route light emerging from the tissue to detectors. Although the spatial resolution of DOT is limited, typically on the order of centimeters, the penetration depth of DOT goes beyond a few centimeters making it appealing for optical imaging of large tissue samples [33, 35, 37]. The use of near-infrared light (650-100 nm) aids in probing deeper into tissue due to its relatively low absorption and scattering in tissue.

1.3 Laminar Optical Tomography

LOT can be considered a hybrid technique that combines the data acquisition instrumentation of confocal microscopy with the measurement geometry of DOT. Like confocal microscopy, LOT uses a non-contact laser scanning setup that relies on a set of mirrors to scan the incident light over the sample while at the same time using the mirrors to descan the returning light. Like DOT, LOT measures light that has emitted from the tissue at some distance offset from the source position. High density measurements, which have been shown to improve the resolution

of DOT [38-40], are rapidly obtained with LOT without the need for advanced instrumentation. Despite sharing similar instrumentation as confocal microscopy and similar measurement geometry as that of DOT, the light measured by LOT is quite different. Confocal microscopy measures ballistic light, limiting its penetration depth but allowing for high resolution imaging. DOT detects diffuse light, allowing it to probe deeper depths but with poorer resolution. The light measured by LOT is from the region in tissue in which light has multiply scattered but is not yet diffuse. By measuring this light, LOT offers a compromise between the two techniques: providing deeper penetration than confocal microscopy (with lower resolution) and higher resolution than that of DOT (with less penetration). The implementation of LOT is highly adaptable allowing parameters such as field of view, acquisition speed, and measurement density and geometry to be easily adjustable. The remaining sections of this chapter are devoted to describing the measurement geometry of LOT, the basic components of an LOT system, and analysis of LOT data.

1.3.1 Measurement geometry

LOT measurements are acquired by scanning a point source of light over the surface of a tissue, and detecting light that is emitted from the tissue close to each source position (from 0 to 3 mm away). The position to which light is delivered is referred to as the source and the position from which light is collected from is called the detector position. Light entering at a discrete source position on the surface of a scattering tissue will scatter within the tissue, encountering absorbers and/or fluorophores along its path. Some of this light will emerge from the same surface of the tissue at various distances away from the source position. LOT's ability to perform depth-resolved imaging relies upon the statistical probability that light emerging at greater distances

from the source position has, on average, scattered more deeply into the tissue. The wider the source-detector separation distance, the deeper on average the detected light has travelled within the tissue (see Figure 1-4). While measurements obtained from wider detector separations are more sensitive to deeper depths, they do not represent true depth-sectioning as with CLSM. Instead, these measurements represent a weighted sum of signal from shallower and deeper layers. Unlike other microscopy techniques that reject scattered light, LOT relies on scattering to collect off-axis backscattered light.

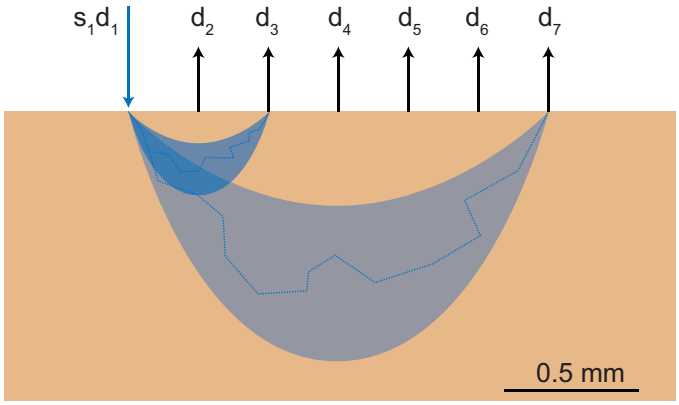

Figure 1-4 LOT measurement geometry. Upon entering a scattering tissue, light undergoes multiple scattered. Light emitting from further distances from the source position will, on average, have travelled more deeply into the sample.

Since LOT does not reject scattered light, there is no explicit 'scattering limit' as encountered in CLSM. Imaging to tissue depths beyond those attainable with conventional microscopy can feasibly be achieved if wider source-detector separations are used, and lower image resolution is acceptable. In the limit of wider source-detector separations, the measurements that LOT acquires are equivalent to reflectance-geometry diffuse optical tomography measurements [41, 42]. The two techniques differ in that with the narrower source-detector separations used in LOT, the detected light has been scattered and attenuated less, and can therefore yield higher resolution images with better signal to noise. In addition, LOT instrumentation differs from DOT, which

typically uses optical fibers positioned in a grid pattern on the tissue's surface [42-44]. LOT uses non-contact laser-scanning, allowing rapid frame-rate, multi-spectral imaging with an adaptable field of view and measurement density. The basic design of LOT instrumentation is described next.

1.3.2 Instrumentation

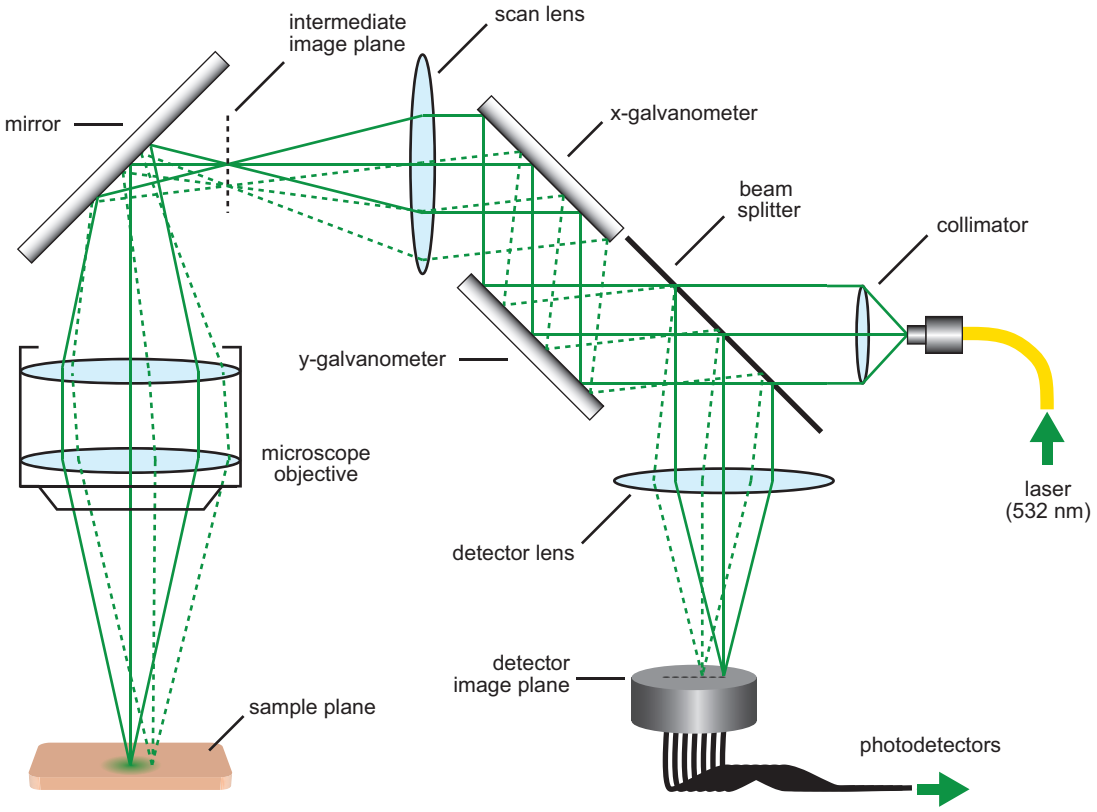

Figure 1-5 Basic design of an LOT system as described in [1]. Galvanometer mirrors raster scan a focused spot over the sample plane. On axis (solid line) and off-axis (dashed line) light are descanned by the galvanometer mirrors and measured using multiple detectors.

Figure 1-5 shows the optical pathway and principal elements of an LOT system. The incident light is shown as solid lines originating from an optical fiber. The light is collimated and passed through a beam splitter before being reflected by a set of galvanometer mirrors. These mirrors are computer controlled to raster scan the beam. The beam then passes through a scan lens,

which converts the angular deviation of the collimated light into a lateral translation of the scanning spot. The raster scanning spot at the intermediate image plane of the scan lens can then be imaged onto the sample plane using an objective lens arrangement.

On-axis backscattered light travels back through the optical system with the same path as the incident light. However, upon reaching the beam splitter, the returning light is reflected towards the light detection components of the system. A lens focuses the light onto linear fiber bundle positioned conjugate to the sample plane. The distal end of each fiber in the array is connected to a photodetector to measure the intensity of the returning light.

Off-axis backscattered light (Figure 1-5, dashed lines) follows the path of light emerging from the sample at a position laterally displaced from the focus of the incident beam. This light also travels back through the system and is de-scanned by the galvanometer mirrors. As the light reflects off the beam splitter, it focuses to a point adjacent to the focal point of light from the center of the scanning beam. As with the confocal light, for all scanning source positions, the light emerging from the tissue at some distance away from the spot's focus will be imaged onto a fiber that is similarly displaced from the center of the scanning spot in the detector plane. Each fiber and associated detector in the linear fiber bundle separates light emerging at specific distance from the focus. It is this scattered light that provides information about the deeper layers of the tissue.

1.3.3 LOT data analysis

A critical aspect of LOT is mathematical modeling of light propagation. The fact that light emerges from the same surface of the tissue as it enters is because it has scattered in a random

path. The depth sensitivity of LOT measurements can be predicted using mathematical models that simulate the way in which light is likely to travel in the tissue, assuming that the scattering and absorbing properties of the medium, as well as the illumination and detection geometry are known [41, 45, 46]. More complex geometries and heterogeneous tissues can also be investigated, although the accuracy of the model will depend on the amount of a-priori information available. Modeling can be used to analyze LOT data in a variety of ways, from prediction of bulk optical properties to 3D image reconstruction as described below.

1.3.3.1 3D image reconstruction

Conventional tomographic image reconstruction creates a cross-sectional image from a series of projection measurements through an object. In x-ray computed tomography (CT), several hundred projections are acquired at all angles through the object [47]. Because of light scattering, it is possible to acquire a set of projections through an object in reflectance geometry when using optical techniques, as illustrated in Figure 1-4. A series of overlapping projections that sample across the surface, with different source-detector separations probing different depths, can therefore be used to reconstruct a 3D image of objects within the scattering tissue in an analogous way to x-ray CT. However, compared to x-ray CT methods, optical tomographic image reconstructions are less able to completely describe the structure of an object owing to the inherent uncertainty in the paths that photons have travelled. This uncertainty results in poorer quantitation and resolution than x-ray imaging, in addition to spatially-dependent resolution.

In both x-ray CT and LOT, knowledge of the sensitivity distribution of each of the projection measurements is required. In x-ray CT, this is relatively straightforward since detected x-rays can be restricted to those that have passed in a straight trajectory through the body at a known

series of angles. However, with LOT, the sensitivity of each measurement path is a function of the optical scattering and absorption properties of the tissue being probed. As a result, image reconstruction relies on the ability to simulate the behavior of light scattering in tissue to determine the spatial sensitivity of each measurement. For diffuse optical imaging, the diffusion approximation can be used to simplify modeling since analytical formulae exist for simple geometries [48]. However, for LOT imaging, the diffusion approximation cannot be employed since light cannot be assumed to be diffuse until it has propagated at least 1 mm in most tissues [49]. To date, Monte Carlo modeling methods have been used to simulate sensitivity functions (see Figure 1-6) $J_{s,d}(r)$ that correspond to maps of the likely change in measurement $\Delta M_{s,d}$ between a source and detector position s,d that will result from a unit change in absorption $\Delta\mu_a(r)$ at position r:

$$J_{s,d}(r) = \frac{\partial M_{s,d}}{\partial \mu_a(r)} \qquad \textbf{Eq 1-5}$$

which can be simplified to:

$$\Delta M_{s,d} = J_{s,d}(r)\Delta\mu_a(r) \qquad \textbf{Eq 1-6}$$

in cases where the change in absorption $\Delta\mu_a(r)$ is small. Assuming that $J_{s,d}(r)$ accurately represents the physical measurements from LOT, Eq 1-6 can be inverted using a range of regularization approaches to produce images of $\Delta\mu_a(r)$. Further discussion of Monte Carlo modeling for LOT is provided in Section 1.3.3.3.

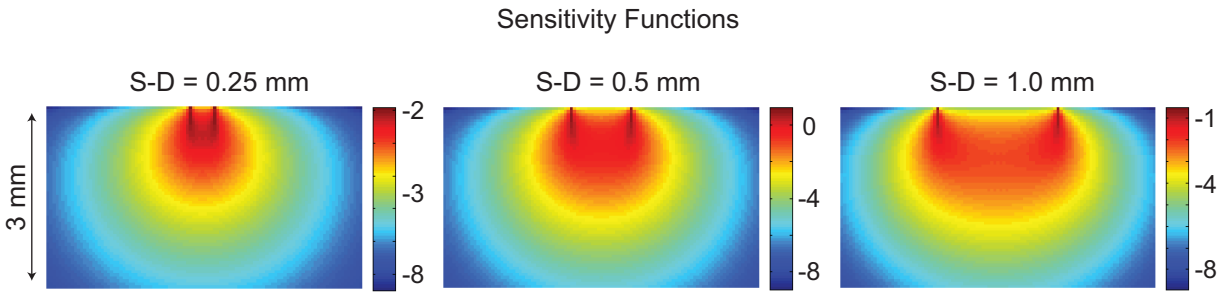

Figure 1-6 LOT absorption contrast sensitivity functions generated using Monte Carlo modeling for 3 source-detector separations.

In its simplest form, LOT image reconstruction can assume that the tissue being imaged is homogenous, its optical properties well known and that the image to be reconstructed is of a small change in absorption $\Delta\mu_a(r)$ such that measurements $\Delta M_{s,d}$ correspond to the difference between measurements before and after that change. In this case, a fairly simple Monte Carlo based forward model can be used to generate $J_{s,d}(r)$ and Tikhonov regularization or other iterative solvers can be used to invert Eq 1-6. Images reconstructed in this way were shown in [50-54].

More advanced image reconstruction approaches could include using non-linear image reconstruction schemes that attempt to accommodate background optical property heterogeneity by re-modeling light propagation based on changing estimates of the baseline [41, 55-57]. Iterative non-linear reconstructions have been developed for DOT, however implementation is greatly facilitated by the availability of analytic solutions to the diffusion approximation, which enable rapid finite element and finite difference-based forward modeling [48]. As mentioned above, the diffusion approximation is not valid for LOT data, and Monte Carlo modeling is typically too slow for implementation within iterative non-linear reconstructions. Furthermore, to date LOT has only been implemented for continuous-wave measurements, which in general cannot accurately distinguish between the effects of absorption and scattering [58]. This makes it

unfeasible, at present, to develop an ‘absolute’ image reconstruction scheme that can predict and account for both scattering and absorbing baseline heterogeneities in tissue using LOT.

1.3.3.2 LOT ‘raw’ data analysis

An alternative approach to a full 3D image reconstruction is to utilize models of light propagation to perform simplified analysis of ‘raw’ LOT data. This approach is valuable in situations where a full 3D image reconstruction is not required, but simple parameters relating to a tissue’s optical properties or structure are sought. For example, given an LOT data set consisting of 2D ‘raw’ data images from multiple source-detector separation distances, the measurements at every point in these images can be modeled. If the same x-y pixel from each of these images is selected, it is possible to plot the intensity of remitted light as a function of source-detector separation, and the shape of this curve is characteristic of both the absorbing properties of the object, its depth and its thickness.

Rather than using all of these measurements to attempt to reconstruct a 3D image of this phantom, a series of Monte Carlo based forward models that predict the relative intensities of remitted light that would be expected at each source-detector separation for a wide range of different object absorption coefficients and depths can be used for comparison with the LOT data. Using least-squares fitting, it was possible to match the ‘raw’ data plots extracted from the LOT ‘raw’ data images to the predicted values in the simulated look-up table [59].

1.3.3.3 Monte Carlo modeling for LOT

LOT imaging spans length-scales from less than 100 μm to several millimeters, and to date imaging has been predominantly performed using visible light wavelengths between 470–650

nm. The typical absorption coefficients of tissue within this wavelength range are between 0.1 and 0.5 mm^{-1}, and reduced scattering coefficients are between 0.5 and 2 mm^{-1} (corresponding to anisotropy factor between 0.75-0.9 and scattering coefficients between 5 and 20 mm^{-1}). Light propagation in scattering tissue can be modeled by the Radiative Transport Equation (RTE). However, solving this equation has proved challenging until very recently, making it difficult to use effectively for routine image reconstruction [60, 61]. A simplification of the RTE is the diffusion approximation, which neglects information about the directionality of scattering by scaling the scattering coefficient according to the anisotropy of scattering to create the reduced scattering coefficient, and assuming that all scattering events are isotropic. The diffusion approximation imposes limitations on the applicability of the model, including the requirement that μ'_s is much greater than μ_a and that the distances being considered are much greater than $1/\mu'_s$. Neither of these conditions is true for LOT and therefore the diffusion approximation to the RTE is not a suitable model for this application. Instead, LOT must utilize a model that can account for the directionality of scattering of light on small length scales, leaving the option to either use the complete RTE for modeling, or to use Monte Carlo modeling. While analytic solutions to the RTE are now becoming available, they have yet to be applied to LOT image reconstructions [62, 63]. To date, LOT image reconstructions have used Monte Carlo modeling as described next.

Monte Carlo modeling has been widely used for optical imaging and spectroscopy applications [46]. Monte Carlo modeling involves setting up a geometry with optical properties and a source configuration, and then launching individual photons into the medium and allowing them to propagate until they interact with a scatterer. The distance travelled between scattering events is randomly selected from a range of lengths based on the density of scatterers given by μ_s. Upon

scattering, the new direction of propagation is again randomly assigned, but weighted by the scattering anisotropy of the medium [64]. The photon is then allowed to continue until it meets another scatterer, and then another until it exits the tissue. The effects of absorption can be applied to the model if the path length travelled by the photon is logged at each point within the volume. While in actuality, a photon can either exist or not, rather than annihilating photons based on the likelihood of absorption having occurred, it is typical to reduce the 'weight' of the photon to a number less than 1 as absorbing events occur. This allows the net probability of the photon existing to be determined with fewer launched photons overall.

Modeling can be used to predict LOT measurements $M_{s,d}$ by determining which photons leave the object's surface within areas and angular distributions corresponding to each LOT detector. By creating a grid within the volume and recording the path length $x_{n,N}$ of detected photons N visiting particular regions r_n of this grid, it is possible to infer the changes in measurement that would result from differences in absorption $\mu_a(r_n)$ within those regions using Beer's law:

$$M_{s,d} = \sum_{N} e^{\sum_{n} \mu_a(r_n) x_{n,N}} \qquad \textbf{Eq 1-7}$$

This kind of modeling does not rely on any linearization assumptions, and can be used to generate 'lookup table' data as described above.

It is also possible to directly generate $J_{s,d}(r)$ using Monte Carlo modeling by effectively distributing the weight of every detected photon into the grid elements along its path (scaled by the path length of the photon's visit within each grid element). The resultant distribution is equal to $J_{s,d}(r)$ under the assumption that changes in absorption $\Delta\mu_a$ are small. However, this approach

can only be used for absorption imaging (not fluorescence) and can be slow and noisy for larger source-detector separations since all areas of a 3D grid must be frequently visited for smooth distributions.

The analysis presented above has been specific to modeling the effects of absorption changes. Fluorescence modeling requires different considerations because when a photon is absorbed by a fluorophore, it does not retain its directionality and is reemitted isotropically as a photon of lower energy. Therefore, the direction in which the photon is traveling in when it interacts with the fluorophore is irrelevant, and the direction at which the returning photon is launched will be random. However, it is still necessary to account for the directionality of the paths taken by incident and detected photons [65]. An additional aspect that must be accounted for is the need to consider the differing optical properties of the background medium at the incident (excitation) light wavelength, and the detected (emission) wavelength of light from the fluorophore. This means that two different models are required in addition to estimates of the absorption and scattering properties of the medium at both wavelengths. Overall, these considerations mean that sensitivity functions $J_{s,d}(r)$ for fluorescence LOT measurements will be different to those derived for absorption changes, and could even have differing depth sensitivities, particularly if fluorescence is present in the background [52, 66].

In summary, modeling is a critical aspect of LOT which can allow both reconstruction of 3D images, and quantification of optical properties and geometrical parameters of measured tissues. However, LOT modeling requires special considerations in order to account for the much smaller length-scales of LOT measurements.

Chapter 2

LOT Instrumentation Development

LOT was first demonstrated in 2004 by Hillman et al [1] where it was shown that the technique could allow high-resolution 3D imaging in a scattering medium over depths of 0-2.5 mm. The primary target for this initial imaging system was absorption contrast in rat cortex [67]. Subsequent studies utilized the same LOT system to image voltage sensitive dye fluorescence in perfused rat heart [68]. However, this first generation system was limited in its speed, signal to noise, and was unable to image multiple wavelengths and fluorescence in parallel.

One of the main goals of this thesis was to develop an advanced LOT system for *in vivo* imaging capable of high-speed imaging of both absorption and fluorescence contrast. Speed was an important factor in the development of the system since the goal of many *in vivo* studies is to capture the dynamics of a rapidly changing biological system. Speed is also vital for acquiring *in vivo* clinical measurements as motion artifacts can complicate data analysis and the amount of time in which to acquire measurements is limited. The ability to image multiple sources of contrast offers additional insight into the structure and/or interrelations of different constituents of a tissue. These considerations weighed heavily into the design of the LOT system presented in this thesis.

This chapter describes the development of a second generation LOT system capable of both absorption and fluorescence imaging with high temporal frequency. We begin by describing the

system design, including the optical layout, electronic components, and control software. Calibration of the source-detector separations as well as LOT data is then discussed. Lastly, phantom studies used to demonstrate multi-wavelength and fluorescence LOT are described.

2.1 Simultaneous Multi-wavelength Laminar Optical Tomography

The first generation LOT system used 7 single avalanche photodiode detectors (APD), coupled to optical fibers arranged in a linear array. Multi-wavelength measurements were acquired using electronic shutters in front of two lasers allowing interlaces images to be acquired sequentially. In our new system, we wanted to include 3 lasers, to capture both fluorescence and absorption information. However, using shutters to interlace scans would cause the maximum frame rate of the system, governed by scanning and data streaming speeds, to be reduced by a factor of 3. Images at different illumination wavelengths would also be acquired in sequence, meaning that any movement or physiological changes occurring in the interim would directly affect spectroscopic analysis of the acquired data.

The solution to this problem was the idea to use a 2D array photomultiplier tube (PMT) detector instead of the fiber-array coupled to APDs. The addition of a diffractive element before this array bends light of different wavelengths by differing amounts, thereby projecting them onto different rows of the PMT array. Using this configuration, simultaneous, multi-wavelength measurements can be acquired. Our implementation of this system is described below.

2.1.1 Optical system

2.1.1.1 Illuminating the sample

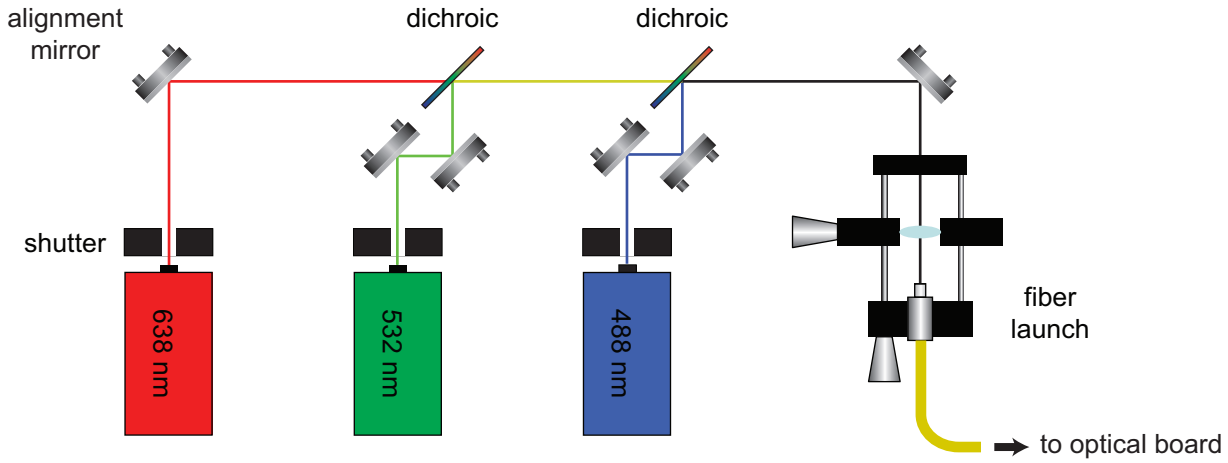

Figure 2-1 LOT laser board. Collinearly aligned lasers are coupled into a fiber launch and delivered to the optical board section of the system.

Three lasers, 488 nm, 532 nm, and 638 nm (85-BCD-030-115, 85-GCA-020, 56RCS004/HS, Melles Griot), are collinearly aligned into a polarization maintaining single mode fiber (PM460-HP, Thorlabs) as shown in Figure 2-1. The fiber light delivery system offers greater convenience over direct beam delivery by providing increased flexibility of component placement and by providing control of the polarization orientation through the use of a rotation mount fiber launch. The intensity of the lasers (>20mW) is such that light loss due to coupling efficiency is not limiting, as 1-5 mW was suitable for most imaging applications.

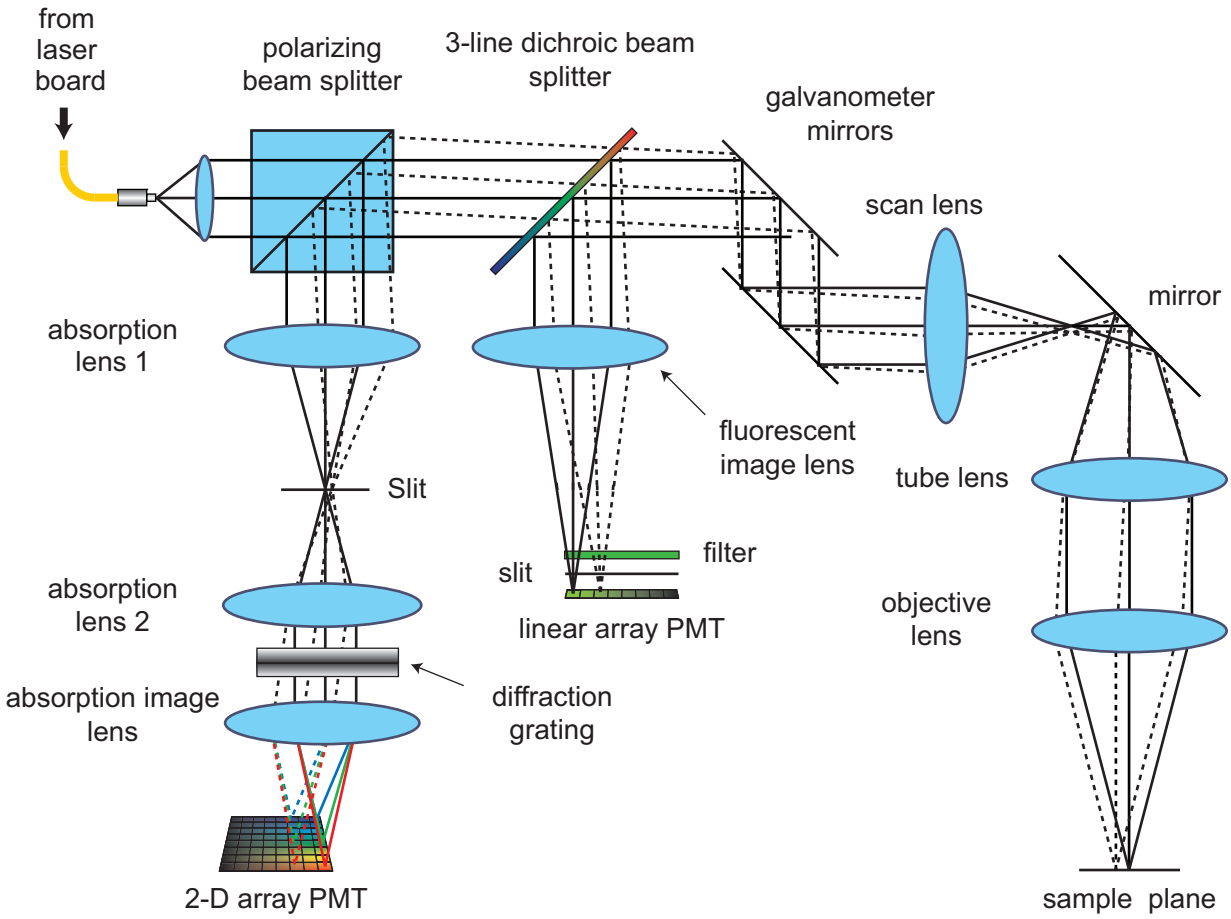

Figure 2-2 LOT optical board. Collinearly aligned laser light is delivered from the system's laser board. Galvanometer mirrors scan a focused beam over the sample plane while fluorescent and multi-wavelength absorption detection arms simultaneously detect the returning light.

Figure 2-2 shows a schematic diagram of the optical layout of the system. The fiber delivers the beam to a polarizing beam splitter (PBS-03 PBB 007, Melles Griot) that passes only horizontally polarized light. After passing through the polarizing beam splitter the light travels through a 3-line dichroic beam splitter (Di01-T488/532/638, Semrock). The transmission spectrum of the dichroic beam splitter is shown below in Figure 2-3. The dichroic beam splitter was selected such that each notch in the transmission spectrum corresponds with the wavelength of one of the lasers in the system. The polarizing beam splitter and dichroic beam splitter act to separate the incident light from the returning backscattered light for the absorption and fluorescent detection

arms respectively as described later in this section. After travelling through the dichroic beam splitter, the multi-wavelength light is reflected by a set of x and y galvanometer scanning mirrors (6215HB with 6 mm mirrors and two 671215H controllers, Cambridge Technologies). The galvanometer mirrors raster scan the beam through the scan and objective lenses and onto the sample.

2.1.1.2 Detecting fluorescent and backscattered reemitted light

Light emerging from the sample travels back through the lenses and is de-scanned by the galvanometer mirrors. Two different detection paths are used to measure the fluorescence and back-scattered multi-wavelength light. Fluorescent light is reflected by the dichroic beam splitter and focused through a slit onto a linear array photomultiplier tube (PMT) (R5900U-01-L16, Hamamatsu). In its current configuration, 7 of the 16 available channels are used providing 7 different source-detector separation distances. The value of the incremental offset distance is determined by the lenses used in the system and is discussed later in this chapter. A 1 mm tall slit positioned in front of the PMT limits the vertical extent of the detection area, so the elements of the detector array distinguish peripheral light that has scattered more deeply into the tissue from the superficially scattered light. A bandpass optical filter is typically positioned in the fluorescence detection arm to remove any residual excitation light. For the absorption detection path, the back-scattered multi-wavelength light passes through the dichroic beam splitter and is reflected by the polarizing beam splitter before being focused onto a slit. The polarizing beam splitter suppresses horizontally polarized specular reflections and reflects only vertically polarized light. Following transmission through the slit, a line of multi-wavelength light is collimated, and then focused through a transmission diffraction grating (GT50-06V, Thorlabs)

onto a 2D PMT array (H7546B, Hamamatsu). The diffraction grating separates the aligned multi-wavelength light into three horizontal lines, therefore the rows of the PMT measure different wavelengths, while the columns of the PMT measure light from different offset distances relative to the source position. By using 3 rows with 8 channels per row, a total of 24 channels are used on the 2D PMT array.

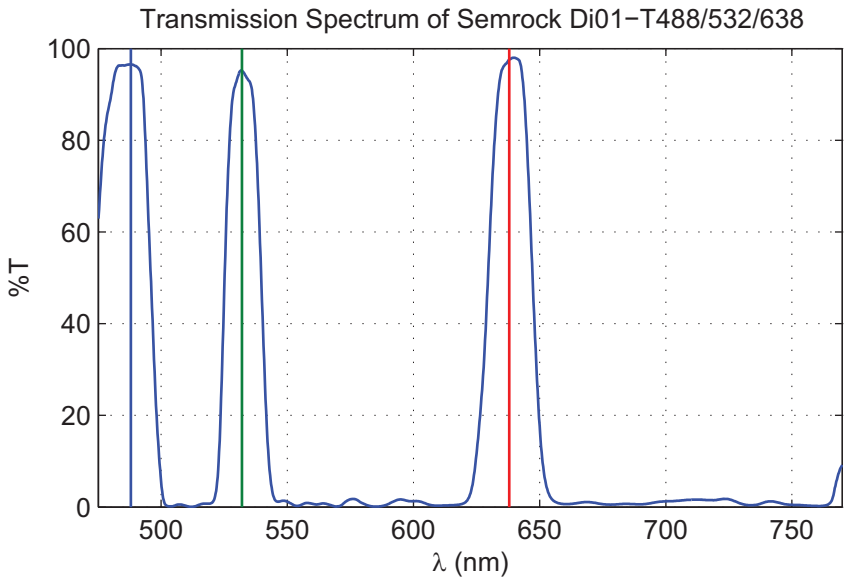

Figure 2-3 Transmission spectrum of 3-line dichroic beam splitter. Vertical lines indicate laser lines for the red, green, and blue lasers. Data from [69].

2.1.1.3 Optical components

Illumination source

The light source for multi-wavelength LOT consists of 3 lasers that provide greater than 100:1 ratio of polarized light with the output power of each exceeding 20 mW. The selection of wavelength is governed by the desired source of contrast. By configuring the system to use 488 nm, 532 nm, and 638 nm laser light, the system is sensitive to melanin, and oxy- and deoxygenated hemoglobin. These wavelengths can also be used to excite endogenous

fluorophores and fluorescent dyes for fluorescent LOT measurements. The dichroic beam splitter is paired with the emission lines of the lasers while the filter positioned in the fluorescence detection arm is optimized for the fluorophore being imaged.

Photo detectors

The three most common photo detectors used in optical imaging are charged-coupled devices (CCD), avalanche photodiodes (APD), and photomultiplier tubes (PMT). In a CCD, light is projected on a photoactive capacitor causing an electric charge proportional to the light intensity. The capacitor then dumps its charge into a charge amplifier which converts the charge into a voltage that is sampled and digitized. For avalanche photodiodes, light incident upon the semiconductor device excites charge carriers (photocurrent) that are accelerated by a strong internal electric field. The high energy carriers collide with the semiconductor lattice generating secondary carriers which are also accelerated creating further carriers. This avalanche effect amplifies the photocurrent which is then converted to a voltage, sampled and digitized. The LOT system uses PMTs to detect light. Photons incident upon the photocathode of a PMT (see Figure 2-4a) generate electrons via the photoelectric effect. The electrons are accelerated by an operating voltage applied to the PMT towards an electron multiplier consisting of multiple dynode stages. At each stage, the electrons are accelerated and focused onto the dynode generating secondary electrons that are subsequently accelerated and focused towards the next stage. The energy of the accelerated electrons and number of secondary electrons generated is proportional to the applied operating voltage. Therefore, the gain of the PMT can be controlled by changing the operating voltage. Figure 2-4b shows a plot of the linear relationship between gain and supply voltage for the 2D PMT array in LOT. The multiplied secondary electrons

emitted from the last dynode are collected by the anode of the PMT. If the incident light intensity is low enough that a single photoelectron is emitted from the photocathode, the output will be a pulse that can be used for photon counting. For LOT, the measured light is of sufficient intensity that the PMT pulse outputs overlap creating an analog signal. The resulting time varying current output from the PMT is proportional to the intensity of light incident upon the photocathode.

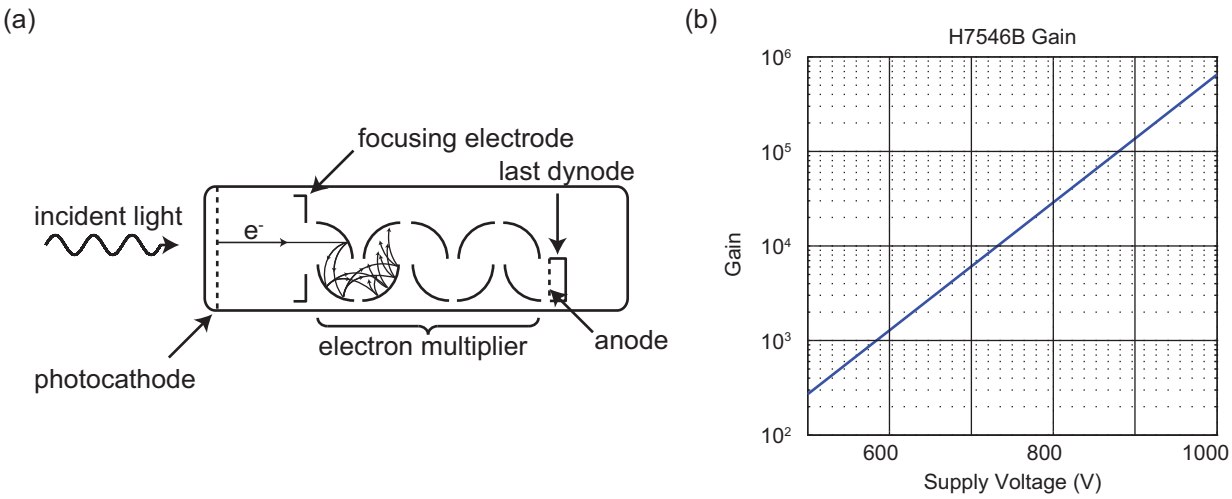

Figure 2-4. (a) Schematic diagram of a single channel PMT. (b) Plot of the typical gain vs. supply voltage relationship for the 2D PMT array in LOT.

The fluorescence detection arm of LOT has a 16 channel, linear array PMT. In its current configuration, 7 adjacent channels are used providing 7 different source-detector separation distance measurements. The absorption detection arm has a 64 channel (8x8 2D array) PMT. Multi-wavelength LOT measurements use 3 rows (one for each laser wavelength) and all 8 channels in each row for a total of 24 channels.

Polarized light

Light is an electromagnetic wave whose electric field can be described as the vector sum of two perpendicular electric field components, $E_{\parallel}$ and $E_{\perp}$. The magnitude and phase of $E_{\parallel}$ and $E_{\perp}$ can

take on any value, however for the case of linearly polarized light, the two wave components are aligned in phase. In order to describe the polarization, a reference frame is required. Let $E_{\parallel}$ be aligned parallel to the x-axis in the horizontal surface of an optical table and $E_{\perp}$ be aligned perpendicular to the surface. In this reference frame, horizontally polarized light would have a zero magnitude $E_{\perp}$ component. Alternatively, vertically polarized light would have a zero magnitude $E_{\parallel}$ component.

In LOT, the lasers output vertically polarized light that is aligned into a polarization maintaining optical fiber. The distal end of the fiber is mounted to a rotation mount just prior to the polarizing beam splitter. By rotating the fiber mount, the linearly polarized beam can be rotated from vertical polarization to horizontal polarization as well as all angles in between. The fiber mount is rotated to achieve horizontally polarized light that passes through the beam splitter on its way to the sample. Within the sample, the light undergoes scattering events such that the backscattered reemitted light is no longer linearly polarized. This returning light is reflected by the polarizing beam splitter towards the detection arm of the system. The use of polarization to separate incident light from backscattered reemitted light from the sample offers two advantages: the light efficiency is improved versus using a 50:50 beam splitter and specular reflections from optical components in the system are suppressed. When using a 50:50 beam splitter, half of the incident light is lost on its way to the sample and half of the backscattered reemitted light is lost when it is reflected towards the detection arm of the system. However, the use of a polarizing beam splitter cube can significantly improve light efficiency, since almost all of the horizontally polarized laser light will be transmitted to the sample, and 50% of returning light (all of vertically polarized light) will be reflected towards the detector plane.

Specular reflections occur throughout the system and at the air/tissue interface. These reflections can be problematic because their intensity is proportional to the intensity of the incident light and can be much greater than the intensity of the detected light. While the use of anti-reflection coated lenses can help reduce specular reflections, they do not completely eliminate them. Since specular reflections retain the polarization of the incident light, the polarizing beam splitter does not reflect them towards the detection arm. An exception to this occurs when the polarization of the light is altered prior to the specular reflection occurring. Metal and dielectric mirrors do not change the polarization state of the reflection so long as the beam is incident normally on the mirrors or if the plane of polarization lies on or normal to the plane of incidence. However, if the polarization direction makes an angle with the plane of incidence then the reflection makes a small phase shift between $E_{\parallel}$ and $E_{\perp}$. The resulting reflected beam is no longer linear polarized and will be slightly elliptically polarized. Specular reflections from the face of lenses with this slightly elliptically polarized light will mostly, but not completely suppressed by the polarizing beam splitter.

2.1.2 Electronics system

Photomultiplier tubes generate a time varying current based on the intensity of the light incident upon the detector. For each channel of each PMT in LOT (7 fluorescence, 24 absorption) an electronic circuit consisting of a transimpedance amplifier, anti-aliasing filter and secondary stage amplifier was built as shown schematically in Figure 2-5.

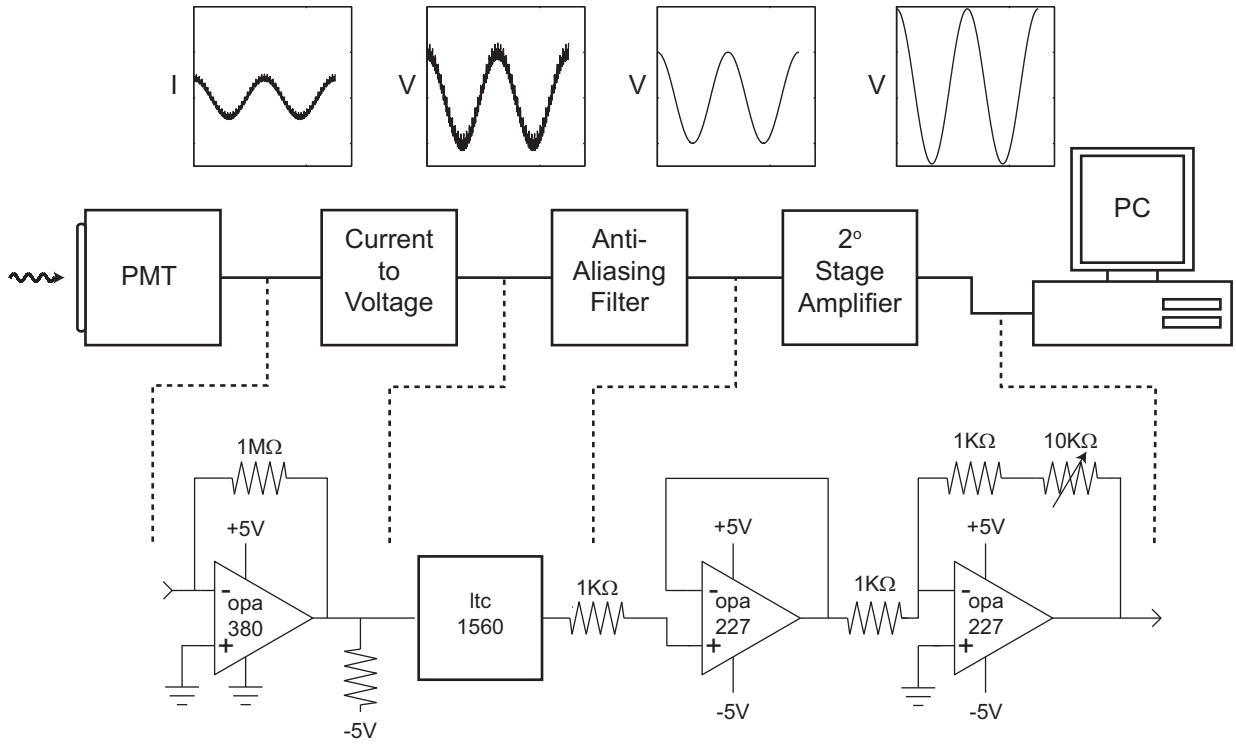

Figure 2-5 LOT System Electronics. Each channel of each PMT has an electronic circuit consisting of a current to voltage stage, anti-aliasing filter, and secondary stage amplifier allowing for simultaneous sampling.

A high-speed transimpedance amplifier (OPA380, Texas Instruments) accepts a current input from the PMT. The variable gain and bandwidth of the transimpedance amplifier is set by the value of the feedback resistor, with larger resistor values providing increased gain at the expense of a lower bandwidth. The desired bandwidth for LOT imaging depends upon the sample rate of the system. In most cases, LOT imaging is performed with a pixel sample rate of less than 1MHz, therefore a bandwidth of 1MHz is sufficient. A pull-down resistor connected between the output of the transimpedance amplifier and the negative supply improves the output voltage swing by allowing it to approach closer to 0V.

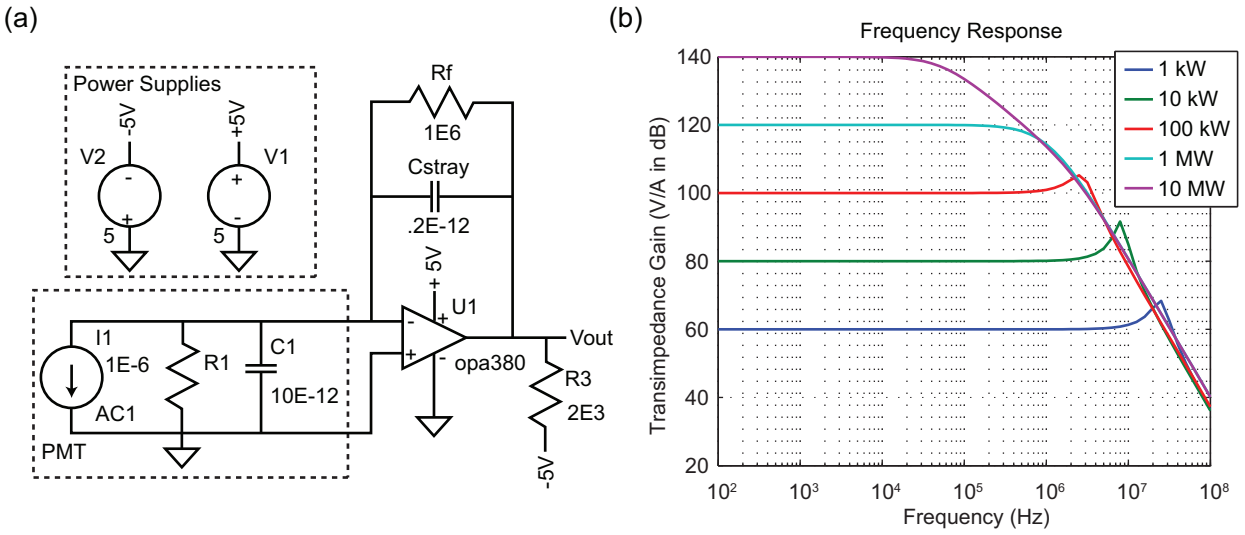

Figure 2-6 (a) LTspice IV model of transimpedance ampflifier stage. (b) Frequency response of model circuit for varying feedback resistor (Rf) values.

The transimpedance amplifier stage was modeled in LTspice IV™ (Linear Technology) as shown in Figure 2-6a. The PMT equivalent circuit consists of a current source in parallel with a resistor and capacitor. Figure 2-6b shows the simulated frequency response of the circuit for various feedback resistor values (Rf). Based on these results, a 1MΩ feedback resistor was selected offering ample gain and bandwidth for a range of LOT acquisition configurations, however future designs could include a switchable feedback resistor to allow for optical gain and bandwidth for specific imaging configurations.

In order to reduce the likelihood of contaminating the low current PMT signals with noise during transmission to the current to voltage stage, a PMT interface board was developed. The 8 layer printed circuit board (PCB) was designed using Advanced Circuits PCB Artist software. The PMT mounts to the interface board through a socket on the back of the board that connects the anode signals and high voltage input to the board. Anode signals from 4 PMT rows, totaling 32 channels, are routed to 32 transimpedance amplifier circuits located on the front of the board.

While LOT currently uses 3 rows (1 for each wavelength), circuits for a 4th row were included on the interface board for future use. The voltage output from each amplifier circuit is routed to a connector on the bottom of the board. A high-density rg178 coaxial cable assembly (EQRF-020-0152-S-R-MCX-P-2, Samtec) connects to the board, transmitting the output signals to an anti-aliasing filter. Figure 2-7 shows a schematic drawing of the pcb layout and photographs of the interface board.

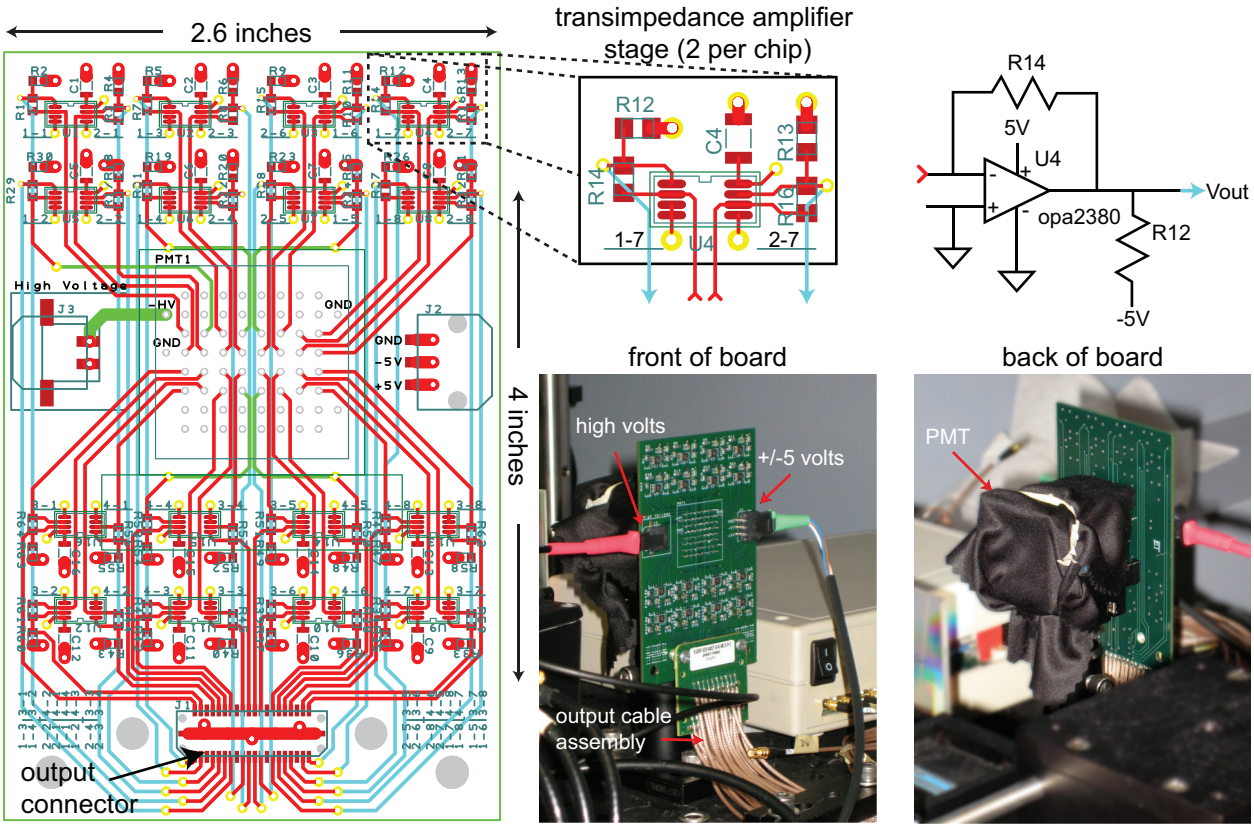

Figure 2-7 Schematic and photograph of PMT interface board. The front of the board contains surface mount components for the 32 transimpedance amplifiers. The back of the board contains a socket that mounts to the PMT.

An anti-aliasing filter stage follows the current to voltage stage. Aliasing occurs when an input signal has frequency components at or higher than half the sampling frequency. These components will show up as aliases or spurious lower frequency components that cannot be

detected from the sampled data. In actuality, the errors are at a higher frequency, but when sampled, appear as a lower frequency, and thus, false information. An elliptical lowpass filter (LTC1560, Linear Technology) was used to filters the data with a selectable cutoff frequency of 500 kHz or 1 MHz. Figure 2-8 shows the frequency response of the lowpass filter obtained by applying a 1 Vpp sine wave to the input and incrementally adjusting the sine wave frequency while recording the filter output.

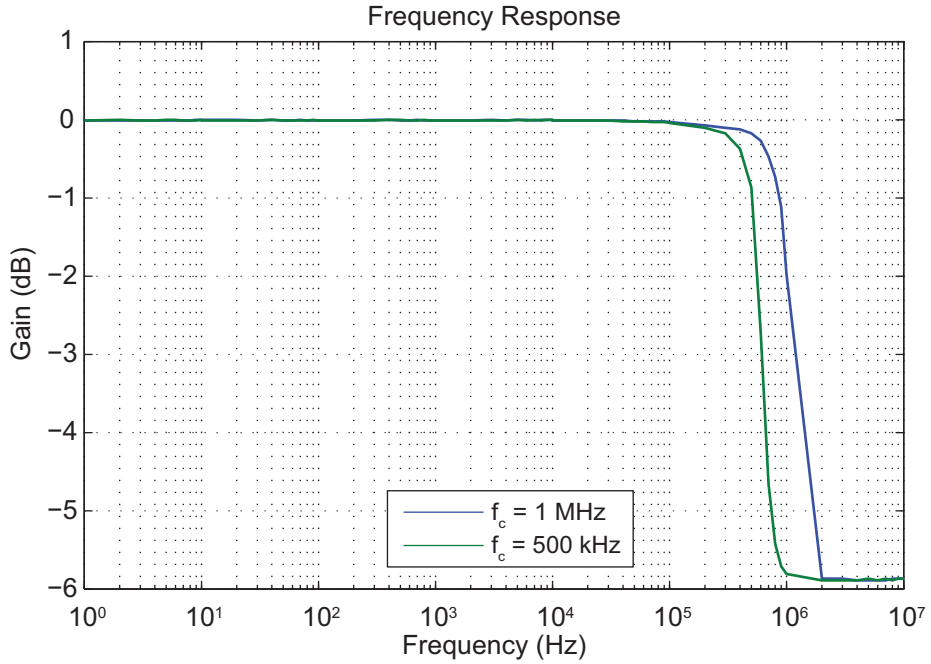

Figure 2-8 Frequency response of the anti-aliasing lowpass filter. The selectable frequency filter offers cutoff frequencies of 500 kHz and 1MHz.

After the signal passes through the anti-aliasing filter a secondary stage amplifier allows for amplification of each individual channel. Because the detected light is de-scanned by the galvanometers, the image of the scanning spot at the PMT array remains stationary but varies in intensity over time as the galvanometers steer the beam over the tissue's surface. Nevertheless, the detectors further from the center of the scanning spot will typically detect lower light levels than those closer to the spot's center. The secondary stage amplifier for each detector can

therefore be adjusted to produce approximately equal voltage output levels when a typical object is being imaged. This provides optimal gain for each channel, reduces the inter-channel cross-talk, and utilizes the full digitalization range of the data acquisition cards.

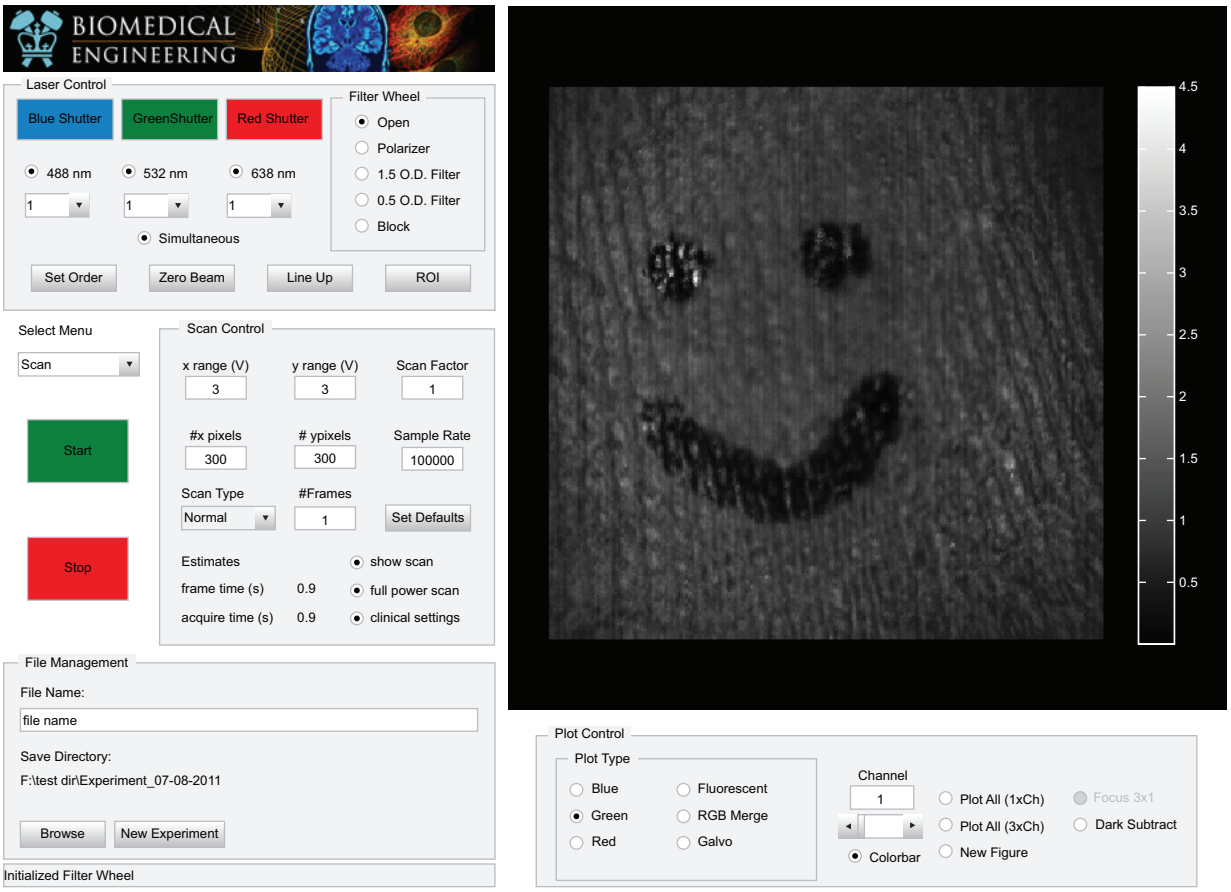

Figure 2-9 LOT system control. A graphical user interface program synchronized data acquisition from the opening of shutters to the movement of galvanometer mirrors and digitization of data. The program also allows users to select scan parameters and visualize acquired data.

A personal computer with a 3.0GHz, Pentium 4 processor and 4GB of RAM is used to acquire data and control the system. The computer contains five data acquisition (DAQ) cards: four 14 bit, 8 channel, simultaneous sampling 3MS/s per channel analog input cards (National Instruments PCI-6133), and a 12-bit, 8 channel, 1MS/s analog output card (National Instruments PCI-6713). All data acquisition is synchronized using a custom designed graphical user interface

(**Figure 2-9**) written in Matlab™ (Mathworks). In addition to synchronizing scan acquisition, the program controls scan parameters such as the number of x and y pixels, pixel acquisition rate, field of view, and laser illumination sequence. The interface also displays the most recent scan images, allowing the user to select different source-detector separations and different wavelengths.

2.1.3 System control

A major challenge for controlling the system was to properly synchronize the movement of the galvanometers with the data acquisition, and to reliably re-order the data stream acquired for each frame into a square image corresponding to the bi-directional scan. This was achieved by synchronizing the DAQ cards such that each output voltage value sent to the galvanometers, and each input read from the PMTs are driven by the same clock signal and therefore issued simultaneously. At very high scan speeds, the limited size of the analog output board's buffer is overcome by driving analog output with a synchronized clock at a lower divisible frequency. Using this synchronized acquisition, frames can be acquired continuously at up to 4500 lines per second for over 20 seconds, limited only by the speed at which data can be streamed to disk. Image reformation is simplified due to the fact that exactly the same number of data points is acquired per line scan. A diagram of the instrumentation control is provided in Figure 2-10.

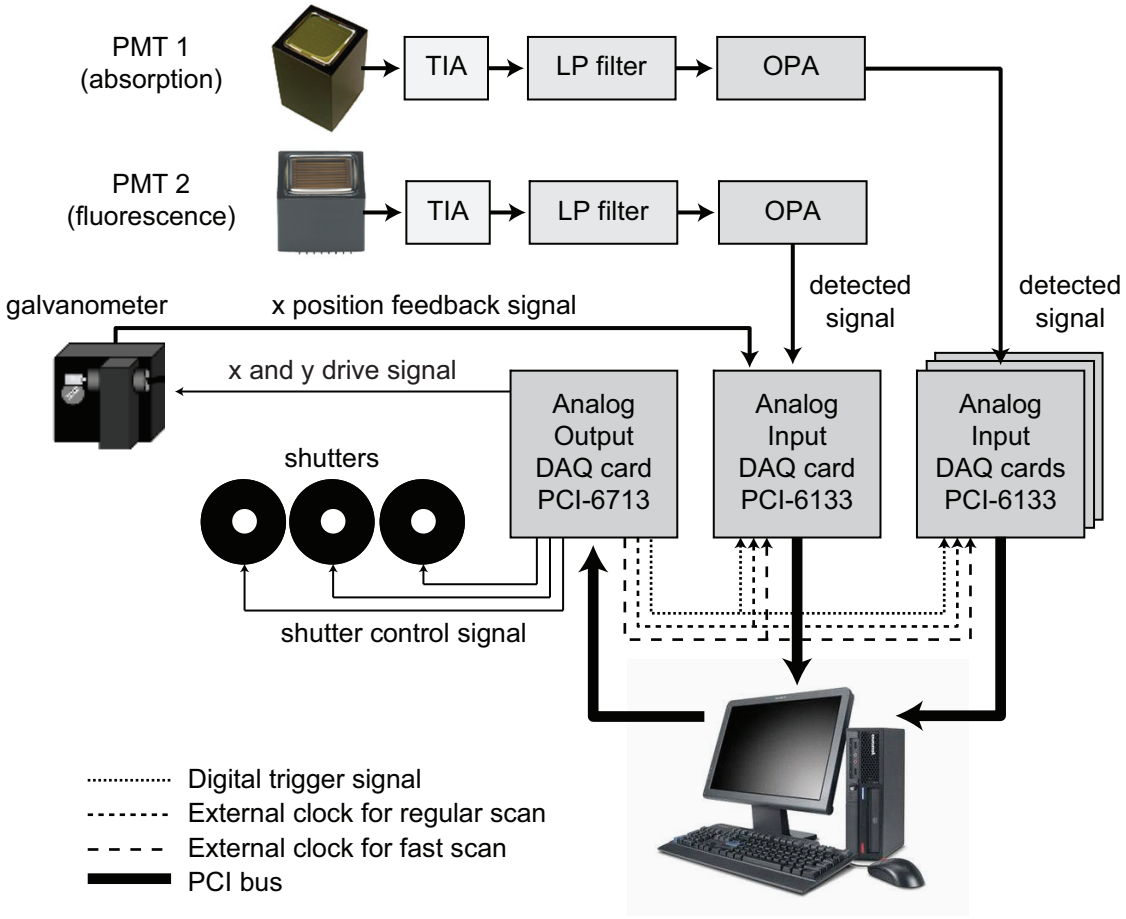

Figure 2-10 Schematic diagram of LOT instrumentation control. An analog output board controls the shutters and galvanometer mirror position. Light detected by the PMTs is converted into a voltage, filtered and sampled by analog input boards. Control software synchronizes the movement of mirrors with data acquisition.

Data acquisition is initiated by a digital trigger signal that is generated by the analog output card. The dotted line in Figure 2-10 indicates the flow of the digital trigger signal. To acquire a single frame with one laser, the analog output card, upon receiving the initiation trigger, opens one of the shutters by sending it a 5 volt signal. At the same time, the analog input cards are initiated by the digital trigger to acquire the data from all the PMT channels as well as the 'x-position' feedback signal available from the galvanometer controller boards. For imaging with multiple lasers, different laser-shutters can be synchronously opened and closed between frames. This sequence can easily be changed, for example, to repeat several frames for the first laser before

switching to another laser. Multi-frame acquisition can occur individually or continuously. For individual scans, the acquired data are stored in the PC memory, reshaped and then immediately displayed on screen. For fast continuous scans, the acquired data is streamed directly to disk, and processed after completion of data acquisition.

2.1.3.1 Image formation

LOT data is collected as a time series of data points. In order to visualize the data in the form of an image, the data must be reshaped based on the scan pattern of the laser beam. In theory, the data can be reshaped knowing only the raster scan pattern and number of pixels in the x and y direction. However, in practice, there is a delay in the galvanometer mirror motion response (see Figure 2-11) that requires the initial data points to be discarded prior to reshaping. Therefore image formation consists of two steps, finding and removing the data points associated with the galvanometer delay and reshaping the raster scan data into a 2-D image.

Cross-correlation is a measure of similarity between two waveforms as a function of a time-lag applied to one of the functions. For discrete signals, $f[m]$ and $g[m]$, the cross-correlation is given by:

$$(f * g)[n] = \sum_{m=-\infty}^{\infty} f^*[m]g[n+m] \qquad \textbf{Eq 2-1}$$

Where f^* is the complex conjugate of f which, for our real data point, is just f and n is the lag ($\pm1, \pm2, \ldots$). If we let f be the galvanometer control signal and g be the galvanometer feedback signal, the cross-correlation will be a maximum when the lag causes the signals to align. Therefore, determining the number of data points to discard from the beginning of the LOT data

set corresponds to computing the cross-correlation between the galvanometer control and feedback signals and finding the lag associated with the maximum in the cross-correlation. After removing the data points, the data set is padded with the mean value of the time series such that the total number of data points remains unchanged. The mean value is used to pad the data to ensure that when the image is displayed, the minimum and maximum values for scaling the colorbar is determined from actual data and not padded data points. The data is then formed into an image by first reshaping it into a px x py matrix. Due to the raster scan pattern, every other column of the matrix is flipped to generate an image.

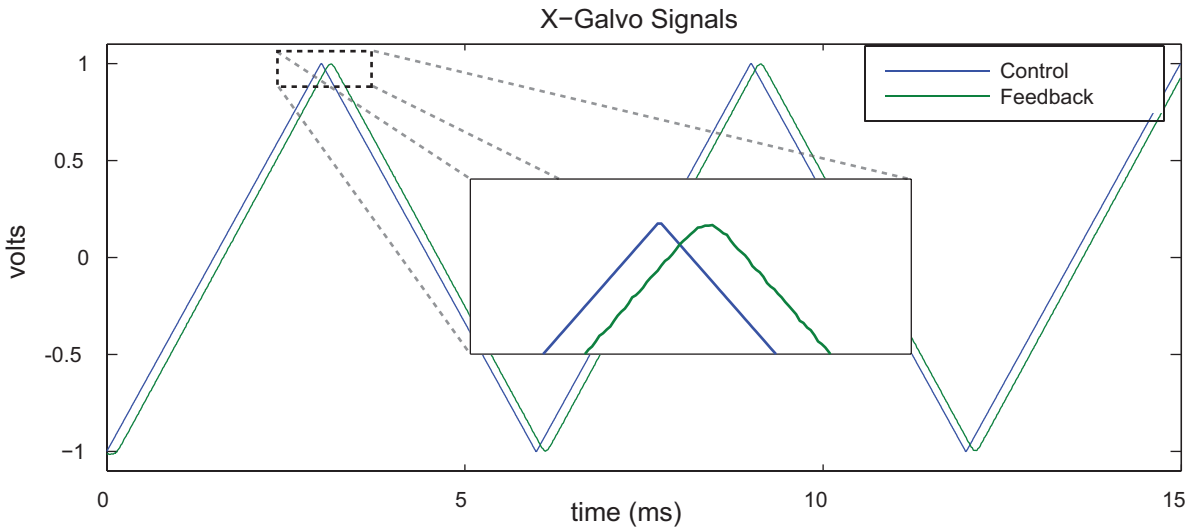

Figure 2-11 X galvanometer mirror control and feedback signals used to determine delay when reshape stream of 1D raster-scanned data into 2D images.

2.1.4 System parameters

2.1.4.1 Optical magnification and source-detector separation

The source-detector separation in LOT is set by the size of the detector and the magnification of the lenses in the system. The optical magnification for the absorption detection arm (m_{abs}) is given by:

$$m_{abs} = \frac{f_{tube}}{f_{objective}} \frac{f_{absL1}}{f_{scan}} \frac{f_{abs\,\mathrm{Im}}}{f_{absL2}} \qquad \textbf{Eq 2-2}$$

where, using Figure 2-2 as a reference, f_{tube} is the focal length of the tube lens, $f_{objective}$ is the focal length of the objective lens, f_{absL1} is the focal length of absorption lens 1, f_{scan} is the focal length of the scan lens, f_{absIm} is the focal length of the absorption image lens, and f_{absL2} is the focal length of absorption lens 2. Similarly, the optical magnification of the fluorescent detection arm (m_{flu}) is given by:

$$m_{flu} = \frac{f_{tube}}{f_{objective}} \frac{f_{flu\,\mathrm{Im}}}{f_{scan}} \qquad \textbf{Eq 2-3}$$

where f_{fluIm} is the focal length of the fluorescent image lens.

Theoretically, the minimum nonzero separation distance between a source and a detector channel on the sample plane (r_{sd_min}) is the distance between two adjacent PMT channels (r_{ch_min}) divided by the optical magnification:

$$r_{sd\_\min} = \frac{r_{ch\_\min}}{m}. \qquad \textbf{Eq 2-4}$$

The maximum source-detector separation distance (r_{sd_max}) on the sample plane is determined by the maximum distance between the two furthest channels on the PMT array (r_{ch_max}).

$$r_{sd\_\max} = \frac{r_{ch\_\max}}{m} \qquad \textbf{Eq 2-5}$$

Therefore, by changing the system magnification, the minimum and maximum source-detector separation distance on the object plane can be easily adjusted to within the limits of the size of the optical elements and achievable signal to noise. Table 2-1 below shows lens configuration used to obtain a 250 μm source-detector separation for both absorption and fluorescence contrast imaging.

Table 2-1. LOT Lens Configuration

Lens Focal Length			
objective:	150 mm	absorption lens 1:	80 mm
tube lens:	200 mm	absorption lens 2:	35 mm
scan lens	50 mm	absorption image lens:	150 mm
fluorescent image lens:	150 mm		
Magnification			
m_{flu}	4	m_{abs}	9.143
PMT Specifications			
fluorescent PMT pitch (r_{ch_min})	1 mm	absorption PMT pitch (r_{ch_min})	2.3 mm
number of channels	16	number of channels	8
Source-Detector Separation			
fluorescent ($r_{sd\ min}$)	0.250 mm	absorption ($r_{sd\ min}$)	0.251 mm

2.1.4.2 Field of view

The field of view of LOT refers to the full imaging region on the surface of a sample that is scanned by the incident laser beam. The size of field of view is restricted by the physical size of

the scan lens, which apertures the scanning beam. The amount of linear displacement (d) of the focused beam for a given angular deviation of the galvanometer mirrors (θ) is given by:

$$d = M_{obj} f_{scan} \tan(2\theta), \qquad \textbf{Eq 2-6}$$

where f_{scan} is the focal length of the scan lens and M_{obj} is the magnification power of the objective (see Figure 2-12a).

When imaging dynamic changes, the size of the field of view may become limited by the galvanometers' scanning speed. While the x-galvanometer is driven using a bidirectional triangular wave, at high speeds, the mirrors are unable to reach the limits of this motion, smoothing the effective triangle wave and reducing the system's field of view. Ultimately, the galvanometer mirrors will fail at high speeds once they exceed an acceleration level governed by the mirror size and their ability to dissipate heat. The galvanometers provide an analog feedback signal that indicates the true position of the galvanometer mirrors. Figure 2-12b shows the results of driving the galvanometer mirrors, where the maximum drive-signal voltage is compared to the actual maximum feed-back position voltage for a range of different line-scan speeds. For these mirrors, 1 volt of drive voltage represents 2 degrees of mirror motion. The plot demonstrates that for slow scans, such as 100 lines/second, the input voltage can reach 9 volts without distortion. However, for faster scanning at 6000 lines/second, the input voltage can only reach 1.5V without significant distortion, and ultimately failure of the mirrors at above 2.5V. A typical LOT scan requires no more than a 3V galvanometer input signal resulting in a maximum linear line-scan speed of 4500 lines/second.

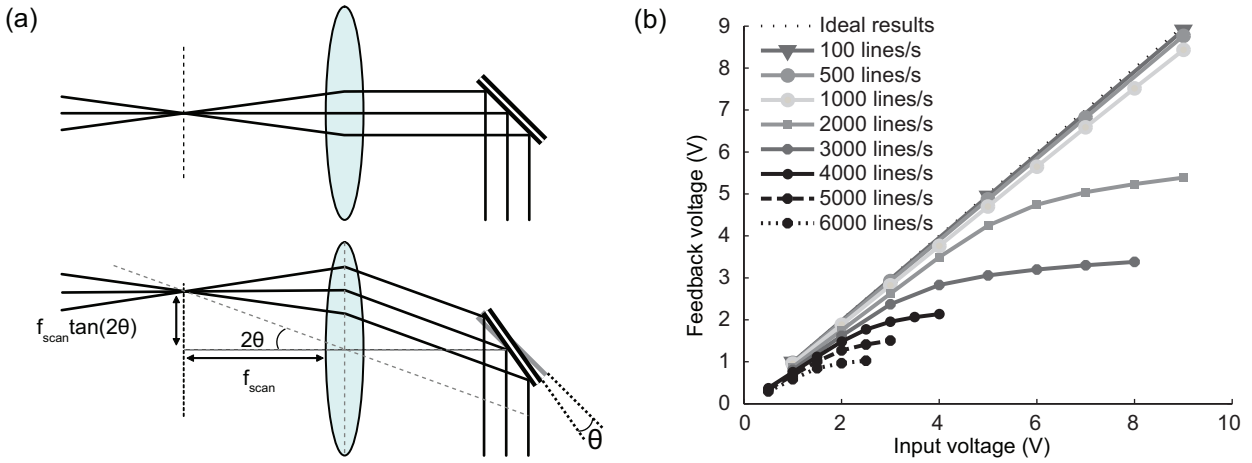

Figure 2-12 Effects of galvanometer scan angle and speed. (a) Changing the angle of the collimated light entering the scan lens causes a lateral scan of the focus in the primary image plane. (b) The angular deviation of the galvanometer determines its maximum speed. The feedback voltage from the galvanometers represents the real position of the galvanometer. The galvanometers will fail at scan angles (input voltages) that exceed the limit for a given line-scan speed.

2.1.4.3 Image acquisition speed

The speed of the system is limited by the number of lines that the galvanometers can scan in a second and the data acquisition board sample rate. In order to determine which of the two is limiting, the sample rate and maximum galvanometer mirror line scan rate must be known (4500 lines/second). For example, if the data acquisition board sample rate is set to 325 kHz, and a 100 x 100 pixel frame is to be acquired, the sample rate limiting frame rate (FR_{sample}) is

$$FR_{sample} = \frac{f_s}{px^2} = \frac{325000 samples/\sec}{100^2 samples/frame} = 32.5 \frac{frames}{\sec} \qquad \textbf{Eq 2-7}$$

Where f_s is the sample rate and px^2 is the number of pixels per frame. The scan rate limiting frame rate (FR_{scan}) is

$$FR_{scan} = \frac{f_l}{l} = \frac{4500 lines / \sec}{100 lines / frame} = 45 \frac{frames}{\sec} \quad \textbf{Eq 2-8}$$

Where f_l is the maximum line scan rate and l is the number of lines per frame. In this scenario, the data acquisition board sample rate is limiting the maximum frame rate to 32.5 frames/second. If the number of pixels in the frame is reduced to 45 x 45 pixels, a frame rate of 100 frames/second is achievable as limited by the galvanometer line scan rate.

The ability to acquire frames rapidly is important for *in vivo* measurements, where motion artifacts can be problematic.

2.2 Calibration

2.2.1 Calibration of source-detector separations

As described above, the anticipated distance between the incident and detected light at the tissue surface, for each detector channel, can be calculated based on the lenses and alignment of the system. However, in practice, the true values of the separations may deviate from the expected values, and it is critical to know the actual physical separations for quantitative analysis of LOT data [59]. Accurate measurement of the source-detector separation distances, as well as the system's field of view, can be obtained by imaging a translucent ruler against a scattering background. Figure 2-13 shows 'raw' LOT images of such a ruler. The most striking aspect of the images is the appearance of a shadow of the ruler in the wider detector channels. As the source beam scans over a dark line on the ruler, the amount of detected light decreases, creating the darker image of the ruler. However, when the imaged position of the detector coincides with

a dark line on the ruler, the amount of scattered light detected also decreases. The shadow, therefore, corresponds to the point when the detector position is passing over the lines on the ruler and the distance between the primary lines and the shadows in each image correspond to the effective source-detector separation in the object plane. Overlaid on each image in Figure 2-13 is a plot of the average pixel value down the columns of the image in the tic mark region. Dips in the plots correspond to tic marks and shadows in the image. These plots aid in calculating the pixels per millimeter in the image as well as the individual source-detector offset distance. While these empirical results usually agree well with the predicted separations based on the system design, a ruler scan is typically acquired before or after each LOT measurement session to ensure that the relative positions of the source and detector positions within the system are carefully recorded for each dataset.

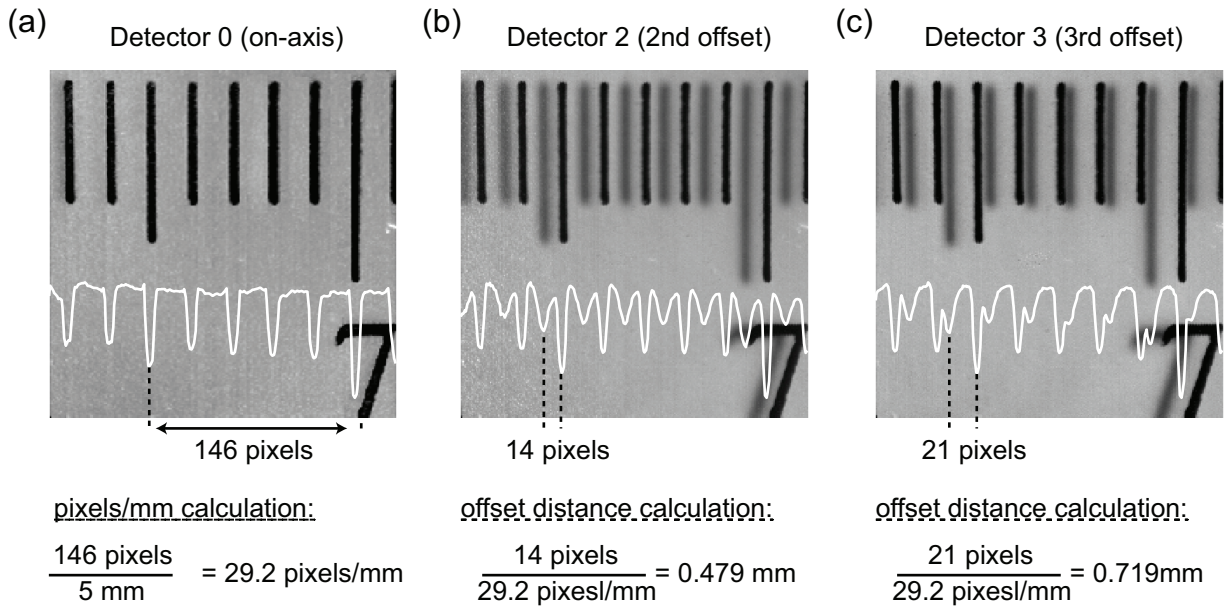

Figure 2-13 LOT ruler calibration scan. Tic marks appear in the image when the source is positioned over the ruler tic-mark while shadows appear when the detector is positioned over the tic-mark. When the detector and source are aligned (a) no shadow appears. When the detector is offset from the source (b and c), the source-detector distance is indicated by the shadow distance in the image. The distance is determined by measuring the shadow distance in pixels, and using the pixels to length conversion.

2.2.2 Calibration of LOT data

'Raw' LOT data is affected by various systematic errors and can be modeled by the following equation:

$$M_{s,d} = g_d \left(S_{s,d} + R_{s,d} + D_d \right), \qquad \textbf{Eq 2-9}$$

where $S_{s,d}$ is the true data for source position s and detector d, $R_{s,d}$ is the signal contributed by reflections from intermediate optics, D_d is the amount of signal contributed by the background and stray light of detector d, and g_d is the gain contributed by the detector d and its associated electronic circuit (transimpedance amplifier, lowpass filter, secondary stage amplifier). In order to compensate for these factors, the following additional calibration scans are captured: A 'no sample' scan is performed in which the sample is removed from the scan plane resulting in a data set with information about the gain, reflections and background. Subtracting the 'no sample' scan from the sample scan results in the measurement:

$$g_d \left(S_{s,d} + R_{s,d} + D_d \right) - g_d \left(R_{s,d} + D_d \right) = g_d S_{s,d}, \qquad \textbf{Eq 2-10}$$

A 'no laser' scan is performed resulting in a data set with information about the gain and background and a 'light' scan is performed in which a uniformly illuminated surface is scanned without lasers resulting in a data set with information about the gain, intensity of light (L) and background. Subtracting the 'no laser' scan from the 'light scan' yields:

$$g_d \left(L + D_d \right) - g_d D_d = g_d L, \qquad \textbf{Eq 2-11}$$

Dividing the results of Eq 2-10 by the results of equation Eq 2-11 provides data that represents the sample scaled by a constant. Figure 2-14 shows this sequence of operations performed on an LOT scan of a piece of thread embedded in a homogenous scattering background medium.

For cases in which the percent change in signal is the desired measure, the number of calibration scans can be reduced to only the 'no sample' scan. The percent change is calculated by:

$$\frac{M_1 - M_0}{M_0 - M_{ns}} = \frac{s_{1s,d} - S_{0s,d}}{S_{0s,d}}, \qquad \textbf{Eq 2-12}$$

where M_1 is a scan of the region of interest, M_0 is a scan of a reference region (or the same region at a different time).

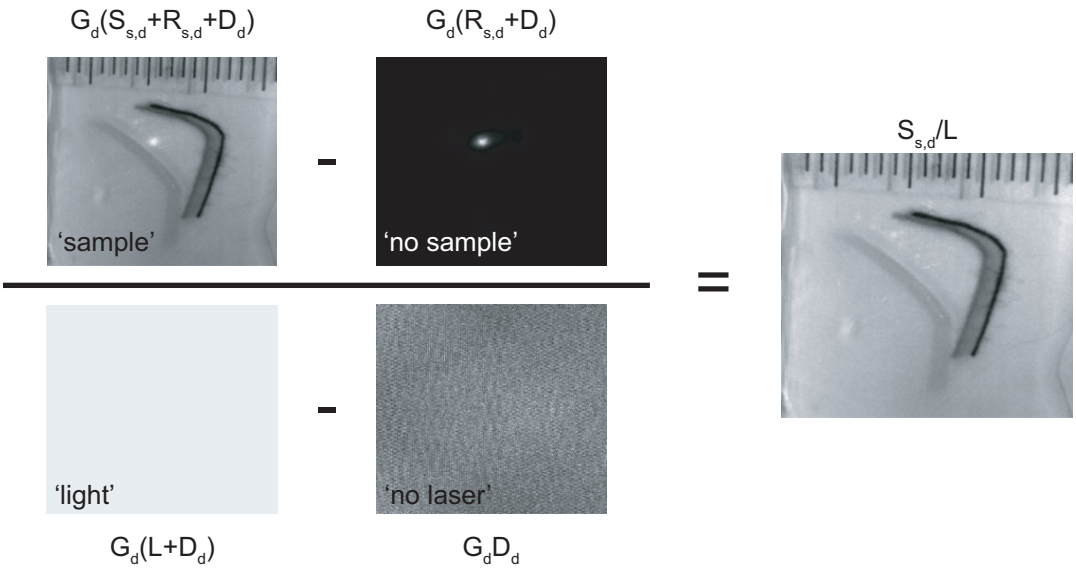

Figure 2-14 Calibration of LOT data. 'Raw' data (one separation) showing two cotton fibers of different colors at different depths ('sample'). 'No sample', 'light' and 'no laser' scan are used to form a calibrated image. The bright dot in the 'no sample' scan is a system reflection. The calibrated image is shown on the right.

2.3 Phantom Studies

Sections 2.1and 2.2 described the development of the multi-wavelength LOT system and calibration of LOT data. This section describes a set of phantom experiments that were performed to demonstrate the instruments ability to simultaneously capture depth sensitive multi-wavelength measurements and to test how well calibrated data from LOT matches data simulated using Monte Carlo modeling.

2.3.1 Phantom design

LOT measurements rely on scattering in tissue to generate re-emitted light in order to detect local changes in absorption or fluorescence. Optical phantoms for testing LOT should, at a minimum, consist of absorbing or fluorescent perturbations imbedded within a scattering medium. An agarose gel-based phantom with stackable layers was therefore developed to allow for controlled placement of perturbations within the phantom. The phantoms were made of 2% agarose (weight/volume) in distilled water with Intralipid™ added as a scattering material and various absorbing materials added based on the application. Agarose is a polysaccharide obtained from agar and is used in a variety of life science applications. When mixed with water, heated above its transition temperature, and subsequently cooled, the agarose solution forms a transparent gel whose mechanical properties are governed by the agarose concentration. Intralipid™ is purified soybean oil, which is commonly used as an intravenous nutrient. It is an ideal medium for light scattering as it has very low absorption, can be easily diluted to provide a range of scattering coefficients, and is cheaply available. Intralipid™ is usually obtained as a 10% or 20% solution (g of purified soybean oil per ml of Intraplipid™). The optical properties

of Intralipid™ have previously been studied by Flock [70] and van Staveren [71]. For wavelengths used in LOT, the work by van Steveren is more applicable. They found that the scattering coefficient (μ_s) dependence on wavelength (λ in nm) was given by:

$$\mu_S(\lambda) = \left(2.54\times10^{9}\,\lambda^{-2.4}\right), \qquad \textbf{Eq 2-13}$$

and the anisotropy factor (g) was given by:

$$g(\lambda) = 1.1 - \left(0.58\times10^{-3}\right)\lambda\,, \qquad \textbf{Eq 2-14}$$

for 1% solutions of 10% Intralipid™.

Assembly of the gel phantoms is as follows: A solution of 2% agarose in water is mixed and heated above the agarose transition temperature. While cooling, Intralipid™ and absorbing chromophores are added and mixed. The liquid phantom solution can then be poured into a mold and allowed to set. Thin slices of known thickness were realized by first preparing the liquid phantom solution as described above. During the cooling process, the liquid phantom is sandwiched between two microscope slides along with cover slips as shown in Figure 2-15a,b. This technique is similar to that used by [72] in which the thickness of the coverslips determines the thickness of the phantom sheet. After fully cooling, the sheet of phantom gel can be cut into small perturbation squares or used as layering sheets as shown in Figure 2-15d. Using the same base material for the background and perturbations minimizes the refractive interfaces between the two.

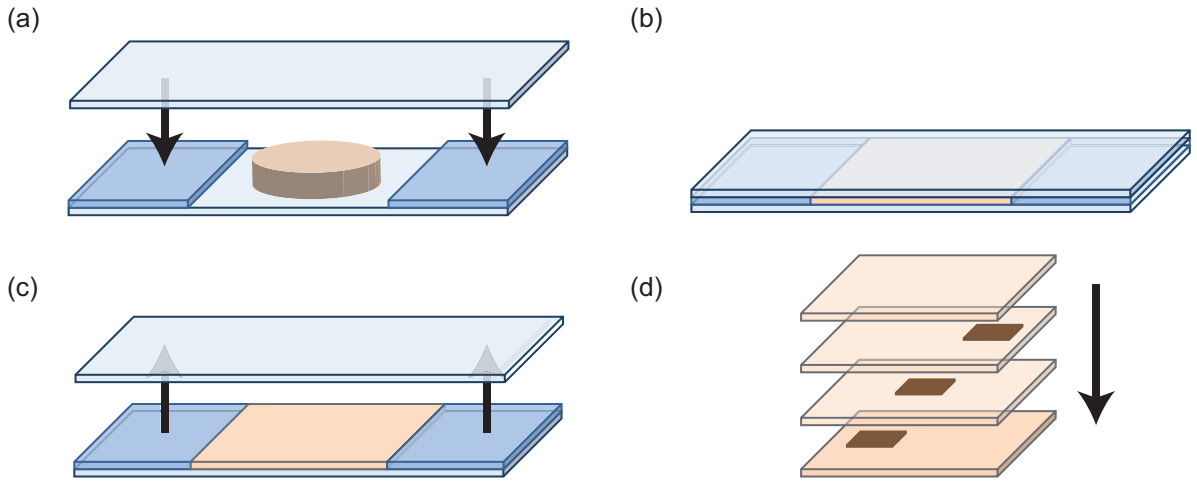

Figure 2-15 Making Phantom Layers. (a-c) Glass cover slips and liquid phantom are sandwiched between microscope slides with thickness of cover slip determining thickness of the phantom sheet. (d) Solidified sheets and absorbers to assemble phantom.

2.3.2 3-Color / multispectral phantom

In order to test the system's ability to simultaneously acquire LOT data at multiple wavelengths, a 3-color phantom was assembled. An agarose gel based phantom was made using 2% agarose, bovine hemoglobin (100714, MP Biomedicals) and Intralipid™ (I141, Sigma). Sufficient hemoglobin and Intralipid™ were added to provide background absorption and reduced scattering coefficients at 532 nm of 0.2 mm^{-1} and 1 mm^{-1} respectively. Thin, 0.1 mm thick sheets of red, green, and blue colored transparency sheets (C-Line Products, Inc) were cut into 5 x 5 mm pieces and embedded in the phantom at depths of 0.2, 0.4, and 0.6 mm. The perturbation depths were controlled by layering transparency films with 0.2 mm thick sheets of phantom gel. A schematic drawing of the phantom is shown in Figure 2-16a.

The LOT system was set up to acquire 200 x 200 pixel images at 23 frames per second and a 20 x 20 mm field of view. Multi-spectral absorption data was simultaneously acquired at 488, 532, and 638 nm with 0.25 mm source-detector offset increments. The data from 30 frames was reshaped into images and averaged.

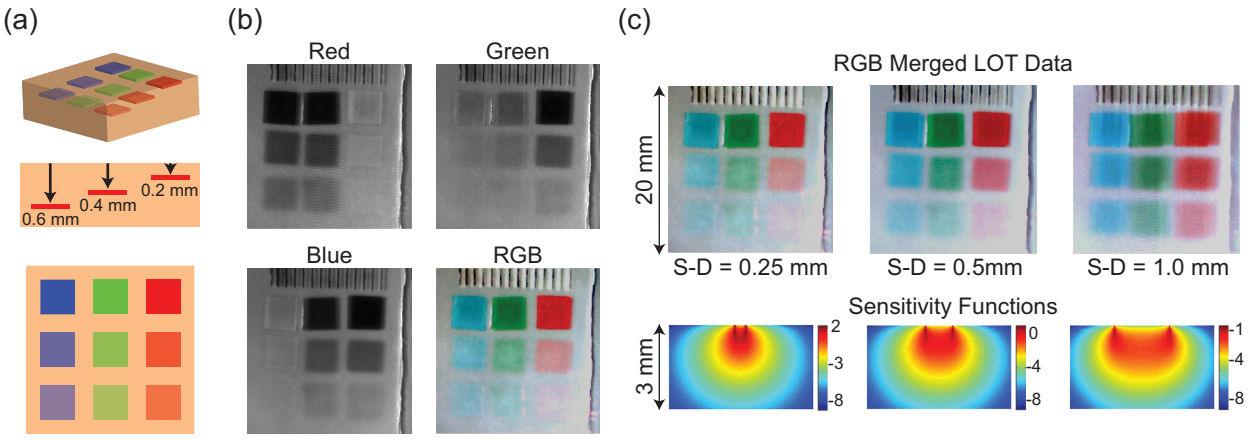

Figure 2-16 (a) Schematic diagram of 3-color phantom. (b) 'Raw' multi-wavelength merged into a single red-green-blue (RGB) image. (c) RGB merged data for various source-detector separation distance and their associated sensitivity functions.

Figure 2-16b shows 'raw' LOT images from the 0.25 mm source-detector separation channels. The 638 nm data (red) shows highest contrast for the green and blue absorbers while the 488 nm (blue) and 532 nm (green) data show higher contrast for the green and red absorbers respectively. A color image was formed by merging the data from each wavelength into the red, green, and blue channels of an RGB image. While the RGB merge provides a photograph-like image for visualization of the phantom, it should be noted that for 'raw' LOT data, each laser wavelength has slightly different depth sensitivities.

Figure 2-16c shows RGB-merged LOT 'raw' data for three different source-detector offsets. A small piece of transparent ruler (with millimeter gradations) was placed onto the phantom's surface for scale. Superficial absorbers in the 0.25 mm separation image show strongest contrast with the deeper absorbers being less apparent. As the source-detector offset increases, the photons probe deeper into the tissue and the deeper absorbers become more apparent owing to the increasing depth sensitivity of the larger source-detector separation images. The greater uncertainty in the path travelled for light detected by the wider offset detectors manifests as

blurring in the 'raw' data images. The wider offset images also have a shadow to the right of each absorber and on the tic marks of the ruler. This shadow is indicative of the source-detector separation distance, as described in Section 2.2.1, and constitutes part of the quantitative depth-specific information provided by LOT. Figure 2-16c (bottom) shows simulated measurement sensitivity functions for detectors positioned at 0.25, 0.5 and 1 mm from the source. These sensitivity functions represent the probable light path within the background agarose gel, and were generated using Monte Carlo modeling [1, 73].

2.3.3 Fluorescent phantom

A phantom designed similarly to the 3-color phantom was made to demonstrate the system's ability to acquire fluorescence measurements. The background medium had the same optical properties as described above. Although, rather than imbedding absorption perturbations, 0.2 mm thick fluorescent sheets were made and cut into 6 x 6 mm squares and embedded to depths of 0.2, 0.4 and 0.6 mm. The fluorescent sheets were made by adding fluorescein to the liquid gel prior to solidifying. A schematic diagram of the phantom is shown in Figure 2-17.

The phantom was imaged with LOT using only a 488 nm laser, with all other acquisition parameters remaining the same as used with the 3-color phantom. The top row of Figure 2-17 show 'raw' LOT data for 3 source-detector separations from the blue backscattered light detection channels. The fluorescent squares appear dark in these channels because the squares absorb the blue light. After absorbing the blue light, fluorescein in the squares become excited and de-excite by fluorescence emission. This fluorescence emission is detected by the fluorescence detection arm and is shown for 3 source-detector separations in the bottom row of Figure 2-17. As with the blue absorption measurements, the more deeply embedded fluorescent

square is more apparent in the wider source-detector separation 'raw' data image owing to the wider detector's sensitivity to more deeply scattered light absorption and subsequent fluorescent emission.

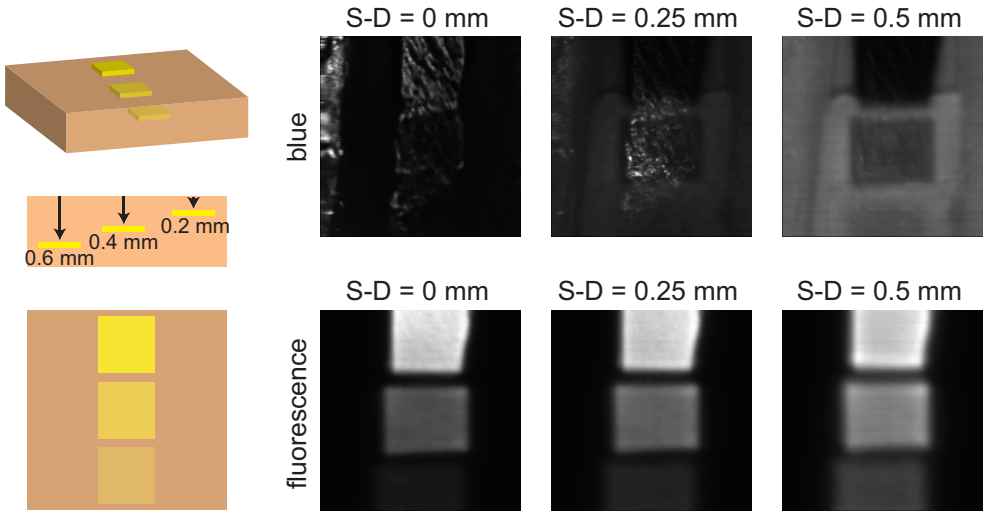

Figure 2-17 Fluorescent phantom schematic diagram (left) and 'raw' data (right). Imaging was performed using a 488 nm laser while simultaneously measuring blue backscattered light and fluorescent light emitting from the sample.

2.3.4 Skin mimicking phantoms

LOT's measurements constitute a 'tomographic' data set containing quantitative information about the depth and optical properties of the tissue being imaged [74]. A second set of absorption contrast experiments were performed to demonstrate LOT's ability to quantify the properties of an absorber at different depths. Absorbers, composed of 0.2 mm thick squares of 2% agarose, Intralipid™ and instant coffee, were embedded in the phantom at depths of 0.2, 0.4, and 0.6 mm (see Figure 3). The absorption and reduced scattering coefficients of these inclusions at 532 nm were 5 mm^{-1} and 1 mm^{-1} respectively (mimicking the optical properties of a melanotic skin lesion). The phantom was imaged using LOT with the 'raw' data from 30 frames averaged.

Monte Carlo modeling of the phantom geometry was performed for comparison with the LOT measurements [73]. The phantom was modeled as a multilayered medium, with each layer having the background optical properties of the phantom. For each photon in the simulation, the distance travelled in each layer as well as the exit position (where the photon leaves the medium) was recorded. Simulated measurements for each source-detector separation distance were calculated by selecting photons with exit locations at a given source-detector separation distance and then using the Beer-Lambert Law to calculate the measured light intensity. By varying the absorption coefficient of a given layer and/or by varying the layer in which the optical properties are changed, simulated measurements for a range of geometries can be calculated from a single model.

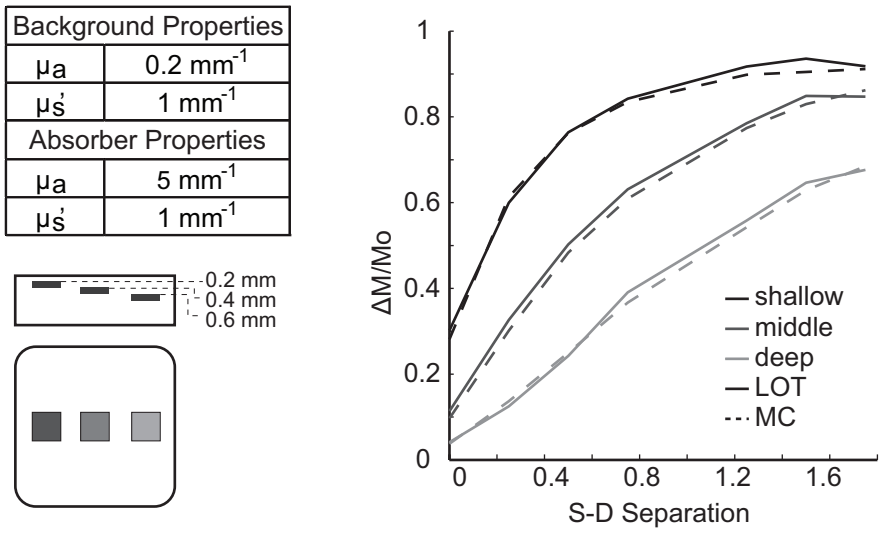

Figure 2-18 Skin mimicking phantom geometry and optical properties (left) and plot comparing LOT data to Monte Carlo simulation data (right).

Figure 2-18 shows a drawing of the phantom and plots of the LOT measurements and simulated values. The plots show the fractional change in measurements $(M_a-M_o)/M_o$ where M_a and M_o are the averages of 10 x 10 pixel regions overlaying each absorber and a background region, respectively. Agreement between the LOT data and simulation data was was confirmed using a

look-up table approach, where forward data were simulated for all three depths, and a range of absorption contrast from 1 to 10 mm^{-1}. By fitting the data to these simulated values, the depth of each object was correctly predicted and its absorption properties were estimated to within ± 1 mm^{-1}.

2.3.5 Summary

This section described the design and construction of phantoms for LOT imaging. The resulting phantoms were used to demonstrate LOT's ability to acquire multispectral absorption and fluorescence measurements. Quantitative comparison of LOT data collected from a skin mimicking phantom and Monte Carlo simulated data was then described. The next section describes the development of an interface for performing LOT imaging in the clinic.

2.4 Development of clinical interface

The LOT system described thus far has been implemented in a bench top configuration. In order to perform *in vivo* clinical imaging, in which areas other than the hands and arms are to be imaged, a clinical interface was developed. The requirements for the interface were that it allowed access to external surfaces of the body, it did not cause the patient any discomfort, it was easy to position/operate, and it was easily sterilized. Two different implementations were explored: an articulating arm setup and fiber bundle setup. The following sections describe the implementation of each configuration and a study performed to compare the ability of each setup to acquire LOT data.

2.4.1 Articulating arm

The articulating arm was implemented by positioning 2” pivot mirrors (BB2-EO2, Thorlabs) distal to the scan lens as shown in Figure 2-19. Pivot mirror 1 was mounted in a 2” cube (LC6W, Thorlabs) which was connected to a set of 60mm, SM2 cage plates (LCP01, Thorlabs) via lens tube couplers (SM2T2, Thorlabs) allowing the cube to rotate. Pivot mirrors 2 and 3 were mounted in right angle kinematic cage mounts (KCB2, Thorlabs) which were attached to extension tubes. Rotation by each of the pivot mirrors provides three degrees of freedom.

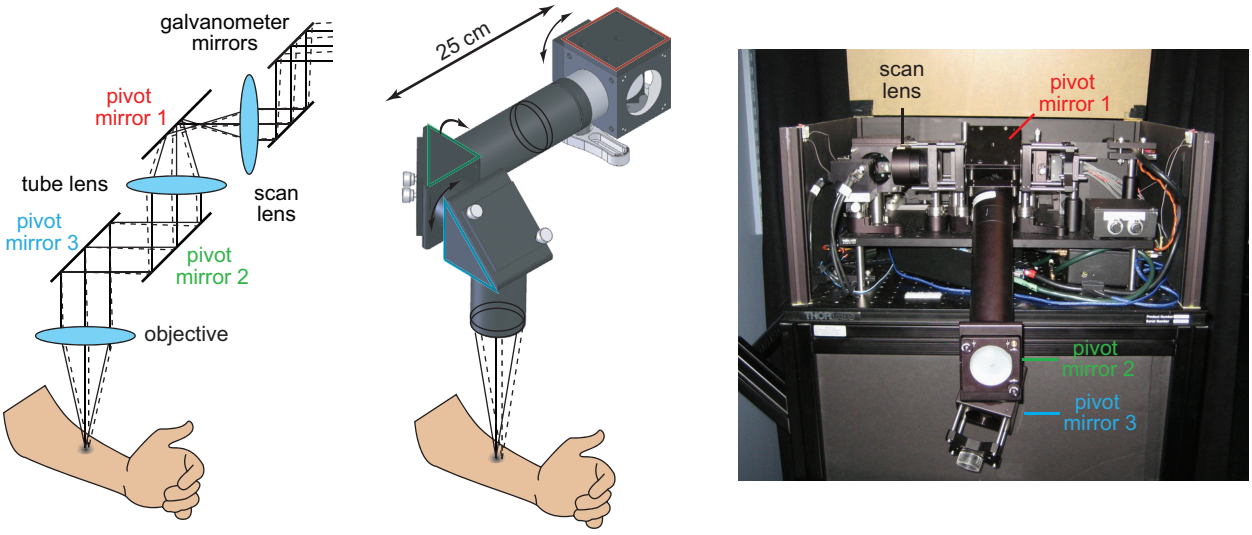

Figure 2-19 Schematic drawing of articulating arm. Pivot mirrors positioned aft the scan lens couple the intermediate image plane to the sample plane with three degrees of freedom.

In order to limit system modifications to components distal to the scan lens, lenses in the articulating arm were selected such that the magnification, and resulting size of the image formed in the intermediate image plane, remained the same. By keeping the magnification unchanged, the source-detector separation distances do not change and modification (as well as associated realignment) of system components proximal to the scan lens is not necessary. The overall length of the articulating arm is limited by the length of the collimated space between the tube lens and the objective. Within this space, the off-axis displacement is translated into an

angular deviation which, for longer collimated space lengths, can result in clipping of the transmitted and remitted light. The use of longer focal length lenses reduces the angular deviation in the collimated space for a given offset displacement. This is beneficial for preventing light clipping making them desirable for the tube and lens objective lenses. However, longer focal length lenses reduce the system's numerical aperture thereby reducing sensitivity and signal to noise while also changing photon migration paths within the tissue. Despite this tradeoff, 2" diameter lenses and mirrors are used throughout the articulating arm as they allow for a longer articulating arm that is better suited for clinical imaging.

To optimize the optical paths in the system, an LOT ray tracing program was developed using Matlab™. The purpose of the program is to verify how and where clipping might occur for different focal length lenses and under various image acquisition settings. A screen shot of the user interface is shown in Figure 2-20(a). The user can set the diameter and focal length of all lenses, the sizes of the polarizing beam splitter, dichroic beam splitter, and galvanometer mirrors, the number and pitch of the detector channels, the spacing between components, as well as the angle of the galvanometer mirror. Figure 2-20(b) illustrates how the simulation can be used to determine that, for this lens configuration, clipping of the incident beam will occur when the galvanometers scan to an angle of 6 degrees, corresponding to a field of view of 16 x 16 mm. Visualizing the returning light path reveals that clipping of the returning beam is more restrictive. Figure 2-20(c) shows that when the galvanometer mirrors are positioned at an angle of 5 degrees, corresponding to a field of view 13.2 x 13.2 mm, the incident light reaches the sample plane, but clipping of the returning light occurs. In order to scan a 13.2 x 13.2 mm field of view, the distance between the tube lens and objective must be reduced to less than 500 mm.

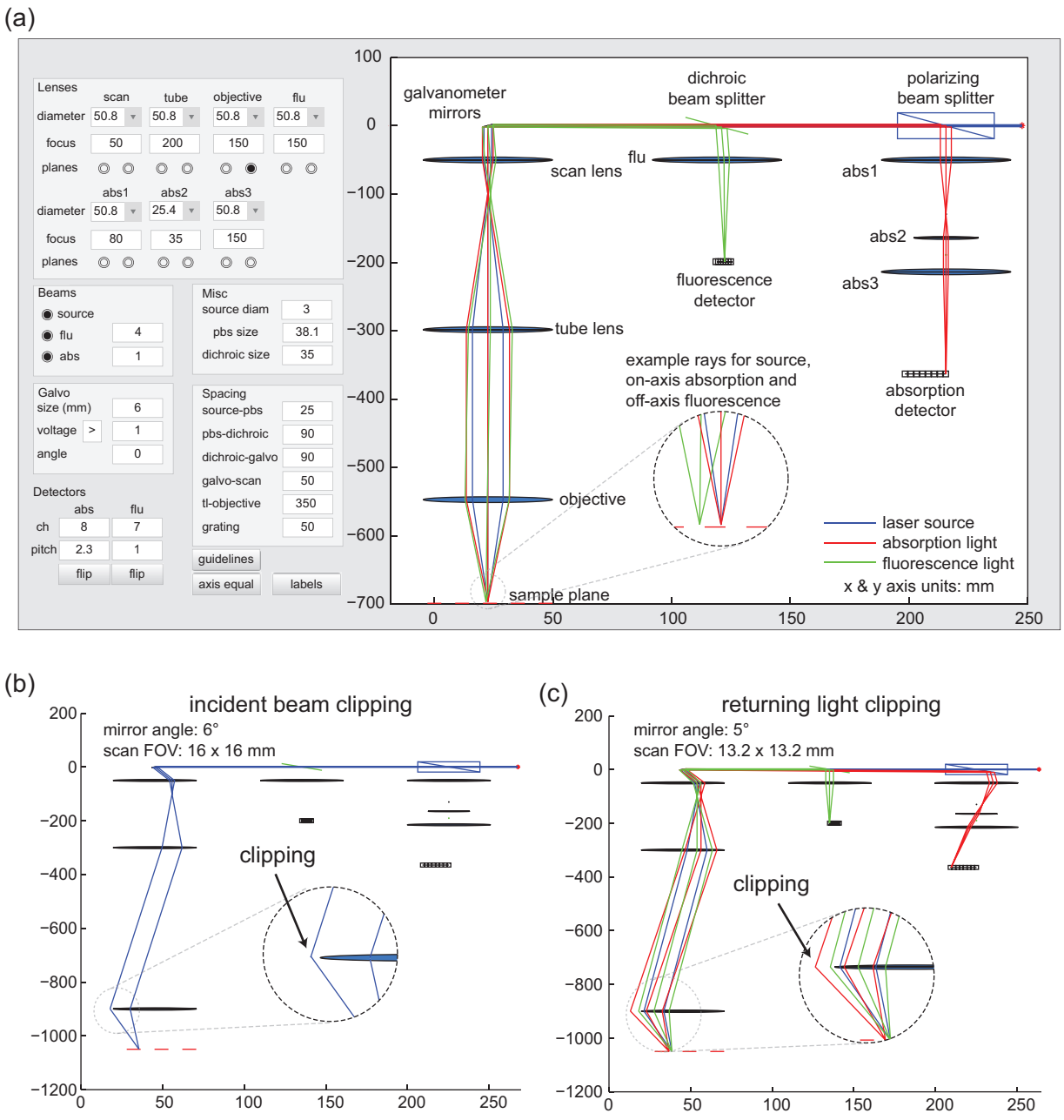

Figure 2-20 Screenshots of LOT ray tracing software. (a) Ray tracing for the incident source light (blue), remitted absorption light (red) and emitting fluorescence light (green). (b) Clipping of the incident light is observed when the galvanometer mirrors are rotated during a scan. (c) Clipping of the off-axis returning light during a scan. All axes are shown in millimeters.

A valuable feature that was incorporated into the system for clinical studies was a 'field if view indicator'. Since moving the articulating arm causes the field of view to rotate, the LOT control software was modified to trace a bounding box with an attenuated beam, generating a square

outline to delineate the region that will be imaged. This region of interest indicator also serves to ensure that the incident light is not being clipped prior to imaging.

2.4.2 Fiber bundle

While the articulating arm configuration improved tissue accessibility, a more flexible patient interface and a step towards *in vivo* imaging of internal organs was achieved by implementing LOT through a fiber bundle (Figure 2-21). The configuration was realized by placing a 4 ft imaging fiber bundle (IG-163, Schott) in the intermediate image plane formed by the scan lens. The 8 mm x 10 mm format bundle, with individual core spacing of 10 μm, couples the intermediate image plane to a position closer to the sample plane. An objective lens positioned at the distal end of the fiber (nearest the sample plane) focuses light to and from the sample. As the galvanometers scan the incident light over the proximal face of the fiber bundle, light is selectively transmitted down different fibers forming a moving source on the distal fiber face. The imaging head images the moving source onto the surface of the sample while also imaging backscattered light emitting from the sample back onto the distal face of the fiber bundle. The fiber bundle transmits the backscattered light to the scan lens intermediate image plane where it emerges and continues along the light detection path.

As with the articulating arm implementation, system modifications were limited to components distal to the scan lens. The lenses used in the imaging head were selected to keep the image size in the scan lens intermediate image plane the same, however since light clipping is not as problematic as with the articulating arm, smaller diameter and shorter focal length lenses were used in the imaging head, allowing it to be more compact. The higher numerical aperture of the shorter focal length lenses permits higher light collection efficiency by the imaging head.

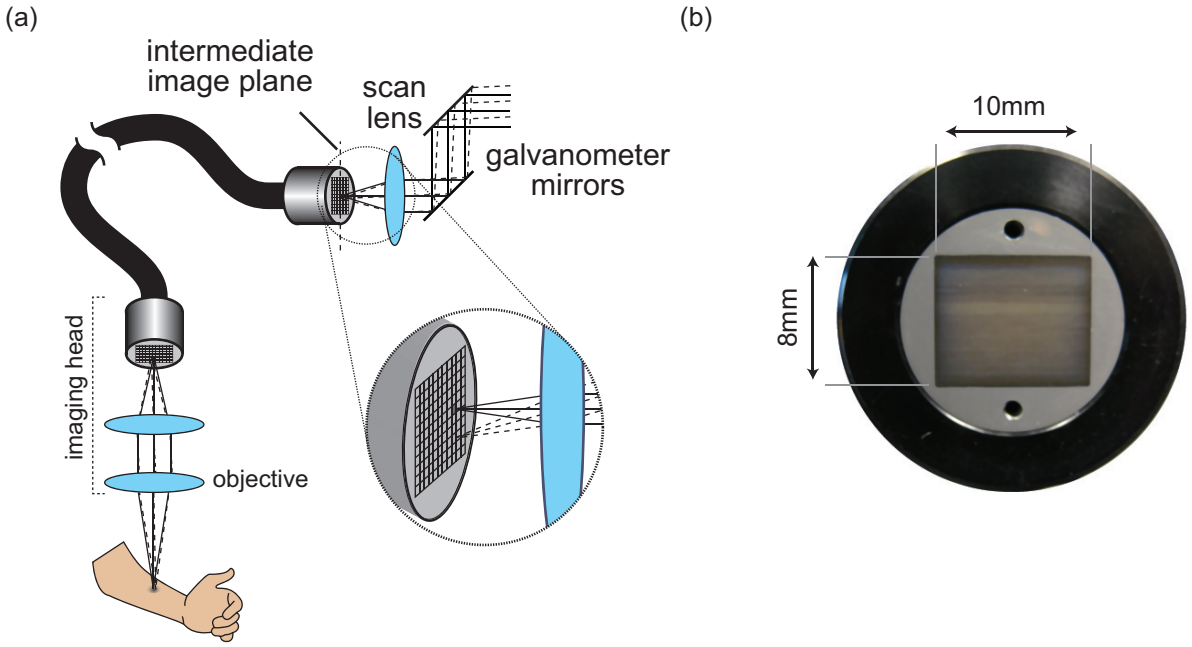

Figure 2-21 (a) Schematic diagram of fiber bundle based LOT. (b) Photograph of the fiber bundle end face. The proximal face of the fiber bundle was placed in the scan lens intermediate image plane. The moving spot on the distal face of the fiber bundle is imaged onto the sample plane. Returning light takes the opposite path.

The basic LOT setup that has been previously described relies on scattering to scramble the polarization state of the backscattered light and a polarizing beam splitting cube to direct backscattered light towards the detection arm of the system. Besides improving efficiency compared to a 50:50 beam splitter, an additional benefit of this setup is that specular reflections from the surface of the sample and from optical components within the system are reduced since specular reflections do not alter the polarization state of the incident light. Introducing a fiber bundle confounds this efficient system in two ways. Firstly, light entering each fiber of the bundle loses its polarization over the course of its journey to the distal end. If this light is then specularly reflected from the lenses in the imaging head, or from the sample, there is no way to distinguish it from scattered light once it returns through the bundle. Secondly, placement of the

fiber bundle face in the intermediate image plane introduces a large specular reflection that, in spite of the 500:1 extinction ratio of the polarizing beam splitter cube, typically saturates the detector. Other groups have addressed specular reflections at the fiber bundle face by using an index-matching oil at the fiber face [75] and tilting the fiber bundle [76]. The effect can be reduced by advancing the face of the fiber bundle just past the intermediate image plane such that the scanning beam is focused just beyond the fiber bundle face rather than at the surface. However, this reduces the coupling efficiency of the bundle as well as increasing the spot size of the scanning beam at the sample.

Another challenge associated with the fiber bundle configuration is light loss in the fiber bundle due to the packing fraction [77]. The inter-fiber space does not carry light thereby lowering the throughput of the fiber. At 532 nm we measured a light loss for one pass of the bundle of 40%, which includes losses due to both the packing fraction and reflection off the fiber bundle face.

2.4.3 Comparison study

A phantom consisting of human hair embedded in an absorbing and scattering background medium was used to compare imaging performance of our two configurations. The tissue-like phantom consisted of an agarose based hydrogel with Intralipid™ (I141, Sigma) and instant coffee (Medaglia D'Oro) added to provide reduced scattering and absorption coefficients at 532 nm of 1 mm^{-1} and 0.2 mm^{-1} respectively. The agarose solution was prepared as described in Section 2.3.1 using instant coffee as the background absorber. Once mixed, most of the liquid solution was poured into a mold to set, while the remainder was used to make a 200 μm thick sheet. When the gels hardened (~10 minutes), the phantom was assembled by placing a piece of hair on the surface of the molded gel and then covering the hair with the thin gel sheet effectively

embedding the hair at a depth of 200 μm. Figure 2-22 shows a schematic cross-section and photograph of the phantom.

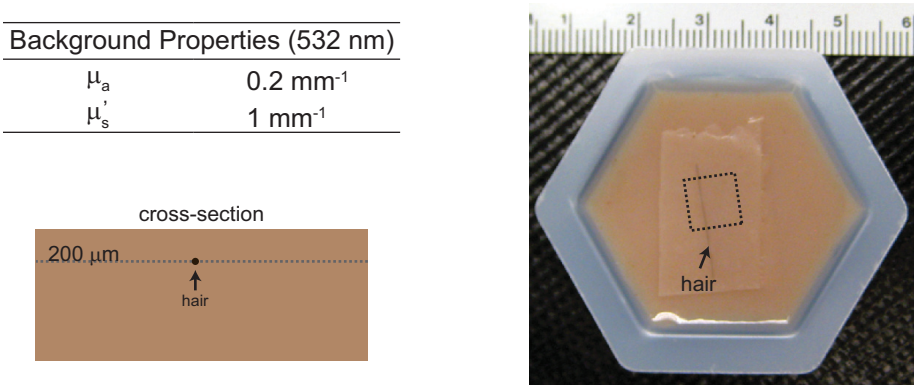

Figure 2-22 Phantom used in fiber bundles – articulating arm comparison study. Left, phantom optical properties and schematic drawing. Right, photograph of the phantom with dashed line showing scanned region of interest. Arrowheads indicate location of hair in each.

The phantom was imaged using 532 nm light with both the articulating arm and fiber bundle configurations. The incident light intensity measured at the sample plane was 1 mW which, for the fiber bundle configuration, required increasing the intensity of light entering the fiber bundle to offset transmission loses within the fiber bundle. Scanning was performed with 300 x 300 source positions (pixels) and 8 source-detector separations (300 μm offset increments). A total of 100 frames were acquired at a frame rate of 1.1 fps. In a typical LOT imaging session, fewer frames are acquired (~15-20 frames) during a scan and at higher frame rates to reduce motion artifacts. Here additional frames were acquired for statistical analysis. To reduce the possibility of motion artifacts, the articulating arm (or fiber bundle) was positioned over the phantom and immobilized for the duration of the scan. Since the intensity of light detected by the wider off-axis detector channels of our PMT is much lower than that detected by the narrow detector channels, a thin attenuating transparency film was placed in front of the first 2 channels of the PMT. This allowed for an increase in the high voltage applied to the PMT to improve the low

level light detection of the off axis channels without saturating the first few channels. The dashed lines in Figure 2-22 indicate the 10 mm x 10 mm scan region of interest. A slightly smaller region of interest was scanned with the fiber bundle because of the 8 x 10 mm area of the fiber bundle face (the imaging head was implemented with 1x magnification). 'No object scans' were acquired to allow correction for specular reflections. These scans were identical to the normal scans except that nothing was present in the sample plane.

Figure 2-23 shows LOT 'raw data' images of the hair phantom obtained using the (a) articulating arm and (b) fiber bundle after subtracting the 'no object' scans to yield $g_d S_{s,d}$ data as per Eq 2-10. In the narrowest source-detector separation (0 mm), the hair appears as a single vertical line. A shadow appears alongside the hair in the off-axis source-detector image which is characteristic of LOT data sets [78]. The offset distance of the shadow is indicative of the source-detector separation since the shadow occurs when the source is positioned adjacent to the hair, but the detector is positioned over the hair. The narrowest source-detector separation (equivalent to the on-axis detection geometry of confocal) accentuates the rough surface of the phantom.

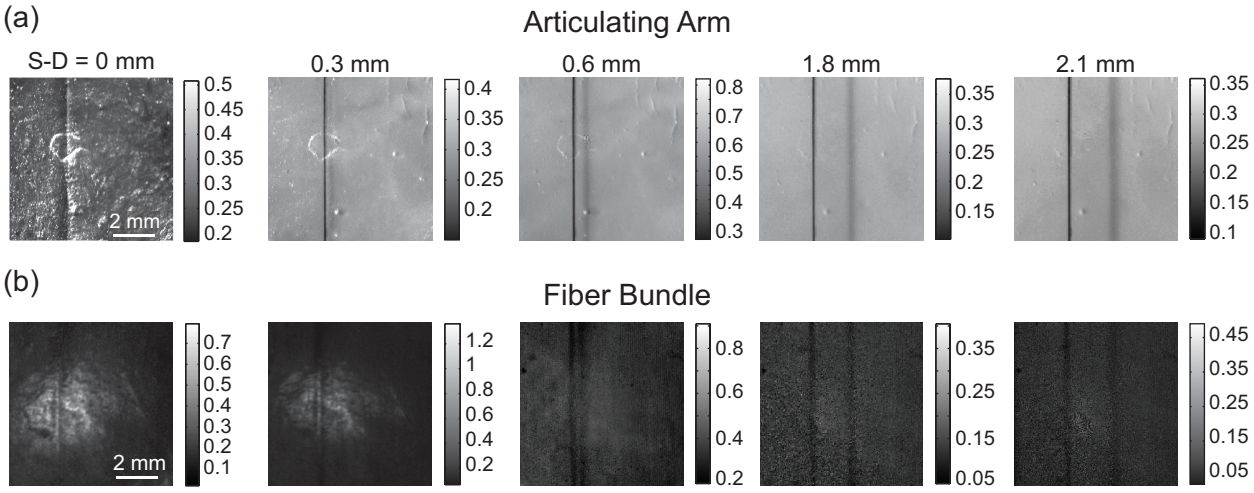

Figure 2-23 LOT 'raw' data images after dark subtraction. (a) Articulating arm. (b) Fiber bundle. Color bars are in units of volts.

In order to evaluate contrast, the background signal must first be defined. In the hair phantom, background corresponds to the homogenous regions surrounding the hair. Background signal for a single source-detector separation was calculated by first averaging the data across frames as illustrated in Figure 2-24(a). With the hair running vertically down the resulting image, the data was averaged down each column creating a profile with a constant background level and a dip occurring at the position of the hair. The average background ($S_{avgBkgd}$) was calculated from this background level and the percent change in terms of our noise model calculated by:

$$\%\Delta = \frac{\left(g_d S_{avgBkgd} - g_d S_{s,d}\right)}{g_d S_{avgBkgd}} \times 100 = \left(1 - \frac{S_{s,d}}{S_{avgBkgd}}\right) \times 100 \qquad \textbf{Eq 2-15}$$

The percent change for select source-detector separations are shown in Figure 2-24(b). There are several interesting differences between the plots that are worth noting. The two peaks, corresponding to the presence of the hair in the data, are quite different in size for the articulating arm, whereas the two peaks have similar sizes for the fiber bundle. The first peak (to the left in each plot) corresponds to the signal change when the source beam scans over the hair, whereas the second peak (to the right) corresponds to when the detector is effectively scanned over the hair. For the articulating arm, the size of the scanning source beam is diffraction-limited, leading to a high and narrow point spread function, whereas the effective detector size is approximately 300 μm wide leading to a lower and wider second peak. The fiber bundle cross-sections illustrate that the fiber bundle causes the size of the scanning beam to increase at the sample plane, leading to a lower and wider first peak. Therefore, in order to objectively compare contrast between the two configurations, we compare the amplitude of the second peak (detector shadow) rather than

the first peak. Absorption contrast, as shown in Figure 2-24(c) (left), is given by the maximum percent change in the hair shadow signal from the baseline for both configurations.

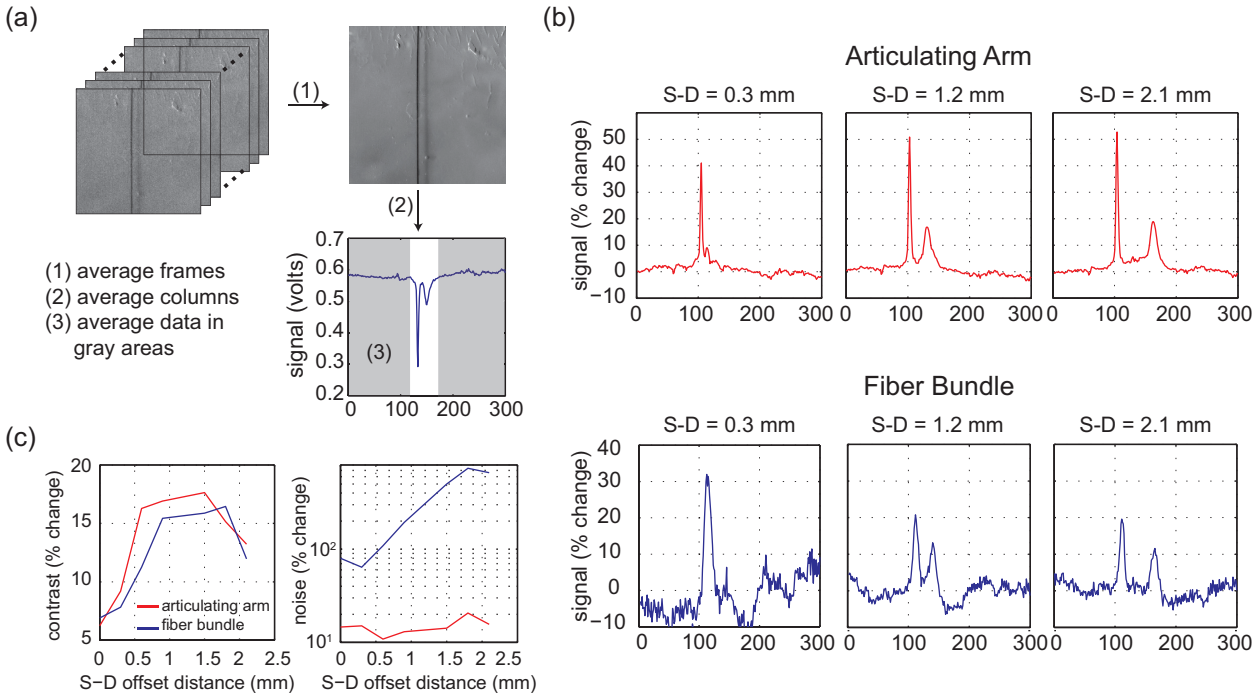

Figure 2-24 (a) Background signal was calculated from the average of 100 frames (1). The averaged frame was then averaged down columns creating a profile of the frame (2). Background regions were selected and averaged from the profile (3). (b) The percent change from the background signal provided a measure of contrast. Plots show the percent change for the articulating arm (top) and fiber bundle (bottom) at three source-detector (S-D) separation distances. (c) Contrast and noise plots for each configuration.

As expected, the contrast for both configurations is similar. The shape of the contrast as a function of source-detector separation can be explained as follows: For the narrower source-detector separation distance, contrast is lower since light detected by the narrower source-detector separations has mostly probed superficial regions above the hair. Contrast increases for the wider source-detector separations since this light has probed deep enough to interact with the hair. The slight differences between the contrast profiles for the two configurations may be attributable to the slightly different effective source-detector separations and numerical apertures

of the two measurement geometries and therefore the different relative depth sensitivities of each measurement.

Image noise was evaluated by first calculating each pixel's percent change across all 100 repeated images. The standard deviation of each pixel's percent change was then calculated and averaged for all pixels in the image resulting in a measure of noise. Figure 2-24(c) (right) compares the noise level for each source-detector distance for each configuration. Noise for both configurations increases as source-detector separation increases, as expected, due to the reduced amount of light reaching more distant detectors. These plots also clearly demonstrate that the noise level of the fiber bundle is significantly higher than for the articulating arm. This is primarily due to the significant transmission losses associated with the fiber bundle implementation; we expect that improved implementation and reduction of proximal reflections will improve the relative performance of this configuration.

The challenges associated with the fiber bundle implementation are evident in the noise plots. The higher noise levels in the fiber bundle images (compared to the articulating arm) can be attributed to the large specular reflections from the faces of the fiber bundle. The contrast values shown in Figure 2-24b are relatively unaffected by this confound, since our calibration scheme includes subtraction of a 'dark scan' corresponding to the case when no object is present. However, by comparing the amplitude of the 'dark scan' signal for the fiber bundle to measured data with an object present, we were able to deduce that 50-80% of our measured signal was due to light reflecting from the faces of the fiber bundle. Furthermore, inspection of 100 repeated scans of the fiber bundle's dark signal revealed significant, structured variance that is hypothesized to be due to small fluctuations in the relative position of each fiber with respect to

the laser beam scanning the bundle's face. This overwhelming variance is then superimposed onto the small signal that actually traversed the fiber bundle and visited the sample. Since the signal from the phantom becomes weaker as the source-detector separation distance increases, the noise from these reflections becomes more prominent in the wider source-detector separation distance images. Shot noise is an additional confound that may become problematic in this case because its magnitude increases as the square root of light intensity. Typically an increase in noise is offset by an increase in the average signal. However, in this case, the intensity of the proximal reflection signal only increases the noise level, but not the signal.

It is expected that a reduction in the reflections from the fiber bundle's ends will significantly improve the relative performance of the fiber bundle configuration. A first step would be to obtain an imaging fiber bundle whose ends have been polished to an angle other than 90^{o}, although other groups have addressed similar specular reflections at the fiber bundle face by using an index-matching oil at the fiber face [75] and tilting the fiber bundle [79]. The use of a higher extinction ratio polarizing beam splitter cube would also aid in rejecting specular reflections from the proximal face. Future endoscopic embodiments of LOT could also be implemented with distal scanning optics (e.g. using MEMs), or even high-density solid-state arrays of light sources and detectors.

2.4.4 Conclusion

The design and demonstration of LOT data acquisition through both an articulating arm and a fiber optic bundle have been presented. Of the two configurations, the images acquired through the articulating arm had a higher contrast, lower noise levels and reduced specular reflections compared to those obtained with the fiber bundle. However, the fiber bundle provided usable

data that offered significantly more flexible image acquisition and much improved potential for imaging of internal organs. While both systems described here improve tissue accessibility, as described in the next chapter, the articulating arm configuration was ultimately used for clinical imaging owing to its higher quality images.

Chapter 3

Applications of Laminar Optical Tomography

The advances made to LOT, as described in the preceding chapter, were aimed at performing *in vivo* imaging. Previous *in vivo* imaging studies performed with LOT were limited to imaging absorption or fluorescence contrast, but not both, and sequential multi-wavelength imaging, not simultaneous. The newly developed system overcomes these shortcomings and improves upon many other aspects of the system including faster acquisition rate, larger field of view, and higher measurement density. With these advances, LOT is better suited for *in vivo* imaging as it can capture faster responses, measure additional sources of contrast and have fewer motion artifacts. The remainder of this thesis focuses on *in vivo* applications using LOT. Specifically, LOT imaging of skin and LOT imaging of the rat cortex.

3.1 Clinical Skin Imaging

This section describes applications of LOT for *in vivo* imaging of skin cancer. We start with an introduction to skin cancer, including the anatomy of skin. *In vivo* imaging of benign moles and lesions are then described before detailing our investigations in clinical LOT imaging of skin cancer.

3.1.1 Introduction

Skin cancer is the most common cancer, with over 3.5 million cases diagnosed annually in the United States and incidence increasing at 3% per year. The American Cancer Society estimated that about 68,130 new melanomas, the most dangerous form of skin cancer, were diagnosed in 2010 [80]. As with other cancers, skin cancer prognosis is improved with early detection and treatment. Screening is done by a dermatologist who performs visual and palpation exams of suspicious lesions with definitive evaluation requiring surgical biopsy. Treatment typically involves removing the cancerous tissue via surgical excision. Advanced imaging techniques are continually being investigated in order to improve the diagnosis and treatment of skin cancer. In order to better understand how these imaging techniques can be of value, further discussion about the anatomy of skin and treatment of skin cancer is warranted.

3.1.1.1 Anatomy of skin

Skin is made up of three layers: the epidermis, dermis, and subcutaneous tissue (see Figure 3-1). The epidermis is the thin outer layer of skin and is further composed of three sublayers: stratum corneum, keratinocytes, and the basal layer. The outermost epidermal layer, stratum corneum, contains continually shedding, dead keratinocytes. The keratinocytes (squamous cells) layer contains living keratinocytes and the basal layer, the inner most layer of the epidermis, contains basal cells. Basal cells continually divide, forming new keratinocytes thereby replacing old ones that are shed from the skin's surface. The epidermis also contains melanin producing cells called melanocytes. Melanocytes synthesize melanin in vesicles called melanosomes, which can remain in the melanocyte or be delivered to keratinocytes though cytoplasmic processes [81, 82].

Melanin is the primary pigment in skin and is also one of the main sources of absorption contrast for optical imaging.

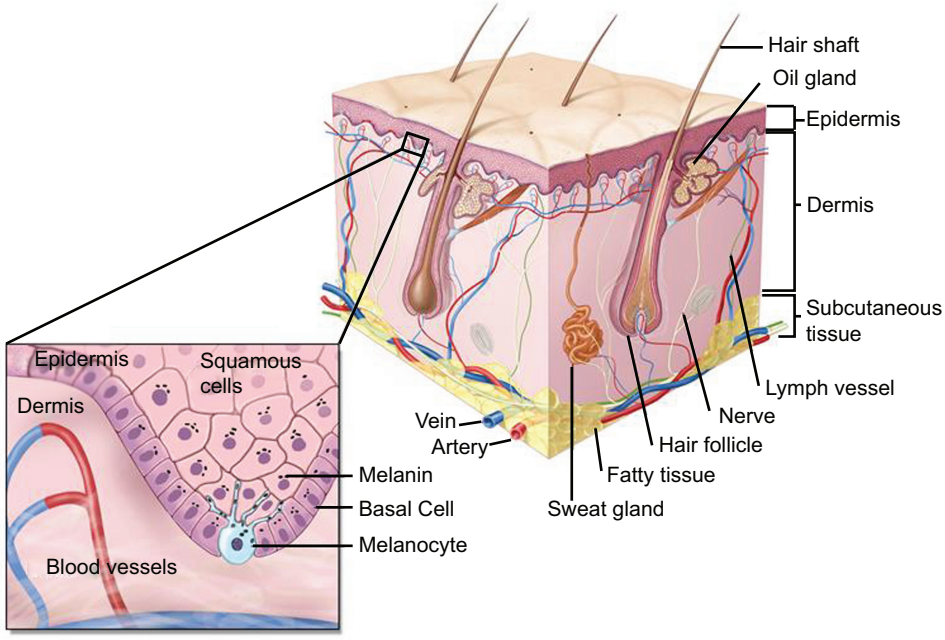

Figure 3-1 Anatomy of skin. Epidermis, dermis and subcutaneous tissue make up the 3 layers of skin. Inset shows dermal-epidermal junction with blood vessels confined to the dermis and squamous cells, basal cells and melanocytes in the epidermis. (adapted from [83])

Beneath the epidermis lies the dermis, the second layer of skin. The dermis is a layer of connective tissue that anchors the epidermis and binds it to the underlying subcutaneous tissue. The dermal layer is usually much thicker than the epidermis ranging from a tenth of a millimeter to a few millimeters [84]. Blood vessels, lymph vessels, hair follicles, and sweat glands can all be found in the dermis as well as nerves that act as pain and touch receptors. The boundary between the dermis and epidermis is referred to as the dermal-epidermal junction and is clinically meaningful because cancers, such as melanoma and basal cell carcinoma, both originate and later spread from this junction. Because of this, optical techniques often aim to image this region.

Subcutaneous tissue, the deepest layer of skin, consists of a network of collagen and fat cells. This layer functions mainly as insulation, cushion for deeper tissues against injury, as well as fat storage.

3.1.1.2 Skin cancer

Cancer is a disease that can generally be characterized by uncontrolled growth and spread of abnormal cells. Typically, damage to genes that either control cell division or prevent inappropriate cell progression to mitosis lead to the possibility of developing cancer [85]. As a person ages, such mutations become more likely and the body becomes less efficient at stopping pre-cancer cells, accounting for the observation that skin cancers typically strike the older segment of the population [86] (Figure 3-2). Exposure to ultraviolet radiation is the main cause of skin cancer with exposure accumulated throughout life [87].

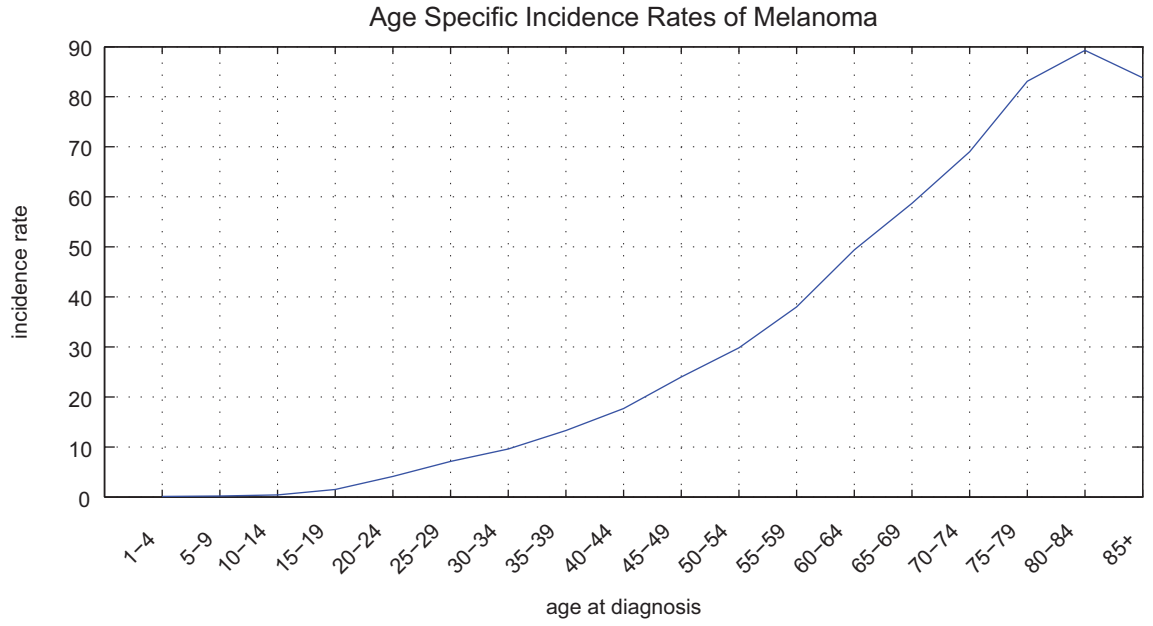

Figure 3-2 Plot of melanoma incidence rates (per 100,000) as a function of age. Data from [80].

The three most common types of skin cancer are basal cell carcinoma (BCC), squamous cell carcinoma (SCC) and melanoma [80]. BCC and SCC are non-melanoma skin cancers that develop in basal cell and keratinocytes respectively. BCC, the most common skin cancer, often first appears as a small red or pink lump on previously normal skin. If left untreated, BCC may crust over and bleed while it continues to slowly grow locally. BCC does not typically metastasize. The second most common skin cancer is SCC. SCC grows more quickly than BCC forming a lump which may crust, bleed, or ulcerate. SCC may occasionally metastasize, however this is unlikely. Melanoma develops in melanocytes and typically evolves through a slow growing radial growth phase within the epidermis followed by a vertical growth phase into the dermis where it has the capacity for developing metastasis [84]. The presence of blood vessels and lymphatic vessels in the dermis increase the likelihood of the tumor spreading which is why melanoma is considered the most serious form of skin cancer.

The biological changes induced by skin cancer can cause changes in the optical properties of the affected skin. The increase in melanin associated with uncontrolled melanocyte replication in some melanomas produces a pigmented lesion that can be used for establishing excision margins. While detecting melanin that is not discernable by eye may be helpful in establishing excision margins, it does not necessarily indicate the true margins since not all cancerous melanocytes create excess melanin and the melanin molecules themselves are not cancerous. Angiogenesis associated with dermal invasion in advanced melanoma creates local increases in blood that could be measured with optical techniques that are sensitive to absorption contrast and can image to depths beyond the dermal-epidermal junction.

The preferred method of treatment for skin cancer is surgical excision. Surgery is often more involved than simple removal of the visible lesion as cancer boundaries may extend beyond that visible with the naked eye. Skin cancers on the face further complicate surgery as preservation of facial features and function require careful consideration. During some surgical techniques, the cancer is removed and examined microscopically by a pathologist before closing the wound. Preparation and subsequent examination of the excised tissue followed by additional excisions (if necessary) can be time consuming leading to increased patient discomfort and cost [88].

Two important measures, particularly in melanoma, are tumor thickness and depth of invasion [89, 90]. Tumor depth is most accurately measured by evaluating the entire tumor following excision. Since biopsy does not sample the entire tumor, it is less accurate for measuring tumor depth. In addition to being an important prognostic factor, tumor thickness and invasion play an important role in determining the surgical excision margins. Melanomas confined to the epidermis (in-situ melanoma) require a 0.5 cm safety margin whereas invasive melanomas (those that penetrate into the dermis) require a 1-2 cm boundary [91]. The thickness of the tumor is also important as melanomas with thickness less than 2 mm require a 1 cm safety margin with the margin increasing to 2 cm for thicker lesions [92].

3.1.1.3 Screening tools

The need for sensitive screening, early detection, and accurate margins while reducing the number of biopsies is critical for improved patient care and has, in part, led to the use of a variety of non-invasive imaging techniques that can be used to complement naked-eye examinations including dermoscopy [93-95], CSLM [94, 96], OCT [97, 98], high-frequency ultrasound [99, 100] and digital image analysis [101, 102]. In a recent study [94], Wood's lamp, dermoscopy and

CLSM were evaluated for presurgical margin mapping of lentigo maligna melanoma. Wood's lamp examination consists of visualizing the lesion under UV light and assists in boundary mapping by emphasizing hyperpigmentation through UV fluorescence. Hyperpigmented areas, such as the lesion, will absorb UV light without fluorescence thereby accentuating the lesion boundaries. Dermoscopy is a technique that minimizes light scattering from the surface of skin, allowing visualization of subsurface structures up to the papillary dermis (outermost layer of the dermis). While these techniques provide a relatively fast method for delineating approximate lesion borders, they are not sufficient to reliably provide true clinical margins [94]. Reflectance CLSM permits visualization of cellular structures up to the papillary dermis with resolution comparable to that of routine histology. The CLSM images differ from those of stained histology owing to different sources of contrast (reflectance for CLSM and absorption for bright field histology). Although useful, CLSM suffers from limited penetration depth and the inability to exploit absorption contrast from hemoglobin and melanin. These chromophores are significant to melanoma as pigmented melanomas have increased levels melanin [103] and increased vasculature beneath the tumor is associated with dermal invasion [104, 105]. Neither Wood's lamp, dermoscopy, nor CLSM are sensitive to vascular changes beneath the lesion.

LOT imaging of skin cancer could provide valuable information for skin cancer screening and treatment planning. The ability of LOT to probe beyond the dermal-epidermal junction could reveal changes in vasculature beneath lesions which could help determine if dermal invasion has occurred or assist in the excision margin determination. The depth sensitive measurements could help determine the lesion depth, an important prognostic factor and parameter for surgical planning. Further, LOT measurements might also be of use for selecting a region to biopsy within larger lesions. The results presented in [59] demonstrated that LOT can provide depth

sensitive measures from a skin-mimicking phantom. In order to evaluate LOT's *in vivo* skin imaging capabilities, imaging of benign lesions and cancerous lesions was performed as described next.

3.1.2 Preliminary Skin Imaging

In vivo imaging of benign lesions was performed using the multi-wavelength system implemented on a mobile cart. A cart implantation was desirable in anticipation of performing clinical measurements. Two different lesion types were imaged owing to the different sources of contrast present in each. A benign mole located on the arm of a volunteer having contrast primarily due to melanin was imaged. Moles are formed by melanocytes that are clustered rather than spread throughout the skin. The melanin produced by these melanocytes gives a mole its black or brown pigmentation. The second benign lesion imaged was a permanent erythema on the finger of a volunteer. An erythema is redness of the skin that is caused by local buildup of red blood cells due to congestion of blood capillaries. Imaging these two lesions types is relevant to imaging skin cancer as measures of melanin and hemoglobin have clinical value. For both lesions, 15 frames of multi-wavelength data was acquired at 10 frames/second and with 100 x 100 pixel images.

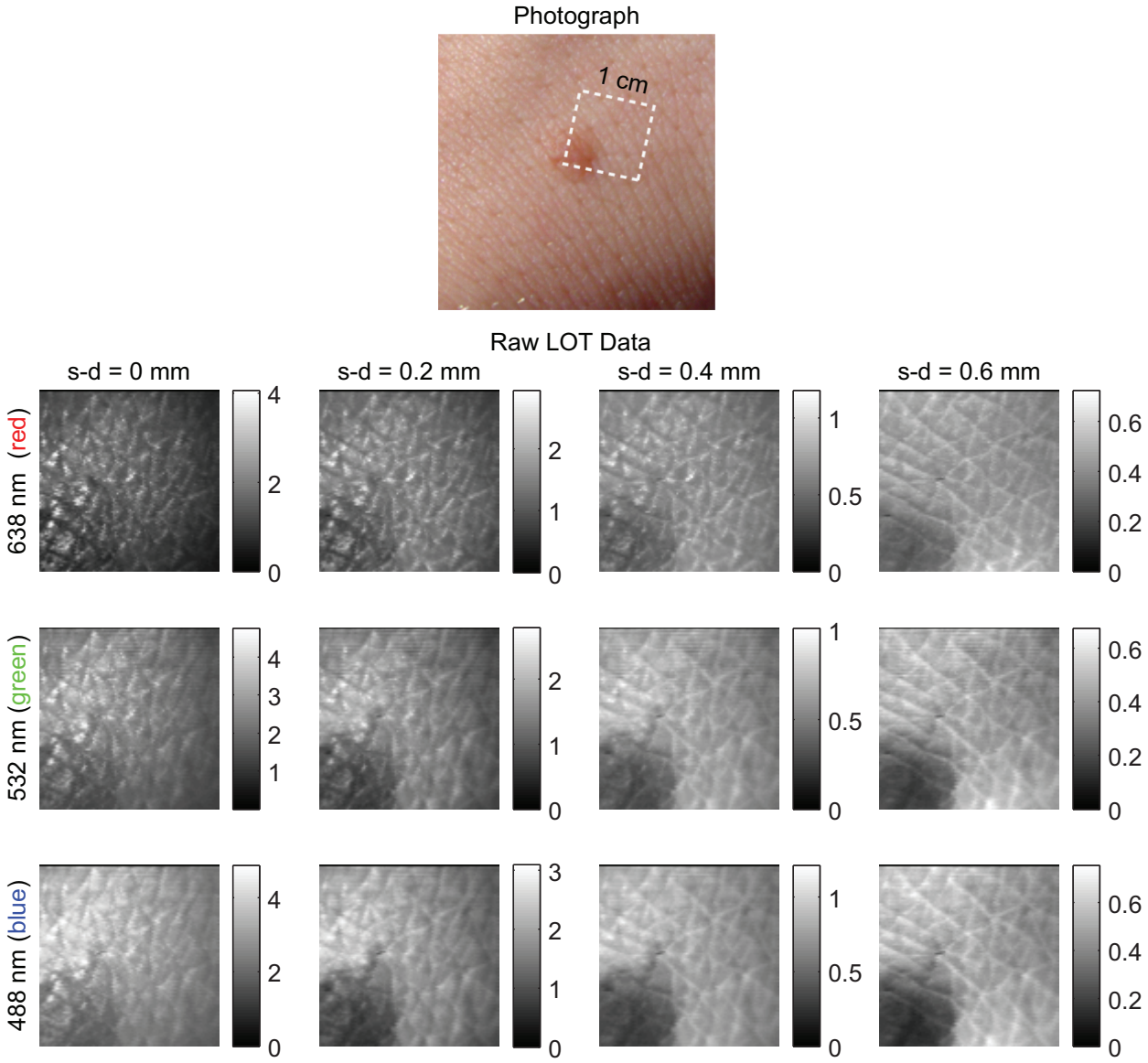

Figure 3-3 Top, photograph of benign mole lesion located on the arm. White box indicates the 1 cm LOT scan region of interest. Gray scale images show 'raw' LOT data for different source-detector separation distances.

Figure 3-3, top, shows a photograph of the mole with the 1 cm x 1 cm LOT scan region of interest indicated by the white box while the bottom of the figure shows 15 frame average of 'raw' LOT data for the first 4 source-detector separation offset distances. The images for on-axis detected light (s-d = 0) show the fine texture on the surface of the skin. The on-axis light collected is similar to that of confocal microscopy, however since a slit, rather than a pinhole, is

positioned in front of the detector, more out of focus light can reach the detector for LOT. As a result, the on-axis image generated by LOT will have poorer resolution than that of a confocal microscope. However, the true value of LOT imaging lies in its ability to provide depth sensitive measurements of tissue. As the source-detector separation increases, so too does the depth sensitivity of the detector measurement. This is evident in Figure 3-3 as surface features that are prominent in the narrow source-detector separation images become less apparent in the wider offset detector images and specular reflections are no longer visible.

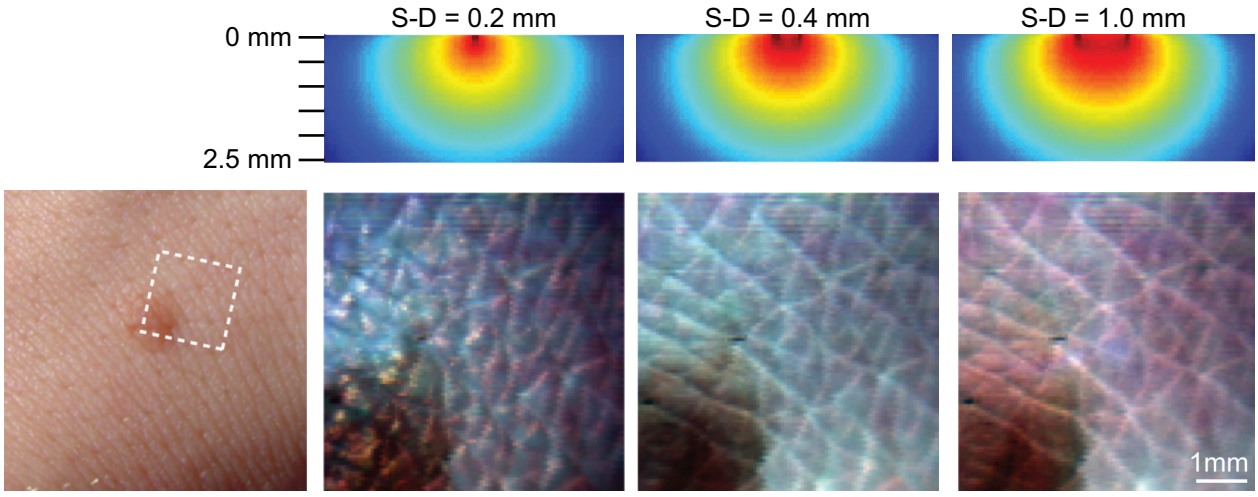

Figure 3-4 LOT imaging of a benign mole. Photograph on left show the LOT scan region of interest. LOT 'raw' data images for 0.2 mm, 0.4 mm and 1.0 mm source-detector separation images are shown on the right. The sensitivity function for each detector is shown above its corresponding image.

The absorption spectrum for melanin (Figure 1-1b) shows that melanin absorption decreases as wavelength increases in the visible spectrum which is supported by comparing the contrast of the mole in the red LOT images to that of the green and blue images. Higher absorption by melanin in the mole in the blue and green data sets results in greater attenuation and less light being detected. An alternative way to visualize the multi-wavelength data set is to merge data into the RGB colorspace to create photograph-like images. While these images can help accentuate

subsurface features of the lesion, as described in Section 1.3.1 ‘raw’ LOT data cannot be interpreted as a true depth section through the tissue. An RGB merge of data shown in Figure 3-4 clearly shows features that may not be appreciated by viewing the grayscale images alone. The deeper sensitivity depth of the 1.0 mm source-detector separation is apparent indicated by the sensitivity map above the image. As the measurement sensitivity depth probes into the dermis, light absorption from hemoglobin will begin to contribute to the measurements as blood vessels and capillaries are found in the dermis. This becomes evident in the RGB merge data of the 1.0 mm source-detector separation as the tissue surrounding the mole becomes redder in appearance.

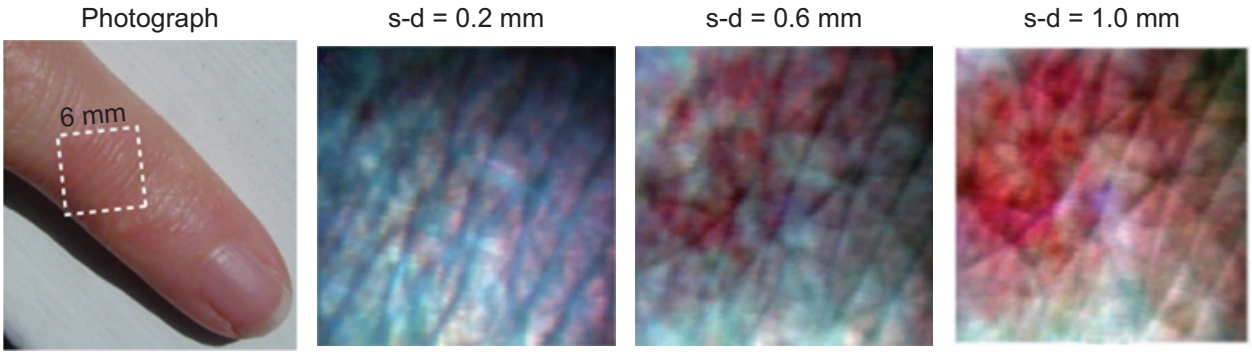

Figure 3-5 LOT imaging of erythema. Dashed box in the photograph to the left shows the scan region of interest. Surface features dominate the ‘raw’ data image for the narrow, 0.2 mm, offset distance detector while subsurface hemoglobin is emphasized in the 1.0 mm ‘raw’ RGB merged data.

An RGB merge of the LOT imaging results for the erythema are shown in Figure 3-5. As with the benign mole images, the narrow source-detector separations show sensitivity to more superficial regions. Observation of this image alone does not provide strong evidence of the presence of an erythema. The two wider source-detector separations show increased levels of green and blue absorption as evident by their red appearance. The deeper sensitivity depth of these detectors is apparent as hemoglobin contrast provided by the erythema becomes more prevalent.

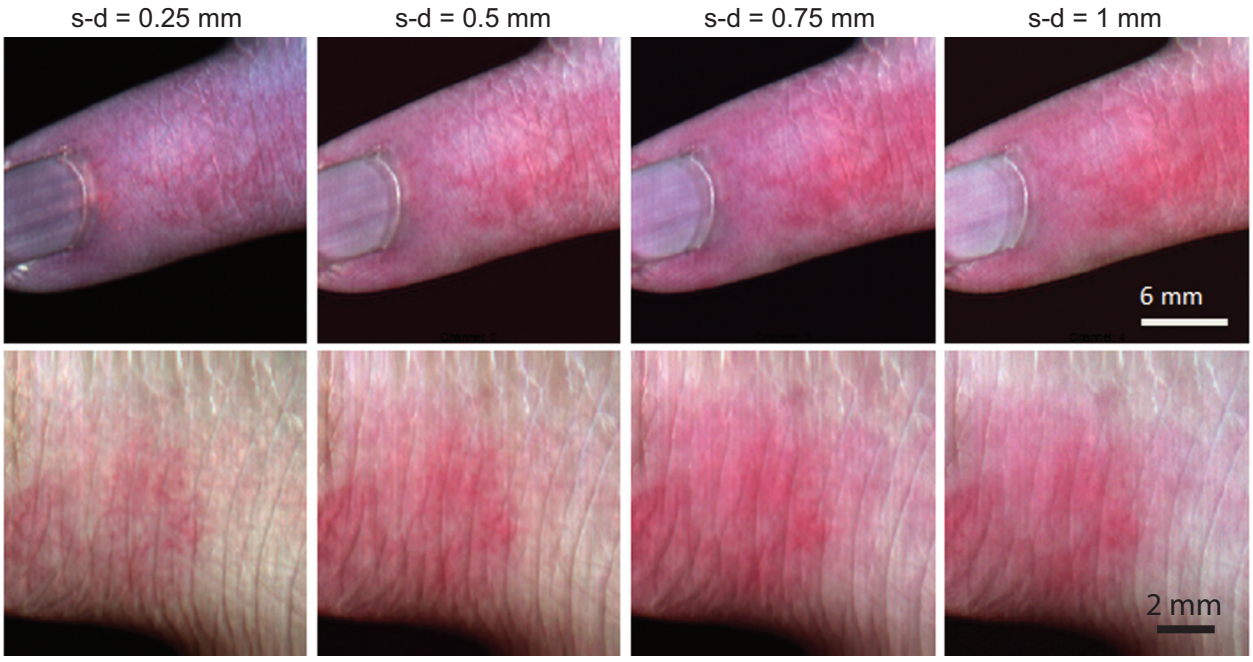

Figure 3-6 LOT imaging of an erythema scanning a large field of view (top) and smaller field of view (bottom).

Figure 3-6 demonstrates a key feature of the second generation LOT system. The top and bottom rows show RGB merged data of the erythema using 20 mm and 10 mm field of views. These large field of views (compared to that of the first generation system) were easily achieved by adjusting the amplitude of the control voltage sent to the galvanometer mirrors through the LOT control software without the need to make any mechanical changes to the system. A second feature worth noting about the data collected from benign lesions is that all images shown here are averages of 15 frames captured at 10 frames/second. Each multi-wavelength data set was captured in approximately 1.5 seconds. While the volunteers were instructed to remain still during imaging, no additional precautions were taken to prevent motion artifacts and the data sets did not require co-registration before averaging.

3.1.3 Clinical imaging

3.1.3.1 Imaging system

Prior to collecting clinical measurements, the system was modified to include an interface with which to image lesions on a range of locations on the body. A fiber optic image bundle was initially developed, providing a flexible patient interface. Due to the poor image quality obtained through the fiber bundle, a second patient interface was developed that utilized a more rigid articulating arm configuration. Section 2.4 describes the development of these implementations.

With both clinical interfaces, absorption contrast measurements were simultaneously taken at 488 nm, 532 nm and 638 nm with 7 source-detector separation distances ranging from 0 to 1.75 mm. Data from the 1.0 mm offset detector was not collected due to a fault in the electronic detection circuitry. Imaging was performed at 3 frames per second, collecting 220 x 270 pixel images with the fiber bundle configuration and 300 x 300 pixel images with the articulating arm setup. The difference in image pixel dimensions can be attributed to the rectangular face of the fiber bundle. The fields of view of the two implementations were similarly different with the fiber bundle having a 12 x 15 mm field of view and the articulating arm having a 1 cm x 1 cm field of view. During each scan, a total of 15 frames were acquired and subsequently averaged.

Calibration scans consisting of a ‘no laser’, ‘no sample’, and ‘light’ scan were collected for each patient immediately prior to the imaging session and used to calibrate the data sets as described in Section 2.2.2. Placement of an attenuating transparency sheet in front of the first 2 source-detector separation channels was found to be useful during development of the clinical interfaces. The gain of the PMT is set by a single high voltage applied to the PMT cathode. Since

the intensity of light detected by the narrower source-detector separation channels is greater than that of the wider channels, the narrow channels were found to saturate if the gain was increased to improve detection of the low light levels of the wider channels. By attenuating only the light reaching the narrow offset channels, the high voltage (gain) could be increased without saturating the narrow offset channels. The calibration scans collected for each patient corrected for this as the 'white' scan measured the light with equal intensity across all source-detector separation channels.

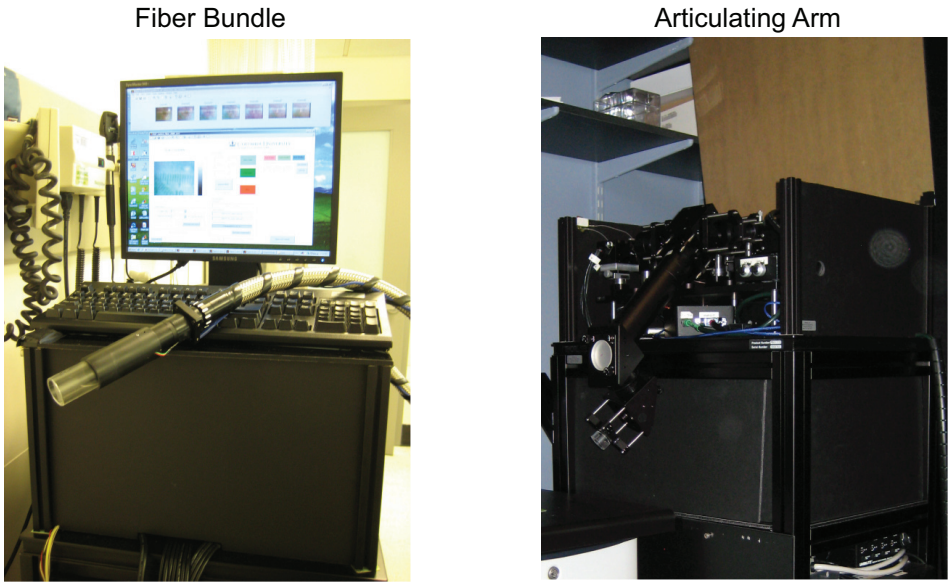

Figure 3-7 Photograph of the fiber bundle (left) and articulating arm (right) interfaces. The lid and front cover for the articulating arm configuration are removed to show the optical components of the system.

3.1.3.2 Clinical protocol

This study was performed in collaboration with Dr. Désirée Ratner, Dermatological Surgeon at the Columbia-Presbyterian Medical Center. All procedures involving human subjects were approved by the Columbia University Institutional Review Board. A total of 10 patients were recruited who were undergoing surgical removal of either BCC, SCC, or melanoma. On the day

of the surgery, the lesions were first photographed and then imaged with LOT. An adjacent region of "normal" tissue was also imaged to serve as a control. After imaging with LOT, the surgeon marked the excision boundaries around the lesion and a second photograph was taken. The lesion was then excised and sent to dermatopatholgy where it was fixed in formalin, embedded in paraffin, bread loaf sectioned, and stained with hematoxylin and eosin (HE). In addition to providing stained tissue sections, dermatopathology provided a map indicating the orientation of each slide in the tissue sample. In order to compare the LOT images with histological findings, the slides were digitized using bright field microscopy under 10x magnification. Figure 3-8 shows a flow chart of the clinical data collection protocol.

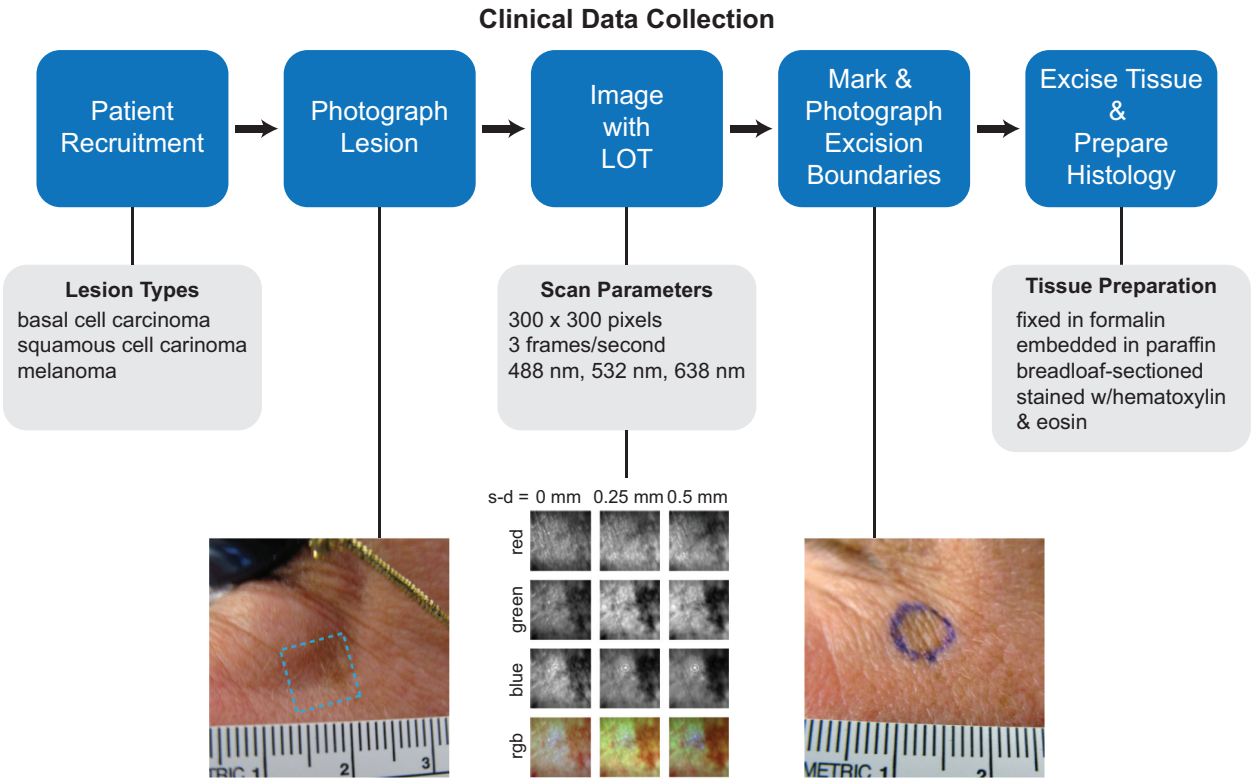

Figure 3-8 Flow chart of clinical data collection. Patients with BCC, SCC, or melanoma are eligible for inclusion in the study. On the day of surgery, lesions are photographed and scanned with LOT. The surgeon then marks the excision boundaries and the lesion is photographed again before being excised. Tissue samples are fixed in formalin, embedded in paraffin, breadloaf-sectioned and stained with hemotoxylin and eosin.

3.1.3.3 Results

Table 3-1 provides a description of the patients participating in the study. The location of the lesions was consistent with the observation that sun exposed regions such as the arms, face, and neck are more prone to develop skin cancer [80]. While recruitment did not target a specific race or sex, the majority of patients imaged were white males with an age over 50.

Table 3-1. Overview of Subjects

Subject #	Lesion Type	Lesion Location	Age	Sex
1	Lentigo maligna	face	80	M
2	Melanoma in situ	face	82	M
3	Lentigo maligna	face	57	M
4	Melanocytic nevus	scalp	31	M
5	Angioma	back	73	M
6	BCC	arm	54	F
	BCC	chest		
7	Lentigo maligna	face	42	M
8	BCC	back	71	M
9	Melanoma	arm	73	M
10	Seborrheic keratosis	face	48	F
11	SCC	face	54	M

Photographs of the lesions are shown in Figure 3-9. Lesion sizes ranged from approximately 1 cm to greater than 3 cm meaning that in some cases, multiple LOT scans were acquired to capture the entire lesion. While it was previously shown that the system could capture large field of view images, the clinical interfaces limited field of view.

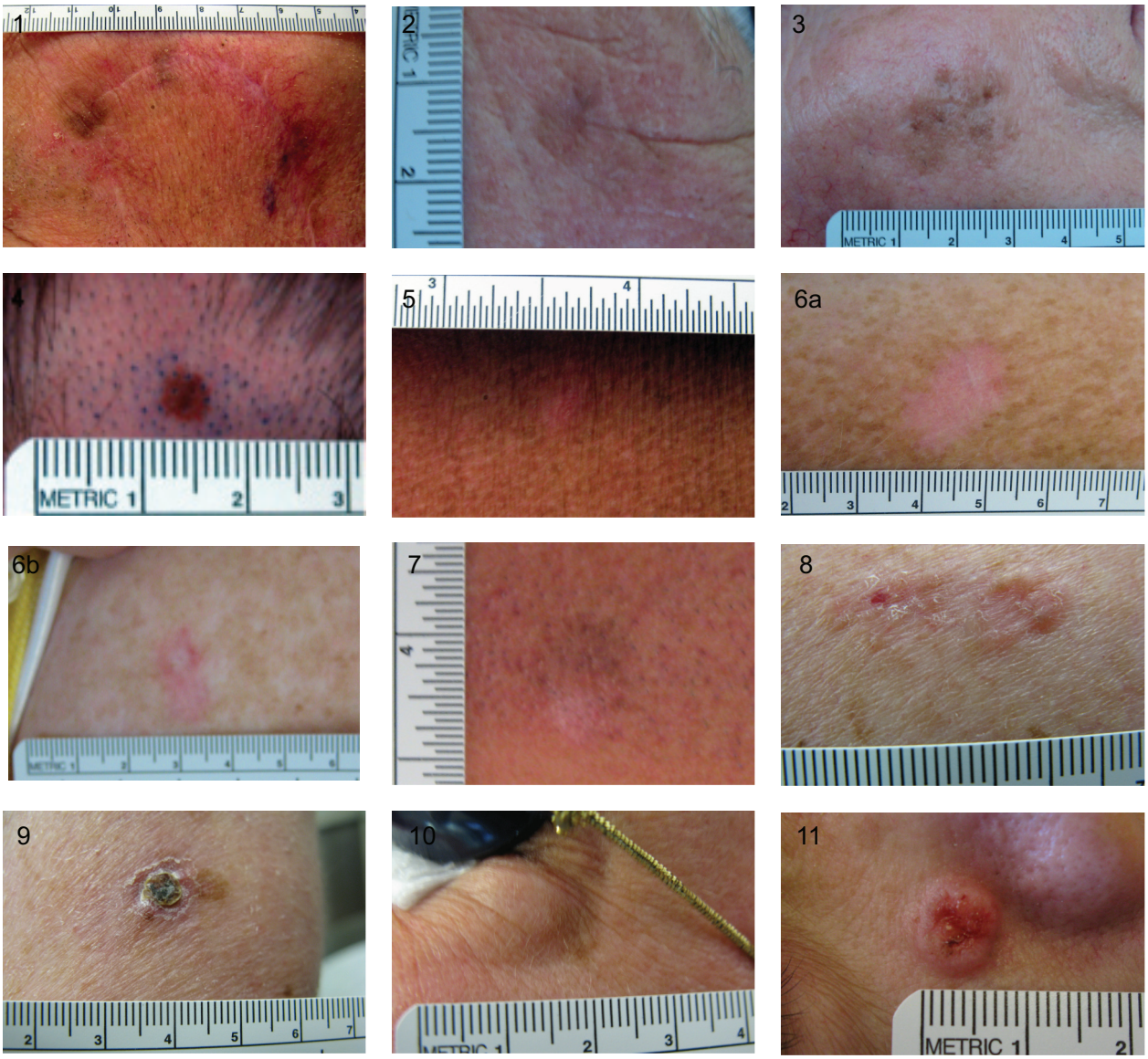

Figure 3-9 Photographs of lesions taken prior to LOT imaging. Image numbers correspond to subject numbers listed in Table 3-1.

3.1.3.4 Fiber Bundle Data

Data for the first patient is shown in Figure 3-10. The white box in the top left photo shows the scanned region of interest. Images in the bottom row are an RGB merge of data from 4 source-detector offset distances. After imaging with LOT, the excision boundaries were drawn and photographed as shown in the top right photo. This patient was undergoing resection of a

recurrent lentigo maligna melanoma. Presence of the lesion along scar tissue suggests that previous margins had not been fully removed.

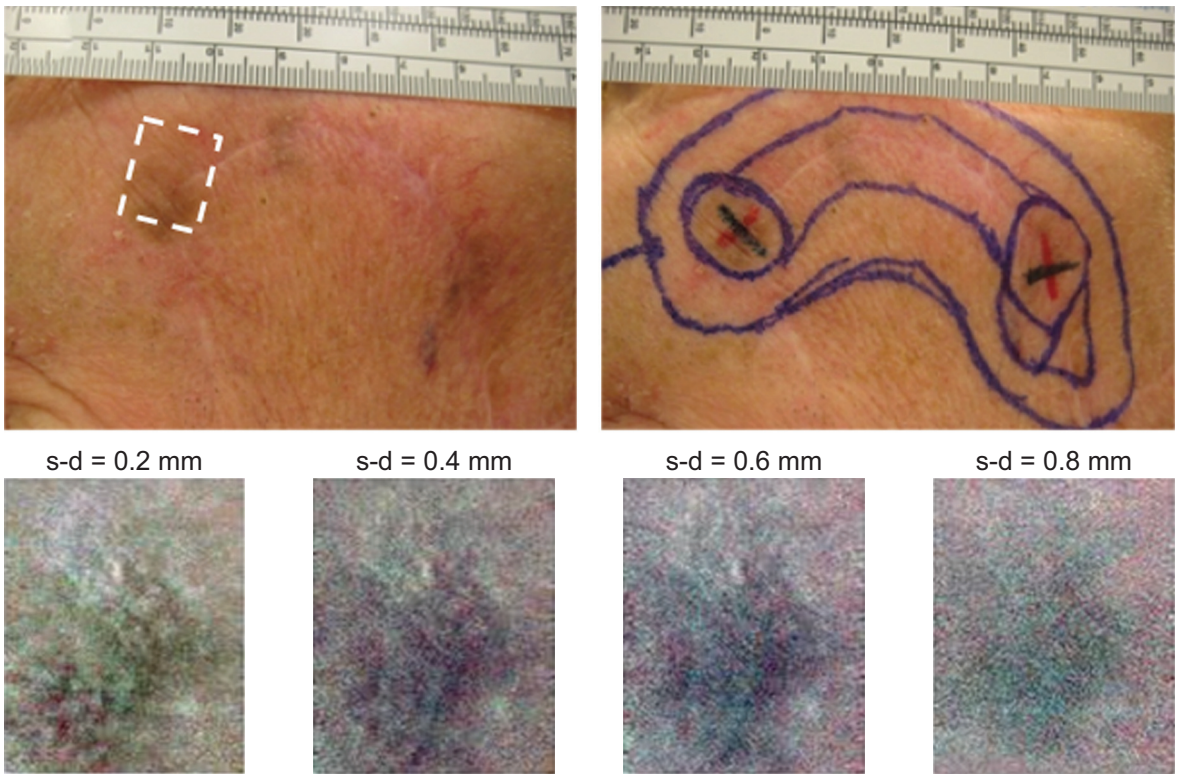

Figure 3-10 LOT data collected on a lentigo maligna melanoma lesion using the fiber bundle interface. Top left, photograph of the lesion with the white box indicating the LOT scan field of view. Bottom, RGB merge of LOT. Top right, photograph taken indicating surgical excision boundaries.

Compared to data acquired from benign lesions, the images collected with the fiber bundle configuration had lower resolution and more noise. As described in Section 0, the fiber bundle configuration suffered from a large specular reflection from the face of the fiber bundle. With no attempt to reduce this reflection, the acquired data consisted only of saturated pixels. The adjustment made to reduce the fiber bundle reflection, while allowing acquisition of LOT data, resulted in poorer image quality. By placing the fiber bundle slightly out of the scan lens focus, the diameter of the reflection became larger allowing more of it be rejected by the slit in the

detection arm. While this helped to reduce the intensity of the reflection, it also lowered the coupling efficiency and increased the spot size of the scanning source. The result was that while the detectors were no longer saturated by the fiber bundle reflection, the intensity of the light returning from the tissue was relatively low compared to the setup used for free space arrangement used to image benign lesions and the image quality therefore suffered.

In an effort to improve the quality of the collected data, a second clinical interface was developed and used to image the remaining patients. Data collected with this interface is presented next.

3.1.3.5 Articulating arm data

All but the first patient in Table 3-1 were imaged using the articulating arm interface. Example RGB merged data collected from patient 4 with the articulating arm setup is shown in Figure 3-11. The Melanocytic nevus lesion was located on the scalp which had been shaved as part of the surgical procedure. The black spots located throughout the images are representative of absorption from the shaved hair. Looking at the 0.5 mm and 0.75 mm source-detector separation images clearly shows the pigmented lesion. While the lesion is visible in the narrower, 0.25 mm offset distance image, surface features are more prominent owing to the shallower sensitivity depth of the detector. The reflections present in the wider detector offset distance images indicate problem with calibration of the data, specifically subtraction of the ‘no object’ (reflection) scan.

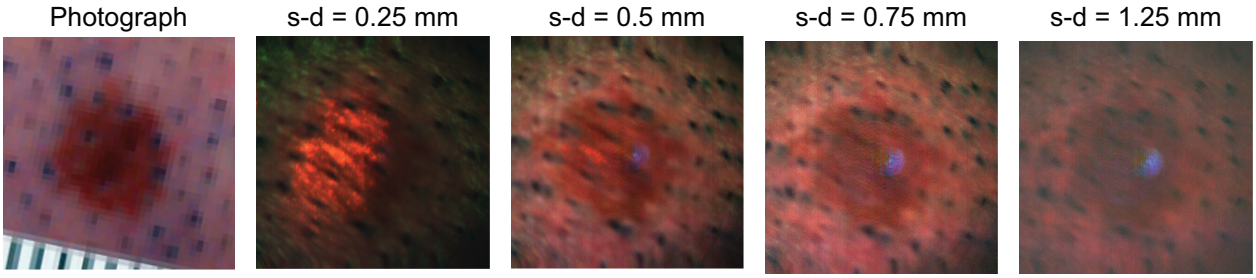

Figure 3-11 RGB merge of LOT data from a melanocytic nevus lesion. Black spot throughout the image are shaved hair as the lesion was located on the scalp. Left most image is a photograph of the scanned region of interest. Blue artifact seen near center the 0.5 mm through 1.25 mm source-detector seaparation images is a specular reflection that could not be eliminated from the data.

The top section of Figure 3-12 shows the uncalibrated data set for all three wavelengths and each source-detector separation distance. A prominent feature in the wider source-detector separation images for the green and blue images is the reflection in the center of the image. In fact, when the image is scaled according to its minimum and maximum values, features of the skin lesion become difficult to see. As described in Section 2.2.2, acquisition of a 'no object' scan and subsequently subtracting it from the skin data should remove the contribution of the reflection from the data. The middle section of Figure 3-12 shows the 'no object' scan acquired during the same imaging session at the clinic and the bottom section of shows the results of subtracting the 'no object' scan from the skin data.

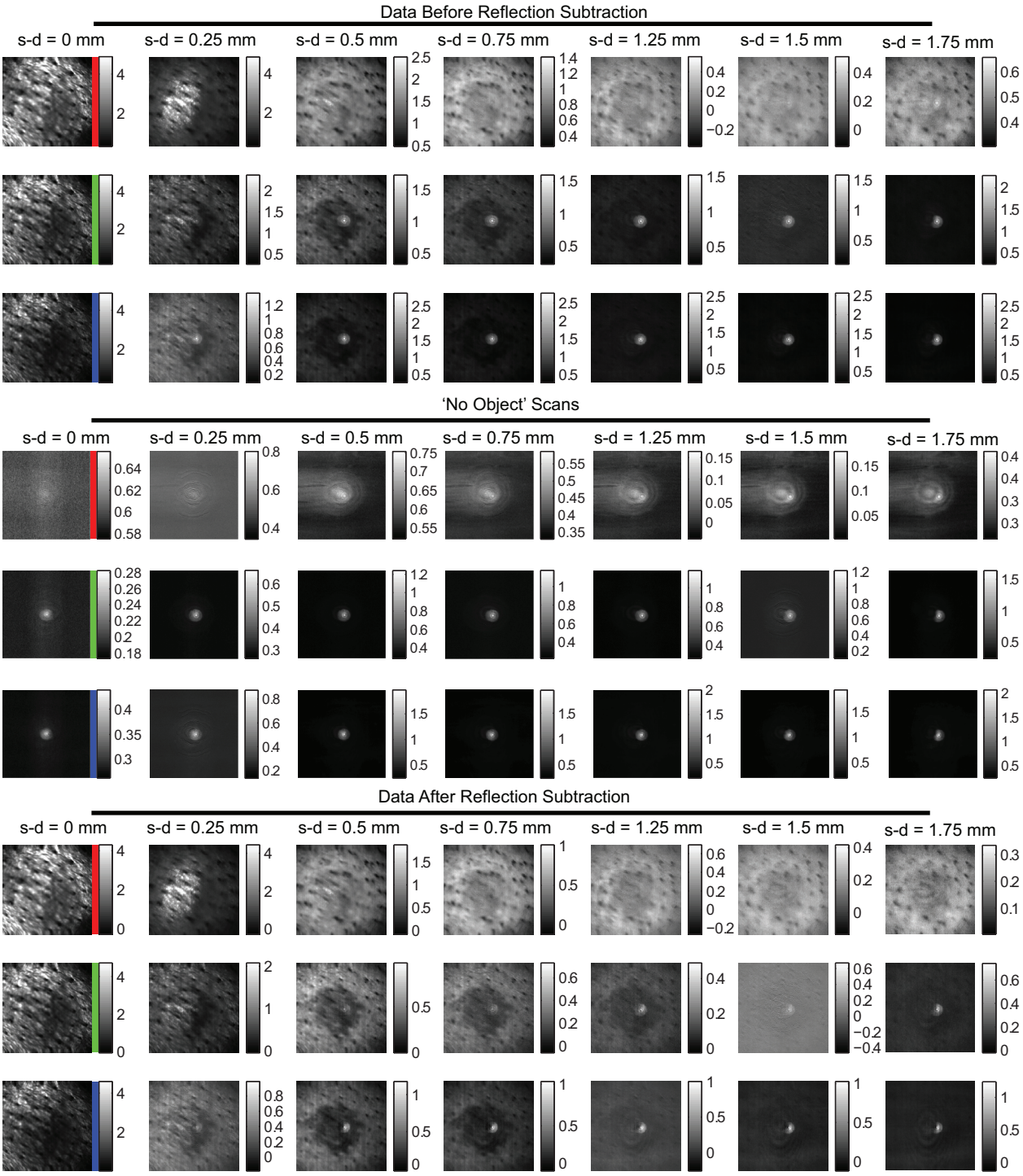

Figure 3-12 Example multi-wavelength data for a melanocytic nevus before (top) and after (bottom) subtracting the 'no object' (reflection) scan.

An explanation as to why subtraction of the 'no object' scan did not adequately remove the reflection from the skin data refers back to Section 2.1.1.3 and the discussion about polarized

light. Linearly polarized light incident upon a metal or dielectric mirror will reflect and maintain its linear polarization state so long as the beam is incident normally on the mirrors or if the plane of polarization lies in or normal to the plane of incidence. If the polarization direction makes an angle with the plane of incidence, the reflection will introduce a small phase shift between the parallel and perpendicular components of the electromagnetic field. As a result, the reflected light will no longer be linearly polarized, instead, it will be slightly elliptically polarized. In LOT, the galvanometer mirrors are metallic mirrors with a dielectric coating. Reflection off the galvanometer mirrors will therefore result in slightly elliptically polarized light. A portion of the specular reflections from components distal to the galvanometer will therefore not be rejected by the polarizing beam splitter in the absorption detection arm which, in part, is the reason why reflections appear in the LOT images. The efficiency with which the polarizing beam splitter separates cross polarized light also plays a role. In a rigid bench top configuration, subtraction of a 'no object' scan is typically sufficient to remove the reflection from the data set. However, the articulating arm implementation makes removing the reflection from the data more difficult for two reasons: (1) the articulating arm includes two additional metallic, dielectric coated mirrors that each contribute to the elliptical polarization of the incident light and (2) a change in position of the articulating arm changes the angle between the polarization of the incident beam and the mirrors within the arm and therefore the amount of elliptical polarization introduced by the reflection. Therefore, the intensity of the reflection during the patient scan will not be the same as that for the 'no object' scan unless the articulating arm is in the same position for both scans.

The inability to remove the reflections from the skin data made quantitative analysis of the data difficult as the inability to differentiate between the reflection and signal from the tissue is

crucial, especially in the wider detector offset distance where the intensity of the returning signal is lowest.

3.1.3.6 Clinical case study

Subject 11, a 54 year old Asian male, participated in the study presenting with a non-pigmented squamous cell carcinoma on the face. Figure 3-13a shows a photograph of the lesion. The proximity of the lesion to the eye and nose made preservation of facial tissue an important consideration. As such, the initial excision boundaries were conservative Figure 3-13c.

The lesion was imaged using LOT as described above, collecting multi-wavelength data at 7 source-detector separation offset distances. An average of the 15 frames acquired during the scan is shown in Figure 3-13d. Visual inspection of the RGB merged data shows that subsurface features surrounding the lesion are clearly accentuated in the wider detector offset images. The scanned region is indicated by the overlaid LOT data in Figure 3-13b.

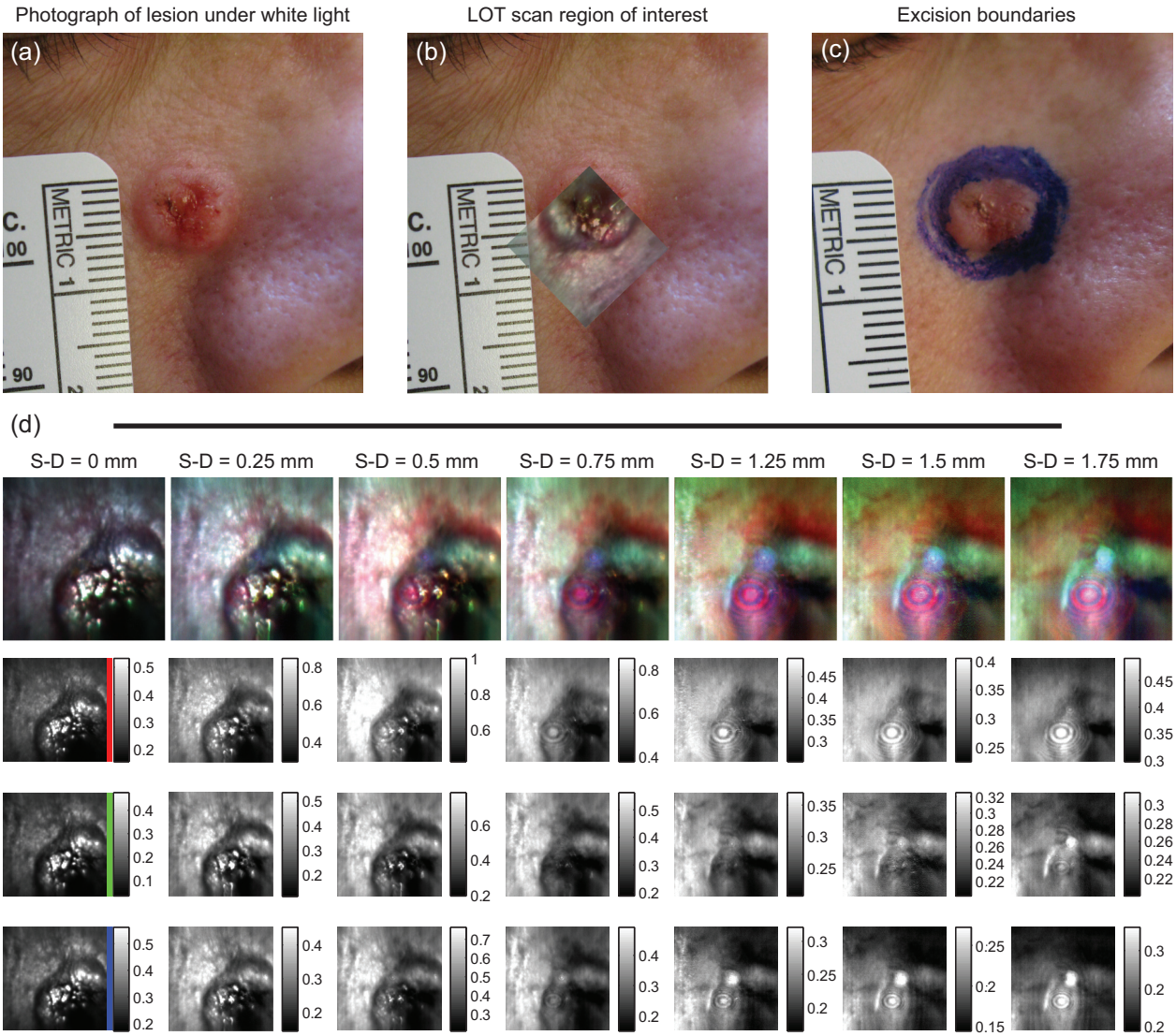

Figure 3-13 LOT imaging of SCC (a) Photograph of SCC lesion the face. (b) LOT overlaid on the photograph indicating the scanned region of interest. (c) Photograph of excision boundaries. (d) RGB merged LOT data and gray scale images of the the multi-wavelength data set for each source-detector offset distance.

Mapping of depth dependent features

As an alternative to viewing LOT data as individual source-detector separation images, each pixel can be thought of as having a curve of intensity values made up of measurements from each source-detector separation distance measurement at that pixel. The shape of the curve is characteristic of the underlying optical properties at that position. The top portion of Figure 3-14

contains a plot of the intensity as a function of source-detector distance for two regions of interest, ‘A’ and ‘B’. In order to provide a metric describing the shape of the curve, the curves were fitted to an exponential decay model. The fitted data suggested that the tissue in region ‘A’ more strongly attenuates the light measured by the narrower source-detector separations than the tissue in region ‘B’.

A pixel by pixel display of the exponential decay constant for each wavelength provides an alternative means of displaying the LOT data and encapsulates the information from each source-detector separation into a single image. This technique was applied to the data set with the resulting fit maps shown in the row labeled ‘fit’ in Figure 3-14. The scale bars alongside each map indicate the value of the decay constant at each pixel . Beneath each fit map is a map of the root mean square error (RMSE) measuring the goodness of fit of between the pixel data and the fitted curve. The RMSE maps highlight artifacts such as the specular reflection from the surface of the lesion. Closer examination of the RMSE map shows that it also revealed the circular rings associated with specular reflections from optical components within the system.

The stained tissue sections (Figure 3-15) were analyzed for correlation with regions with large (more negative) fitted decay constants (blue) as the fit map predicted that these areas had higher levels of absorption. The dashed lines in the ‘raw’ data LOT images of Figure 3-14 show the orientation of each slide with the sample dots at the end of the lines are shown to further orient the section within the tissue. The yellow arrows in the figure point out intravascular blood while the green arrows indicate a nest of subepithelial tumor cells. The location of these within the tissue sample was thought to be near the regions of increased attenuation and may have therefore contributed to the higher attenuation in that region.

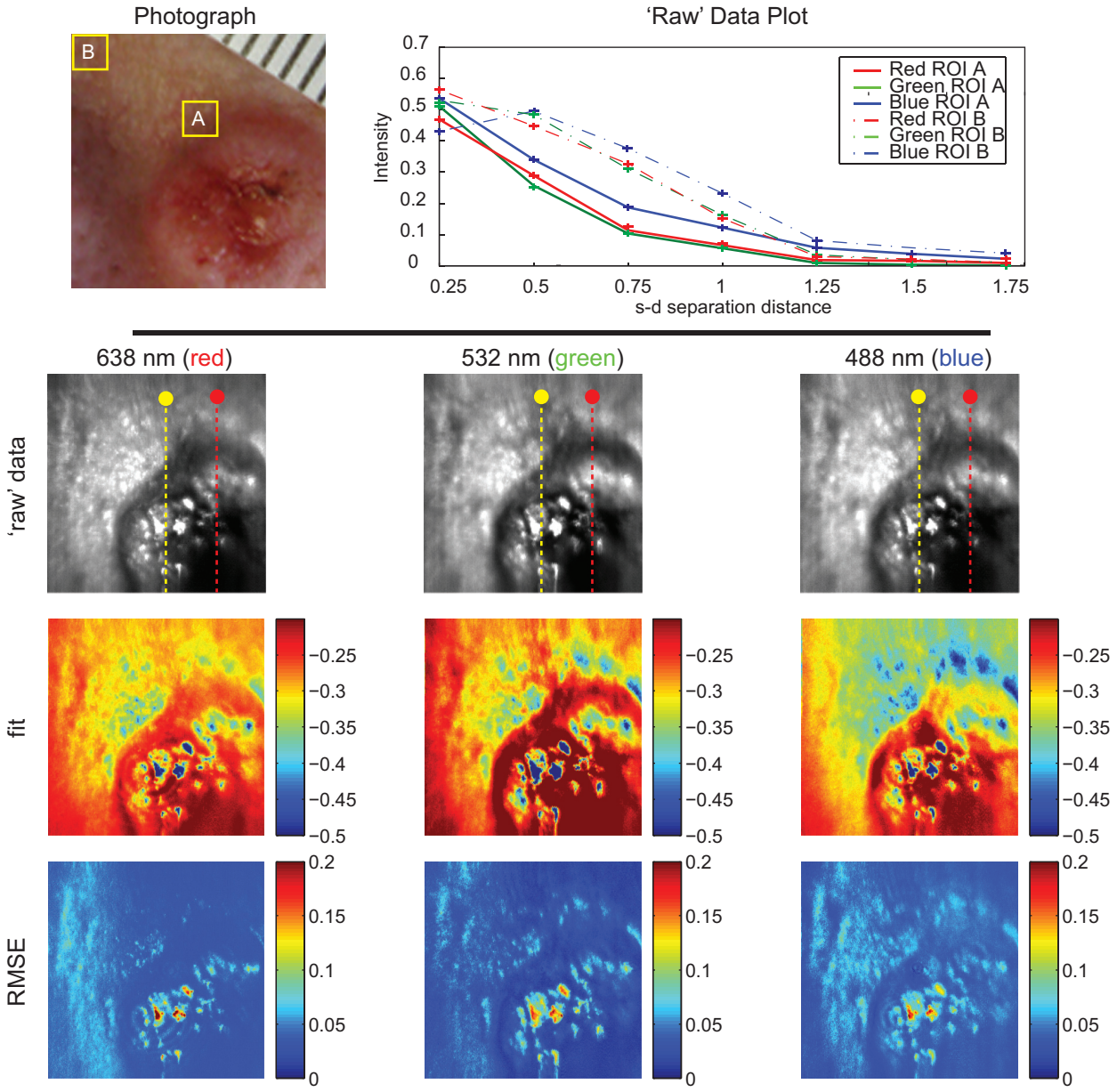

Figure 3-14 Pixel by pixel analysis of LOT data. Top, photograph of SCC lesion showing region of interests (ROI) A and B whose average pixel value is plotted as a function of source-detector position in the 'Raw' Data Plot. Fit plot shows fit of 'raw' data to an exponential function. Bottom, 'raw' data images for each wavelength showing location of histological tissue section. Fit images are maps of the fitted decay constants for each pixel. Larger decay constants (more negative) indicate higher absorption in the narrower source-detector separation channels. RMSE maps beneath each fit map provides a measure of the goodness of fit and reveal specular reflections from the surface of the lesions.

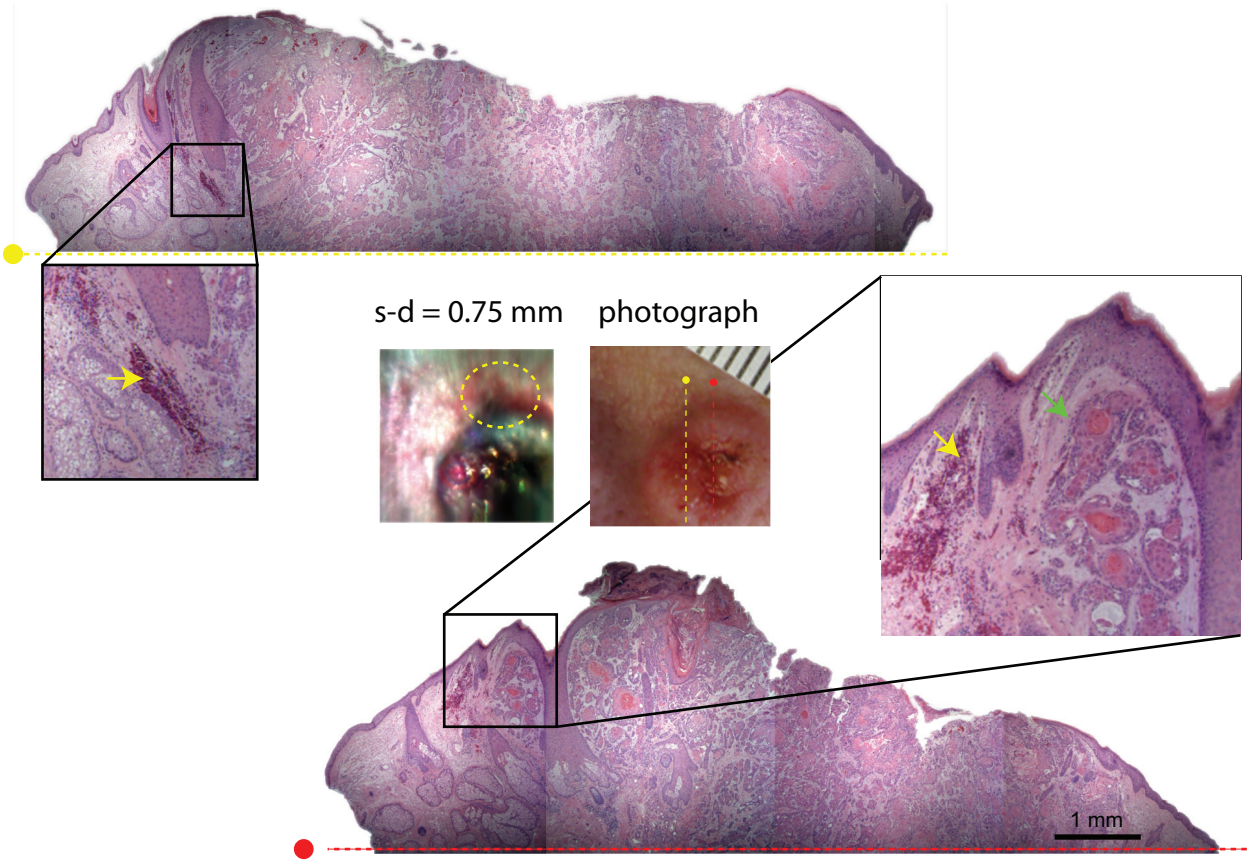

Figure 3-15 H&E stained sections showing intravascular blood (yellow arrow) and presence of subepithelial tumor cell (green arrow). Orientation of the slides is given by the dashed lines shown in the center photograph. 'Raw' data from the 0.75 mm source-detector separation image with yellow circle indicating region of increased absorption corresponding to region in histology with intravascular blood and subepithelial tumor cells.

3.1.4 Discussion

While the improvements made during the development of the second generation LOT system overcame many of the challenges of *in vivo* clinical imaging, additional improvements and further studies should be performed in order to make a definitive conclusion about the value of LOT skin cancer imaging. The study presented here showed that depth sensitive measures of LOT can accentuate subsurface features of a lesion and that the information rich LOT data sets can be analyzed in a variety of ways from simple visual exploration to pixel by pixel analysis.

More complex analysis can be performed to extract tissue chromophore concentrations as reported in [59].

The inability to remove or reject reflections from the clinical system posed a significant problem that would need to be addressed before embarking on another clinical study. Unlike the laboratory setting, where modifications to the system are easily made, the clinical system was located at a remote location and in an IRB approved configuration. Changing the system configuration from the fiber bundle interface to the articulating arm required approval from the IRB. An additional consideration for future clinical studies is the patient inclusion criteria. The study performed here initially only included patients undergoing surgical removal of lentigo maligna melanoma. As a result of the low patient recruitment, and the pilot nature of study, lesion inclusion was expanded to include BCC, SCC, and melanomas. While this improved patient recruitment, it ultimately led to a much more diverse set of lesions, making comparison between data sets difficult.

Upon conclusion of clinical data collection, the system was returned to the laboratory setting and reevaluated for imaging the rat exposed cortex. They system was transferred from its mobile cart onto an optical table, where the articulating arm was replaced with a rigid fixed position objective lens.

3.2 Rodent exposed cortex imaging

This chapter details the initial evaluation of our second generation LOT system for imaging the exposed rodent cortex *in vivo*. We begin with an introduction to neurovascular coupling, the phenomenon that we wish to study using LOT. We then review some common 2D optical imaging methods currently applied to optical brain imaging and describe how LOT can overcome some of the difficulties faced by these techniques. Lastly, we present pilot data acquired using the second generation LOT system to explore its sensitivity to FAD imaging.

3.2.1 Introduction

Neurovascular coupling is the interrelation between blood flow in the brain, and neuronal activity. Functional magnetic resonance imaging (fMRI) relies on changes in blood flow to infer the presence of neuronal activity. However, little is understood about the way that blood flow changes are controlled, or whether all changes in blood flow correspond to neuronal activity.

Studying neurovascular coupling in a brain that does not have intact blood flow, or full connectivity to the central nervous system is unlikely to provide a clear picture of the interrelation between neuronal activity and blood flow modulations. Therefore, utilizing imaging techniques that allow the brain to remain intact are strongly preferable. Optical imaging can be a valuable tool for studying neurovascular coupling [106] owing to the range of optical contrast sources and the high spatial and temporal resolution of techniques such as exposed-cortex intrinsic optical signal imaging and two photon microscopy. A significant challenge is to configuring optical measurements to capture numerous processes in parallel, at high-speed, and if possible in 3D.

3.2.1.1 2D optical imaging of the exposed cortex

Exposed cortex optical intrinsic signal imaging utilizes a CCD camera to capture high-speed images of a surgically exposed surface of the brain. Wide-field illumination of the brain with different wavelengths of light allows spectroscopic calculations to yield estimates of changes in HbO and HbR concentrations as shown in Figure 3-16A. Data acquired in response to a 4 second hindpaw stimulus using this technique is shown in Figure 3-17. Fluorescence from exogenous or endogenous fluorophores can also be measured as illustrated in Figure 3-16B.

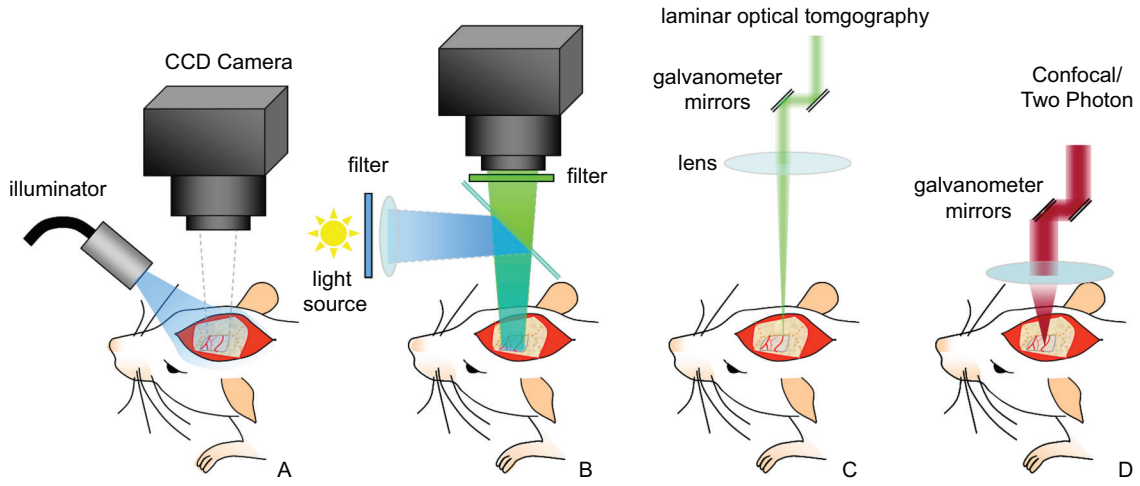

Figure 3-16 Different geometries used for exposed-cortex optical imaging in rats to explore neurovascular coupling. A: Exposed cortex intrinsic optical signal imaging, B: Epifluorescence imaging, C: Laminar optical tomography, D: Confocal or two-photon microscopy.

While intrinsic optical signal imaging has been widely used to study the functional responses in the exposed cortex [107-109], it suffers from the limitation that images are a 2D projection of 3D information. As illustrated in Figure 3-18, rodent cortex is around 2 mm thick and is heterogeneous in depth both in terms of its vasculature and neuronal structures. The main vessels of the brain coarse over the surface and abruptly dive to supply deeper capillary beds that nourish the neurons in deeper layers. While 2D exposed cortex imaging can readily capture the dynamics of these most superficial arterioles and veins, because of light scattering, hemodynamic signals

from the deeper capillary beds contribute much less to the detected signal, and their relative magnitude is difficult to quantify.

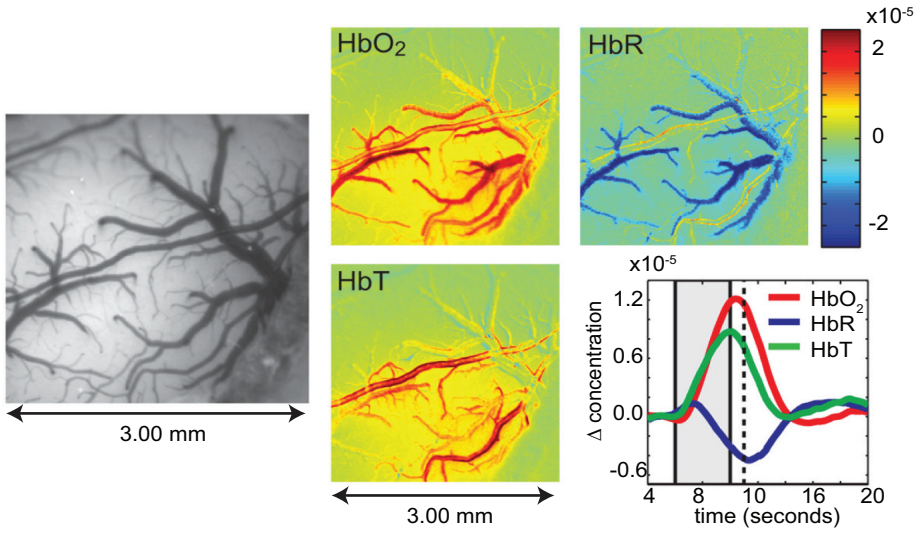

Figure 3-17 Typical images acquired with exposed-cortex intrinsic optical signal imaging (reproduced from Bouchard et al [110]). Hemodynamic response to a 4 second hindpaw stimulus is captured. Left, grayscale image of exposed rat somatosensory cortex. Right, images of changes in concentration of HbO_2, HbR, and HbT at t = 11 seconds (dotted line on time course). Time course plot shows the average change in HbO_2, HbR, and HbT concentration across the entire field of view. Timing of hindpaw stimulus is shown in the grey region.

A further limitation of 2D optical imaging of the exposed cortex is that conversion of multispectral data into oximetric concentration changes relies upon a number of assumptions. In Section 1.1.1, the ability of the Beer Lambert law to convert changes in intensity to changes in the concentration of an absorber was described. Conversion required knowledge of the path length over which the light had travelled in an absorbing medium. In 2D optical imaging of the exposed cortex, all detected photons have scattered within the tissue sufficiently to reverse their direction and reach the camera's lens, but the distance that each has traveled is unknown. Conversion of 2D optical imaging data is therefore usually achieved via an estimate of the average path length likely to have been traveled by each detected photon. This estimate can be

calculated via a Monte Carlo simulation. The simulation must utilize estimated background optical properties of the brain tissue at each specific wavelength and must make the assumption that all photons have traveled the same distance, that light of different wavelengths has probed the same tissue, and that the heterogeneity of the tissue has not systematically affected different pixels.

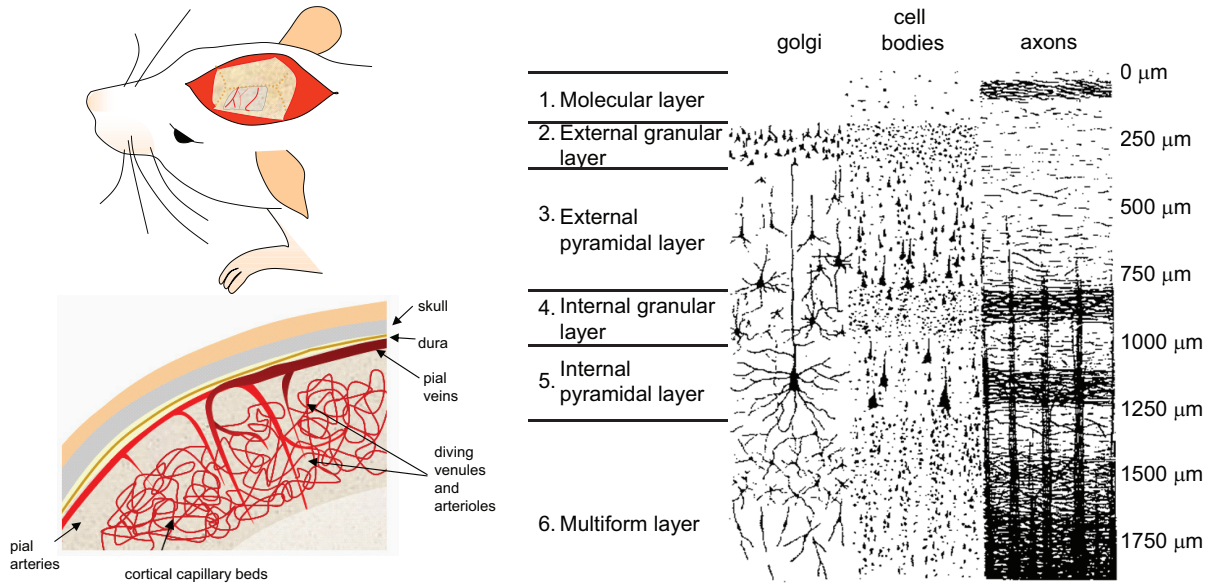

Figure 3-18 Layered structures of the cortex. Both the vasculature and neuronal organization are heterogeneous with depth. (sketch from [111]). Layer 2 of the cortex is thought to receive inputs from other cortical layers, layer 3 output to other cortical regions, layer 4 receives inputs from outside the cortex, and layer 5 outputs to the brain stem and spinal cord.

Wide-field fluorescence imaging of the exposed cortex can be used to capture signals from exogenous contrast such as calcium sensitive dyes [110], as well as intrinsic fluorophores such as flavin adenine dinucleotide (FAD) [112]. In this case, 2D images will show changes in the fluorescence intensity detected when the fluorophore is illuminated at the appropriate excitation wavelength. A filter placed in front of the camera prevents the excitation light from entering the camera. Figure 3-19 shows data acquired during 4 second, 3 Hz hindpaw stimulation after the brain was injected with Oregon Green BAPTA1-AM calcium sensitive dye. Bright flashes in

signal are observed as neurons fire in synchrony with the delivered stimulus, while a slower change in absorption is observed, corresponding to an increase in blood flow in the same region.

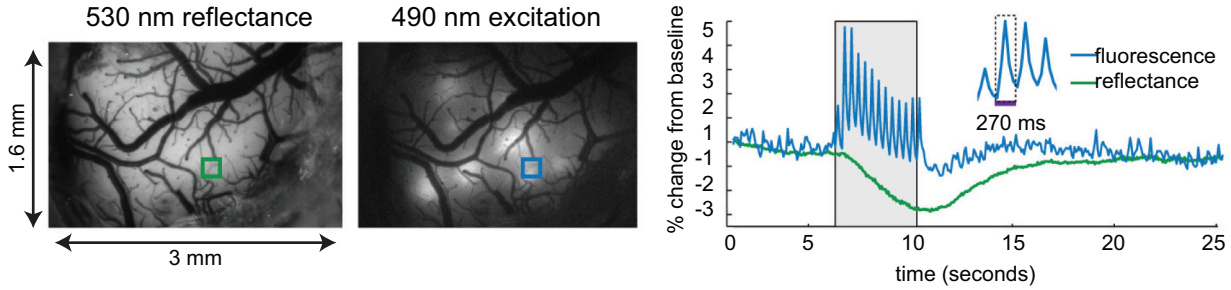

Figure 3-19 2D calcium sensitive dye fluorescence and absorption optical imaging of the exposed cortex acquired using high-speed 2D camera imaging (reproduced from Bouchard et al [110]). This system interlaces blue and green illumination while the camera captures alternate frames through a 500 nm long-pass filter allowing green reflectance and calcium sensitive dye fluorescence to be acquired in sequentially. (b) The time-courses showing the changes in reflectance and fluorescence from the regions indicated in the maps to the left. Spikes in calcium sensitive dye fluorescence can be seen for each hindpaw stimulus delivered at 3Hz, corresponding to neuronal firing, while the green reflectance signal shows the slower increase in absorption due to the corresponding increase in blood flow. The patchiness of the fluorescence map is caused by the need to pressure-inject the calcium sensitive dye into the cortex at a range of locations, leading to uneven loading of cells.

Wide-field 2D fluorescence measurements suffer from similar limitations as absorption measurements, in that the depth from which the detected signal originates is not known and differences in signal onsets at different depths cannot be resolved. A further problem associated with wide-field fluorescence imaging is the impact of simultaneous changes in absorption on the detected signal. For example, in Figure 3-19, there is a noticeable decrease in the fluorescence signal following the cessation of stimulus that could be interpreted as evidence of neuronal inhibition. However, the excitation and emission wavelengths of the calcium dye (488 nm and 520 nm) correspond to wavelengths that are strongly absorbed by hemoglobin. Since Figure 3-19 also shows simultaneously acquired green (530 nm) reflectance light in the same region, it is

clear that the increase in absorption at this wavelength (and also at 488 nm) would account for the decrease in fluorescence observed at this time.

As described in Section 1.2.2, two-photon microscopy can provide depth-sectioned fluorescence imaging in living tissues. The technique can be used to image cellular structure and function, as well as blood flow via dextran conjugated intravascular dyes. However, two-photon microscopy typically images only a single plane at a time, with a small field of view, and is not sensitive to changes in hemoglobin oxygenation, making it difficult to capture interrelated responses in parallel.

Using LOT to capture absorption and fluorescence data on the exposed brain therefore offers many advantages, including the ability to discriminate between signals originating from different depths in the cortex, while also offering the opportunity to more rigorously solve for quantitative changes in absorption and fluorescence (and their effects on each other).

3.2.1.2 LOT measurements of brain function to date

LOT was first developed as a tool for depth-resolved imaging of the rodent cortex [1, 67]. Using a first-generation system, Hillman et al used LOT to explore the depth-dependence of the hemodynamic response to forepaw stimulation in the rodent somatosensory cortex. The ability to distinguish between the temporal behavior of the arterioles, capillaries and veins of the responding region as shown in Figure 3-20 was demonstrated. However, the system used in those studies acquired data at only 10 frames per second (100 x 100 pixels x 8 separations) and at two wavelengths (473 nm and 532 nm) sequentially interlaced using shutters which yielded a net frame rate of 5Hz. The system was able to image fluorescence, as detailed in [68], but could not

acquire fluorescence and absorption data in parallel. Signal to noise was poor with the data shown in Figure 3-20 corresponds to an average of responses from 140 repeated stimuli.

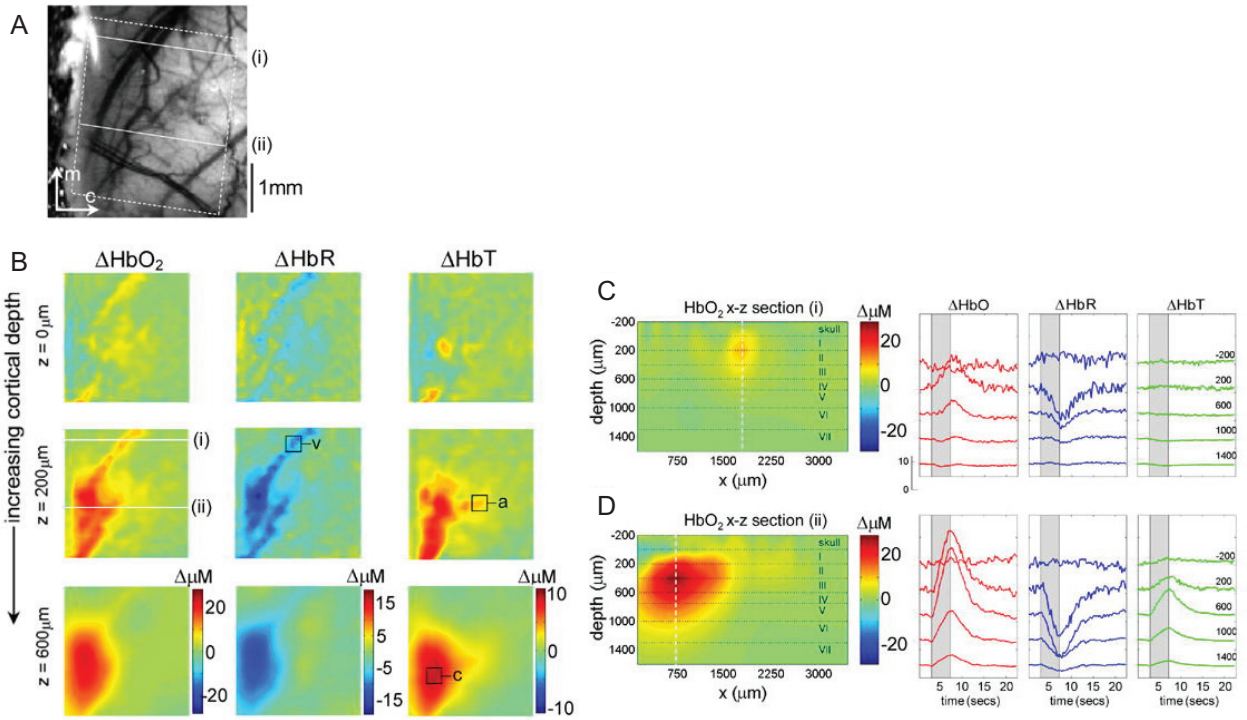

Figure 3-20 First-generation LOT data showing the depth-resolved hemodynamic response to 4 second forepaw stimulation in rodent somatosensory cortex system (reproduced from Hillman et al [67]). (A) CCD image of rat cortical surface (through thinned skull). (B) Depth-resolved LOT images of $\Delta[HbO_2]$, $\Delta[HbR]$ and $\Delta[HbT]$ in the cortex 0.6 s after cessation of the stimulus. (C) Depth-resolved cross section of the HbO_2 response at the position indicated with (i) in panel B, representing a large draining vein. The corresponding HbO_2, HbR and HbT depth-resolved time-courses around x=1800 μm (dotted white line) are shown to the right. (D) Depth-resolved cross section of the HbO2 response at the position indicated with (ii) in panel B. The corresponding HbO_2, HbR and HbT depth-resolved time-courses around x=750 μm are shown to the right. Numbers on each temporal trace represent their depth of origin in microns. 'a', 'v' and 'c' denote regions identified as arteriole, vein and capillary.

3.2.1.3 Imaging FAD fluorescence with second generation LOT system

While the results presented in Figure 3-20 from Hillman et al [67] demonstrated 3D high resolution optical imaging of hemodynamics in the exposed rodent brain, the information gained from these studies related more to resolving differences between vascular compartment

responses, and did not reveal measureable differences in the onset or evolution of the hemodynamic response that could be attributed to layer-specific hemodynamics [113]. In fact, given the slow onset times of blood flow changes in the cortex following stimulation (300-400 ms after stimulus begins), blood flow changes would be unlikely to reflect any layer-specific dynamics that correspond to interlayer relaying of signals within neuronal networks, which would happen on the order of a few tens of milliseconds.

However, a seminal paper in 2003 [112] demonstrated that it is possible to detect the weak autofluorescence of FAD using wide-field fluorescence imaging of the exposed cortex. FAD is a coenzyme involved in mitochondrial oxidative metabolism. Its counterpart, $FADH_2$ is not fluorescent, meaning that when $FADH_2$ is converted to FAD during oxidative phosphorylation, an increase in detected fluorescence would be expected, and is routinely seen immediately after the onset of somatosensory stimulus as shown in Figure 3-21. Not only is FAD a potentially valuable surrogate marker for neuronal activity, it is a valuable parameter for understanding neurovascular coupling. Many questions remain unanswered regarding how the brain controls and utilizes its energy supply, with a popular model being that the brain undergoes both aerobic and anaerobic metabolism during functional stimulus, the latter of which would not change FAD levels [114, 115]. Despite increased use for functional mapping, FAD measurements are also affected by the influence of absorption on detected signals, as described for calcium sensitive dye imaging above. This can be clearly seen in Figure 3-21, where a strong decrease in FAD is seen after the onset of a large increase in HbT concentration, which would strongly absorb at the excitation and emission wavelengths of FAD (~470 nm and 530 nm respectively).

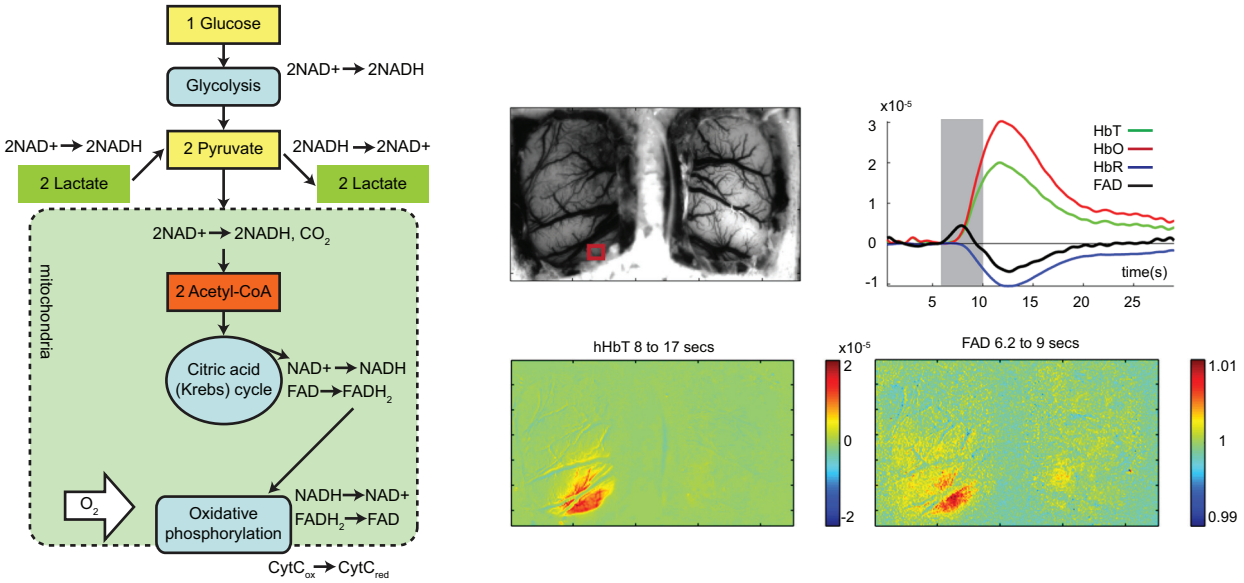

Figure 3-21 The role of flavin adenine dinucleotide (FAD) in cellular respiration. The image on the left depicts the process of cellular respiration. FAD is involved in oxidative metabolism within the mitochondria, where it is reduced and oxidized to and from the $FADH_2$ during the Krebs cycle and oxidative phosphorylation respectively. Since $FADH_2$ is not fluorescent, changes in FAD that correspond to changes in metabolism can be detected. The image panel to the right shows bilaterally exposed rat somatosensory cortex imaged using our 2D camera imaging system. The maps below shows peak responses in HbT and FAD fluorescence during unilateral hindpaw stimulation. The time-course plot shows the evolution of both hemodynamic and FAD signals. FAD fluorescence can be seen to increase slightly before increases in blood flow.

For the reasons described above, LOT imaging of FAD fluorescence could provide highly valuable information for neurovascular coupling research. Since changes in FAD originate in the mitochondria of cells within the cortex, recording of depth-dependent FAD dynamics could reveal interplays between neuronal layers that have yet to be explored. Furthermore, the ability of LOT to quantitatively solve for changes in absorption coefficients as demonstrated in the phantom studies in Section 2.3.4 could allow improved compensation for cross-talk between FAD fluorescence and absorption changes due to blood flow modulations.

To embark upon these studies, pilot study measurements are needed to determine whether LOT is capable of measuring FAD dynamics *in vivo*. Three steps were used to approach this: 1)

Fluorescence properties of FAD *in vitro* were measured to optimize the choice of light source and filters. 2) The clinical LOT system was converted into an optimized bench-top configuration suitable for rodent brain imaging, and 3) *In vivo* measurements were acquired, first with a wide-field 2D camera imaging system, and then with LOT. These steps are described in more detail below.

3.2.2 Pilot studies

3.2.2.1 Measurements of FAD fluorescence in-vitro.

To ensure that the 488 nm laser in LOT could excite FAD, we made a 5 mM solution of pure FAD (F6625, Sigma) in phosphate saline and measured the excitation-emission spectrum in steps of 10 nm using a skin-scan (Jobin Yvon) fiber-coupled scanning spectrofluorimeter. The resulting excitation-emission map is shown in Figure 3-22.

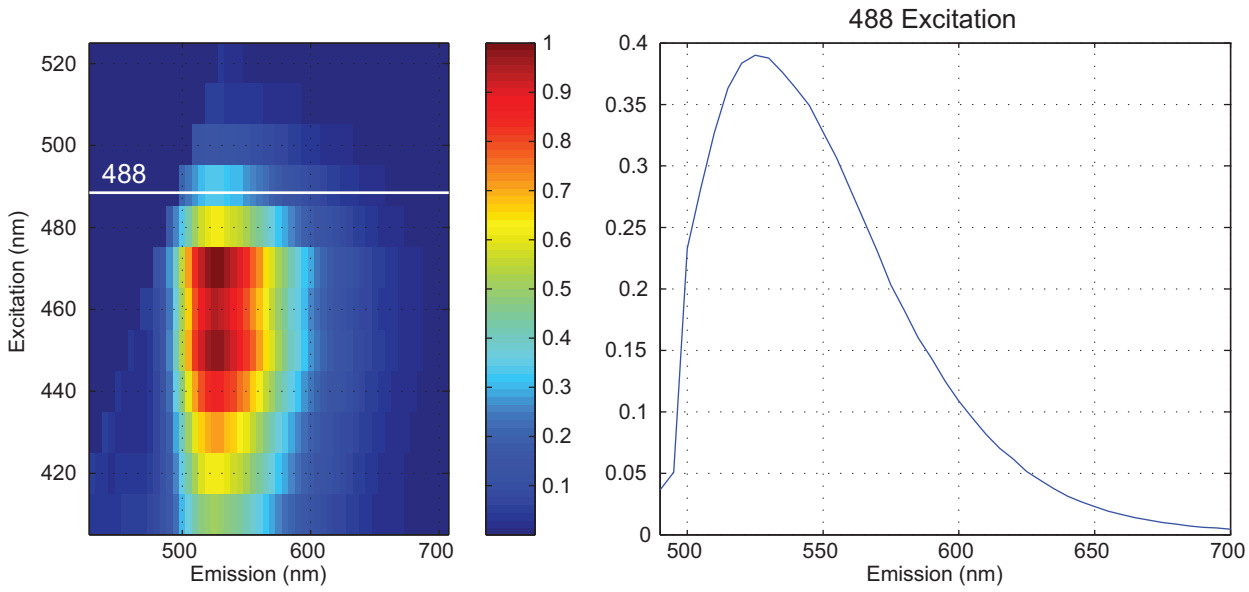

Figure 3-22 Excitation-emission spectrum of FAD (left) and the emission spectrum of FAD under 488 nm excitation (right).

This measurement demonstrated that FAD excites across a range of wavelengths from around 400 nm to around 500 nm, emitting in a band around 530 nm. While not optimal, we concluded that our 488 nm laser would be able to provide around 40% of the excitation of FAD than we could expect with a slightly lower ideal wavelength of 470 nm. Emission filter design is described further below.

3.2.2.2 Preparation of the LOT system for rat brain imaging.

As briefly mentioned at the end of Section 3.1.4 several changes were made to the system in order to allow for imaging of the rodent brain with the largest change being that the system was moved from the cart to a rigid benchtop setup (Figure 2-24). By placing the system on an optical table, we were able to reduce system vibrations which is especially important for long duration, high frame rate imaging. The main optical components were elevated from the table such that the rat could be easily positioned under the objective. The articulating arm interface was replaced with a semi-stationary objective lens with an adjustable lens tube to allow small adjustment to the height of the focus with the rat positioned in the sample plane. This change was significant as it removed the additional mirrors added by the articulating arm which help to reduce the influence of reflections in our measurements. The lasers were moved from the cart to the back of the optical table and transmitted via a free space setup. Higher intensity incident light could therefore be achieved since coupling and transmission losses associated with the fiber optical cable were eliminated.

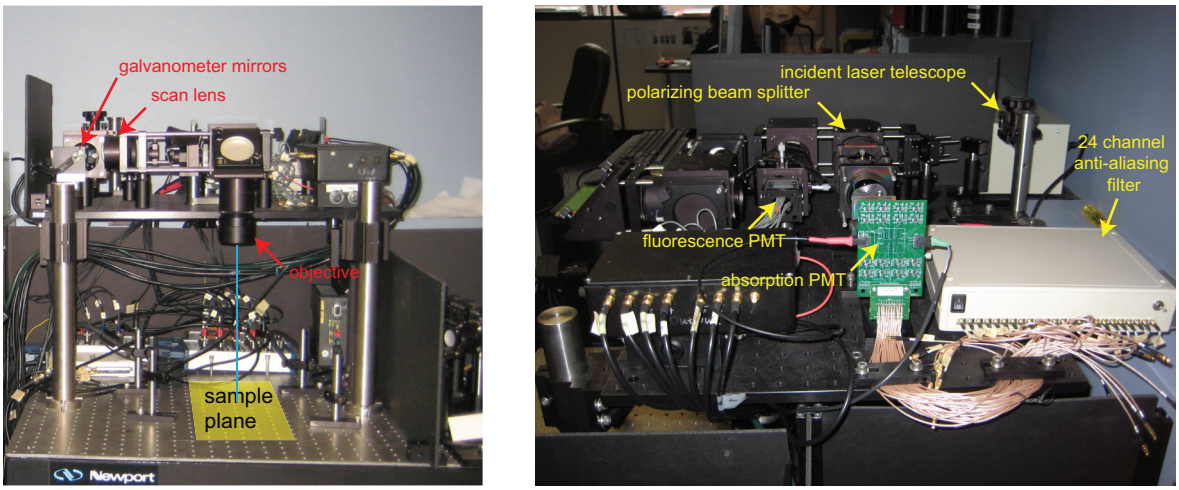

Figure 3-23 Photographs of benchtop system configuration. Optical components were elevated allowing easy placement of the stereotaxic frame in the region labeled 'sample plane'. Right, photograph of optical board

The system electronics were also revisited during the reconfiguration during which the PMT interface board was developed and anti-aliasing filter was redesigned to that described in Section 2.1.2. In order to allow for synchrony between the imaging runs and the application of a stimulus, the LOT control software was modified to trigger the start and stop of the electrical stimulus. The last step in preparing the system for FAD imaging was to select an appropriate filter for use in front of the PMT. The purpose of this filter was to reject any 488 nm blue excitation light that might be reflected towards the fluorescence detection arm by the 3-line dichroic filter.

The final system's configuration offers substantial benefits compared to the first generation system used for early rat brain imaging. The scan rate of the new system was over 18 frames per second when capturing 128 x 128 pixel images, more than 3x the frame rate of the first generation system while capturing higher density measurements (128 x 128 pixel images vs. 100 x 100 pixel images). Three wavelengths can be acquired simultaneously, or for FAD, blue and red, can be acquired along with FAD fluorescence in parallel.

3.2.2.3 *In vivo* pilot studies

Animal preparation

A total of 3 Sprague Dawley rats were used in the experiments. The rats were anesthetized with a vaporized isofluorane (2-3% inhalation in 3:1 air:oxygen mix) and mechanically ventilated following tracheal intubation. Both the femoral artery and vein were cannulated to allow for continuous blood pressure monitoring and delivery of intravenous fluids. Core body temperature was maintained at 37°C with a rectal thermometer attached to a homeothermic heating pad. The rats were then placed in a stereotaxic frame, the scalp retracted, and a portion of the skull (4 mm x 6 mm) overlaying the left somatosensory cortex was thinned using a dental drill. In order to relieve intra-cerebral pressure, the IVth ventricle was opened just prior to removing the thinned skull region. After removing the dura, 1.5% agarose dissolved in artificial cerebrospinal fluid was placed onto the exposed cortex and covered with a small glass coverslip. The optical window was completed by sealing the skull with dental acrylic. Electrodes were placed in the right hindpaw and connected to an electrical stimulus unit. Prior to imaging, the animals were switched to intravenous delivery of alpha-chloralose (40 mg/kg/hr) administered through the femoral vein. All animal procedures were reviewed and approved by the Columbia University Institutional Animal Care and Use Committee.

CCD camera imaging of exposed cortex

Before imaging with LOT, the rats were imaged using a high-speed optical imaging system described in [110] and shown in Figure 3-16A above. The system was configured to acquire images in synchrony with strobing blue (470 nm) and green (530 nm) and red (630 nm) light

emitting diodes fitted with a 460 ± 30 nm, 534 ± 23 nm bandpass filters and a 580 longpass filter respectively. A 500 nm longpass filter was placed in front of the camera such that during blue illumination, the camera acquired cortical images of green autofluorescence and during green and red illumination the camera recorded reflected light. Imaging runs were performed by acquiring 30 seconds of data at 30 frames per second (resulting in 10 frames per second per LED) with 6 seconds of pre-stimulation, 4 seconds of stimulation, and 20 seconds of post-stimulation. During the 4 second stimulus period, 1 mA, 3 μs pulses were applied at 3 Hz were applied to the right hindpaw. Data sets were collected in sets of 5 runs and had a field of view of 4 mm.

LOT imaging of exposed cortex

With the LOT system implemented in a bench top configuration, the system was setup to acquire 128 x 128 pixel images at 300,000 samples/second resulting in a frame rate of 18 frames per second. The fluorescence detection arm was setup measure green fluorescence light by placing a 500 nm longpass filter in front of the fluorescence PMT to reject blue excitation light. The green laser was disabled during fluorescence scans, meaning that only blue and red reflectance were acquired simultaneously with green fluorescence resulting from the blue laser excitation. Imaging runs were performed by acquiring 14 seconds of data at 18 frames per second. The duration of the data acquisition was less than that of the CCD camera runs due to the limited speed at which the LOT computer can stream data from the data acquisition boards to the hard drive. Therefore LOT stimulus runs had 2 seconds of pre-stimulation, followed by 4 seconds of stimulations and then 8 seconds of post-stimulation. The amplitude, pulse width and frequency were the same as that used for the camera-based imaging. Calibration scans as described in

Section 2.2.2 were collected for subsequent data analysis. All data shown has a field of view of 4 mm x 4 mm.

3.2.3 Results

Figure 3-24 shows' raw' LOT reflectance scans (red, green and blue) acquired on the exposed somatosensory cortex of rat A. All 24 images were acquired simultaneously. The RGB merge demonstrates the spectroscopic content of the data. Arterioles appear more pink than darker deoxygenated veins, consistent with the absorption properties of HbO and HbR. Fluorescence channel 'raw' images are shown in Figures 3-25 and 3-26. Comparing this data to the skin data shown in Section 3.1.3, the signal to noise in the wider source-detector channels is improved owing to the redesign of the LOT system's signal conditioning electronics, as well as the improved calibration and reflection removal due to the removal of the clinical imaging articulating arm interface. The gradually displaced shadow of the surface vessels is also clearly seen. The shadow of the large superficial vein can also be seen to be moving across the image with wider source-detector separations in a similar way to the 'ruler' scans shown in Figure 2-13. System improvements made while transitioning to a bench-top configuration dramatically improved signal to noise, brought all 8 detection channels online, and almost completely eliminated specular reflection problems compared to the clinical skin data shown earlier. The field of view of each scan is 4 mm x 4 mm.

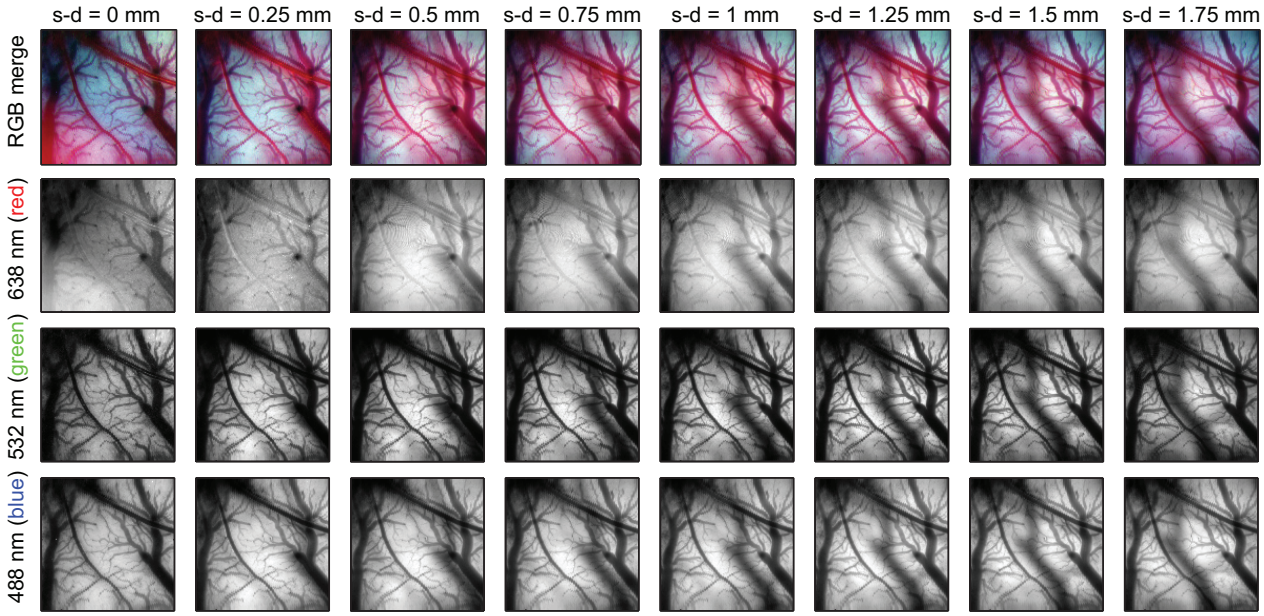

Figure 3-24 'Raw' LOT reflectance data acquired on exposed cortex of rat A. Top row shows RGB merge of 'raw' data from the red, green and blue reflectance channels of the second generation bench-top system. Rows below show each channel individually. All images shown were acquired simultaneously in one scan. Differences in the absorption of darker veins and pinker arterioles can be seen. The shadow of the large superficial vein can also be seen to be moving across the image with wider source-detector separations in a similar way to the 'ruler' scans shown in Figure 2-13. System improvements made while transitioning to a bench-top configuration dramatically improved signal to noise, brought all 8 detection channels online, and almost completely eliminated specular reflection problems compared to the clinical skin data shown earlier. The field of view of each scan is 4 mm x 4 mm.

3.2.3.1 Functional responses

Since the LOT data acquired are time-series, a simple analysis that can be performed is to extract the time-course of a region of interest. The top row of Figure 3-25 shows time-courses extracted from a region of interest in the data acquired on rat C for the first five source-detector separations. The response is typical of that seen in normal brain, with a decrease in blue reflectance and an increase in red reflectance corresponding to an increase in HbO and HbT and a decrease in HbR (as shown in Figures 17, 20, and 21). The reflectance time-courses shown along the bottom row of Figure 3-25 are a conversion of the data, using the modified Beer Lambert law, into Δ[HbO], Δ[HbR] and Δ[HbT]. The fluorescence channel of LOT exhibits an

initial increase in signal following stimulus onset, with an overall decrease in signal as the acquisition continues. The data shown has been calibrated using our standard procedure to correct for systematic errors, and then averaged over 10 repeated stimulus trials. Matlab function 'smooth3' was used to implement a 3D, 3x3x3 element box-car filter to the data shown.

The region of interest was selected after basic examination of the raw data. However, once a time-course is found, a map of the responding region can be generated by looking at the percentage change of the signal in each pixel at the peak time of the response, relative to the signal before the stimulus began. Areas that are responding should appear as high or low values of this percentage change, corresponding to whether the signal increased or decreased. Such maps are shown for rat C in the 3rd to 5th rows of Figure 3-25. The 'raw' fluorescence LOT images are provided in the top row for reference to the vasculature. These maps show a well-defined region exhibiting an increase in autofluorescence which coincides with the region showing a decrease in reflectance at 488 nm. The decrease in reflectance at 488 nm corresponds to a local increase in blood flow. The response in the red channel is a positive increase in reflectance corresponding to a reduction in the amount of HbR in the large draining vein. This result demonstrates that a localized increase in autofluorescence can be detected using LOT. Since the simultaneously acquired blue reflectance shows a decrease in detected signal, the autofluorescence signal cannot simply be the result of an absorption change. To further test this finding, control scans were acquired with the stimulus box disabled. In some cases, small oscillations in blood flow could be seen in the absence of a stimulus, but the data in Figure 3-26 shows only a slow trend in the red and blue reflectance and an exponential decay in the detected autofluorescence that corresponds to photobleaching.

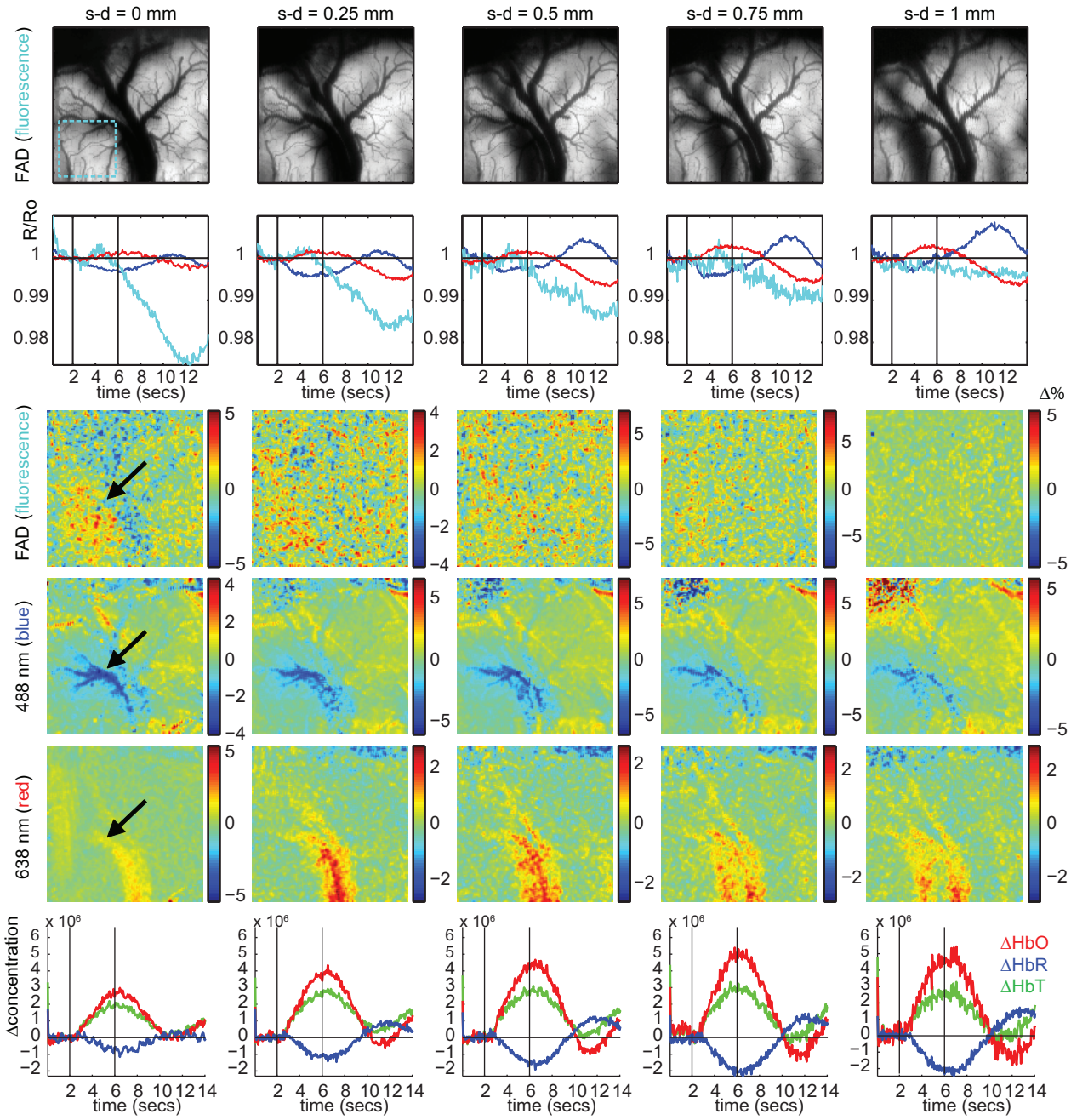

Figure 3-25 Functional responses in raw LOT data from rat C. Top row shows 'raw' fluorescence channel data for the first five source-detector separations. The second row shows the signal intensity extracted from the dotted cyan square in the top left image as a function of time for each source-detector separation. Red = red reflectance, blue = blue reflectance and cyan = fluorescence. The two vertical black lines denote the onset and cessation of 4 second hindpaw stimulation delivered at 3Hz. Rows 3-5 show maps of the % change in signal observed at the peak of each response, for each source-detector separation. Regions of response are highlighted by black arrows. Row 6 shows the red and blue reflectance data from row 2 spectroscopically converted into Δ[HbO], Δ[HbR] and Δ[HbT] time-courses.

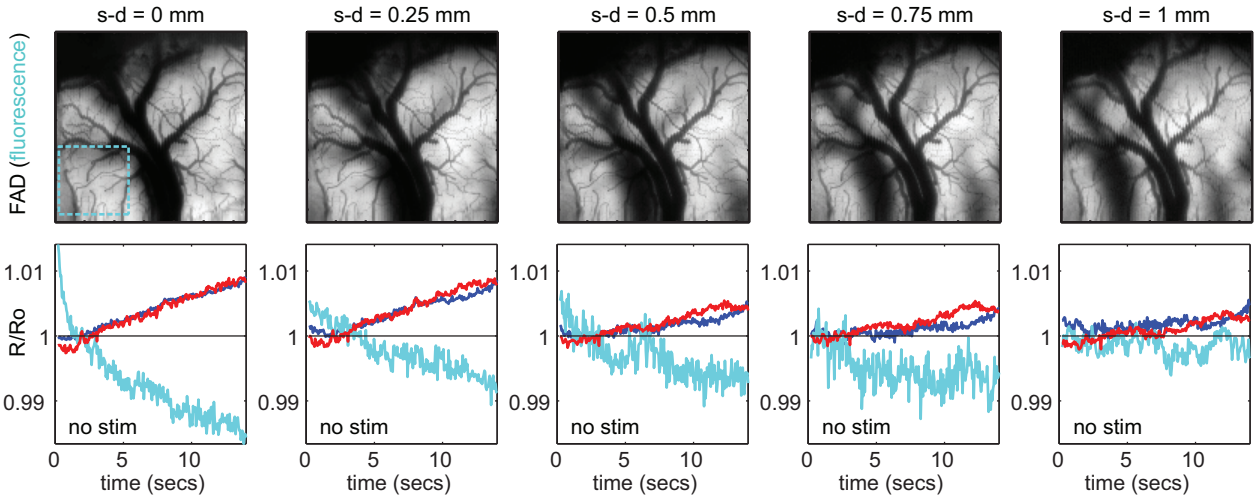

Figure 3-26 Control data (no stimulus). Bottom row shows time course signals of red and blue reflectance (red and blue lines) and the fluorescence signal (cyan) extracted from the region indicated by the cyan box in the top left image. The fluorescence trace, particularly for the first source-detector separation exhibits exponential photobleaching. The red and blue signals drift upwards together.

This trend matches the decay trend seen in the fluorescence data in Figure 3-25. Figure 3-27 shows data from the 2D camera imaging system on the same animal (rat C) showing similarly shaped regions responding during stimulation for green and red reflectance and fluorescence.

Figure 3-28 shows additional LOT data from rat A, revealing similar maps of responses with stronger photobleaching in the fluorescence channel. The responses show a clearly delineated map of increased fluorescence corresponding to a similarly shaped decrease in blue reflectance corresponding to an increase in local blood flow. The red channel maps look fairly flat, but a stripe of increase signal along the left-hand edge of the image can be attributed to decreases in HbR in the draining vein running along the edge of the field of view.

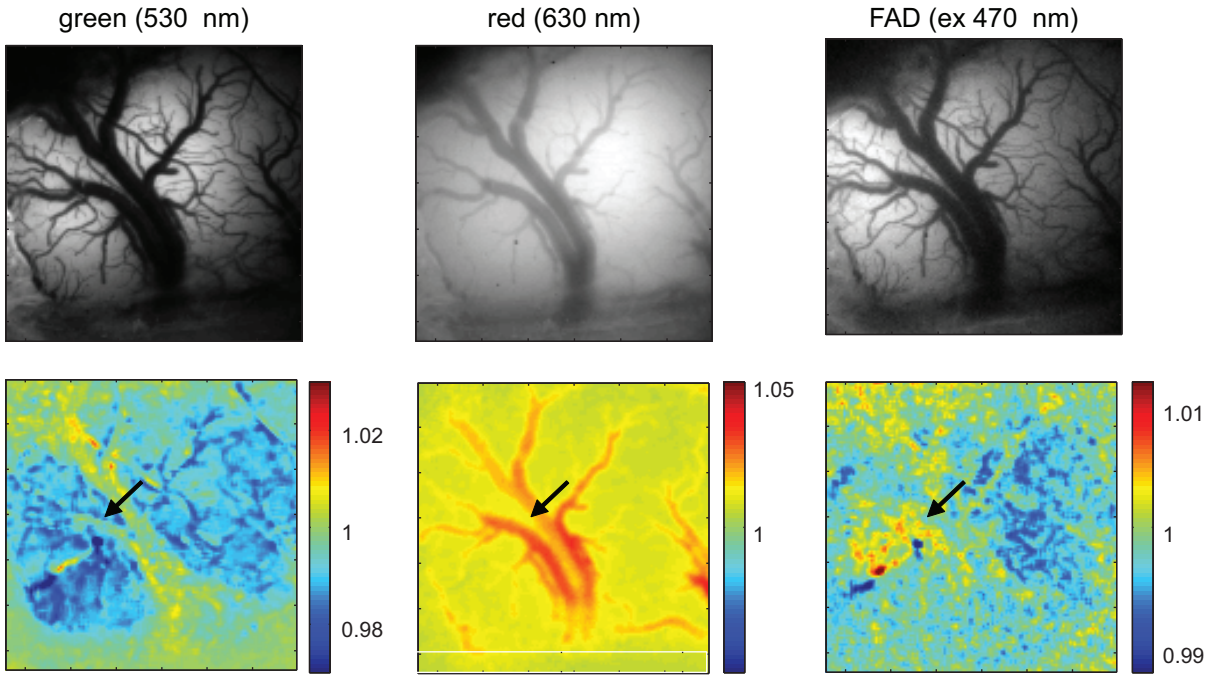

Figure 3-27 Functional maps derived from 2D camera imaging on rat C. Top row shows absolute images under green and red illumination as well as the fluorescence signal detected through the 500 nm long-pass filter during blue excitation. The bottom row shows maps of the fractional changes in signal for each of these illuminations at the peak of the functional response to hindpaw stimulation. The response seen in the green image is more diffuse that that seen with LOT, but is in a similar location as shown by the arrow. The red response agrees well with that seen in LOT, and is localized to the draining vein. The FAD response is small, but localized to a similar location to that seen with LOT.

To attempt to correct for the effects of photobleaching, the assumption was made that there were some regions of the field of view that were not exhibiting any functional response, and that any changes in this region would be similar to changes in the responding that corresponded to baseline drifts or photobleaching. The reflectance changes (for the blue and red lasers) as well as the fluorescence changes for the main responding region divided by the signal in this non-responding region (denoted by '1' and '2' respectively in the top row of Figure 3-28) is plotted in the 3rd row of Figure 3-28. These results show a clearer apparent increase in autofluorescence which correlates well with the stimulus, as well as more level red and blue reflectance time-courses that more closely resemble those in Figure 3-25.

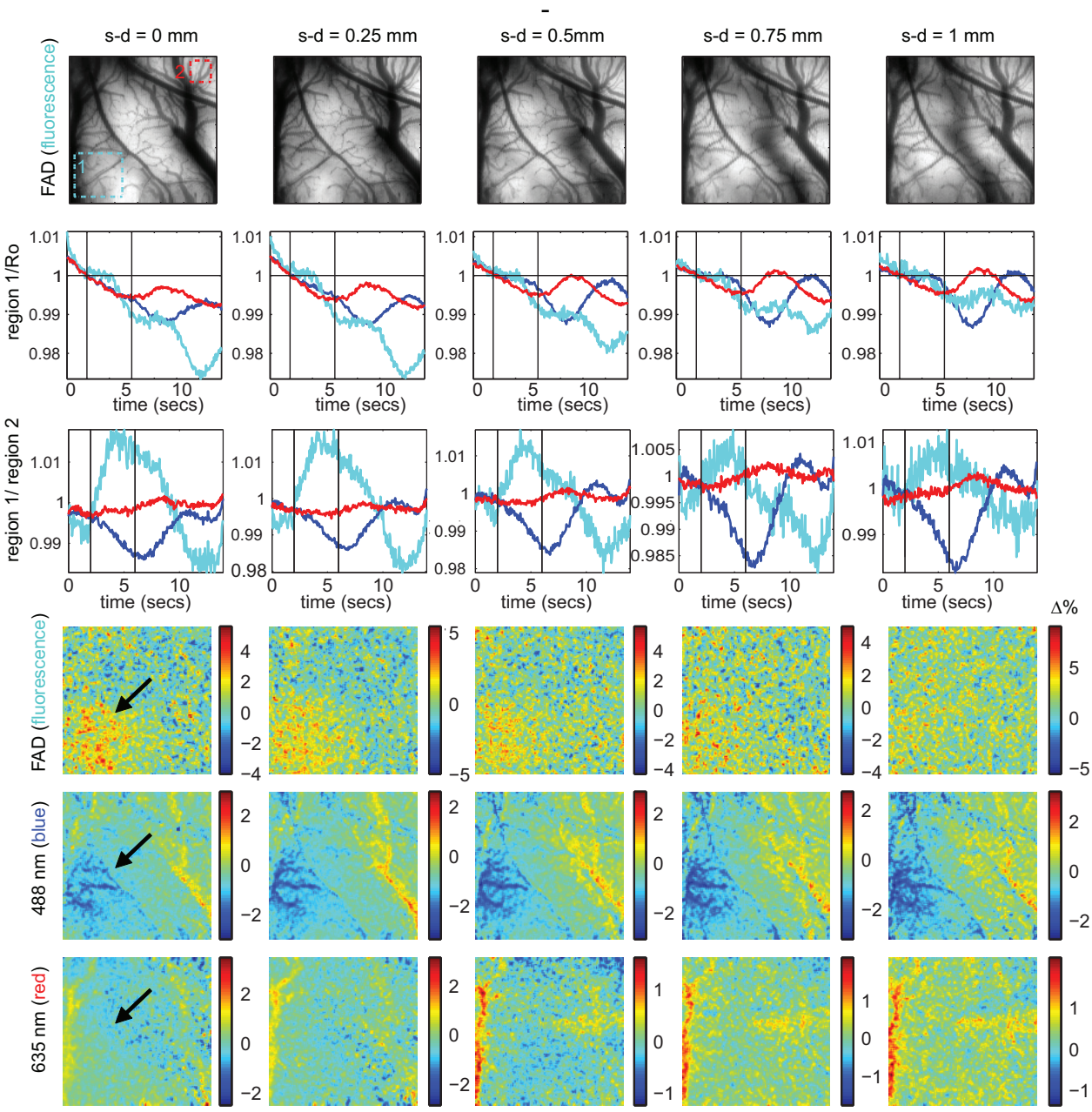

Figure 3-28 Functional responses in 'raw' LOT data from rat A. Top row shows 'raw' fluorescence channel data for the first five source-detector separations. The second row shows the signal intensity extracted from the dotted cyan square labeled '1' in the top left image as a function of time for each source-detector separation. Red = red reflectance, blue = blue reflectance and cyan = fluorescence. The two vertical black lines denote the onset and cessation of 4 second hindpaw stimulation delivered at 3Hz. Row 3 shows the same time-courses, corrected for photobleaching and drift by dividing by the signals extracted from the non-responding region labeled '2' in the top-left image. Rows 4-6 show maps of the % change in signal observed at the peak of each response, for each source-detector separation.

Another way to analyze this data is to use principal component analysis (PCA). This method finds the most common, orthogonal time-courses in the data set and renders images corresponding to the contribution of each time-course to a given pixel [116]. Through PCA analsyis, we found that the second component after PCA closely resembled the time-course of the stimulus response after baseline / autofluorescence correction. While this approach is not exact, Figure 3-29 shows that the second component of PCA in both rats C and A picks out the positive autofluorescence increase, and the reduction in blue light reflectance. The cortical vasculature is more prominent in the blue reflectance data than the fluorescence maps. Again, this result demonstrates that changes in fluorescence are spatiotemporally different to changes in reflectance, confirming that a different process is generating the signals detected in the fluorescence LOT channel beyond simple blood flow changes.

It is interesting that this method also suggests that the temporal shapes of the changes in absorption are fairly invariant with source-detector separation in both rats, which did not appear to be the case for rat C in Figure 3-25. This can be explained by the fact that the absorbing shadow of the superficial vein gradually moves over the responding region with wider separations in this orientation. Since the superficial vein will have different oximetric and temporal characteristics than the parenchyma [67] (see Figure 3-20), these venous signals are adding to the response and changing its shape for wider separations (while also reducing the detected fluorescence signal). The PCA maps demonstrate this effect, showing that the strong, consistently shaped absorption response in rat C localizes to the parenchyma under the superficial vein and its shadow.

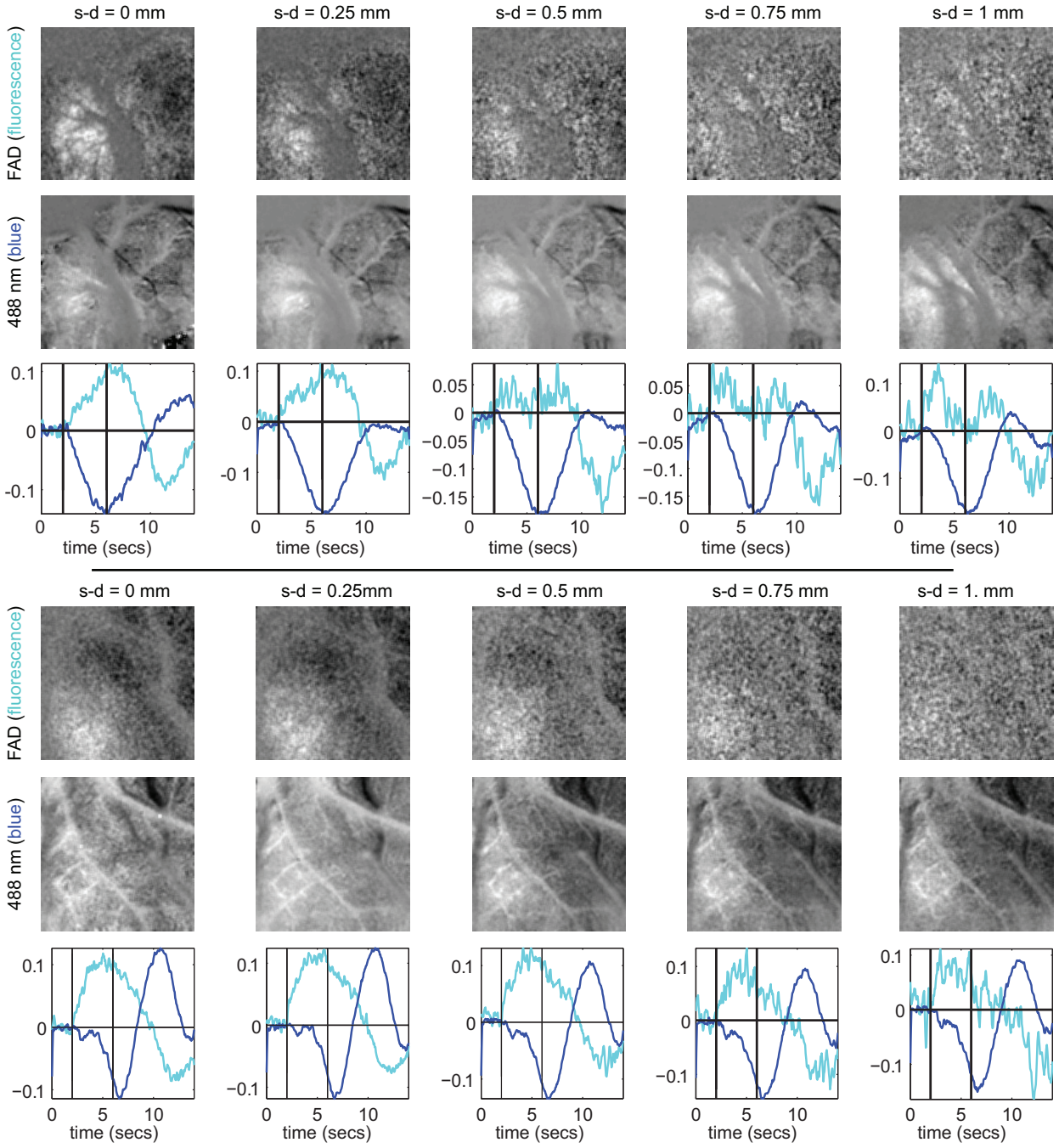

Figure 3-29 Principal component analysis of blue reflectance and fluorescence for both rats (top = rat C, bottom = rat A). Maps correspond to the second principal component, calculated for each source-detector separation individually and show the relative occurrence of the time-course indicated below the maps. All maps show a responding region whose time-course correlates well with delivery of the stimulation. Blue reflectance data shows more vessel-like structures than fluorescence maps. The time-courses of the fluorescence responses between the rats are similar, while the reflectance and fluorescence time-courses are sufficiently different, and opposite, to rule out the possibility that the increases in fluorescence seen are an artifact from absorption changes.

Are we seeing FAD?

The results presented above reveal positive changes in autofluorescence that correspond well to delivery of somatosensory stimulus in two separate rats (note that the physiology of rat B was poor, and no good functional responses were observed with camera or LOT measurements). The observed fluorescence responses seen were spatiotemporally similar, but not identical to the responses seen in blue and red reflectance. While there are numerous sources of autofluorescence in the body, there are relatively few in the living brain, with NADH and FAD being the most prominent. The *in vitro* FAD measurements acquired during preparation of the system for *in vivo* measurements suggest that the excitation wavelength and detected wavelengths were appropriate for detecting FAD fluorescence. The spatiotemporal differences between the reflectance and fluorescence responses shown in Figure 3-29 suggests that the hemodynamics can be independently and exactly simultaneously evaluated with respect to cellular metabolism using our second generation LOT system.

Decoupling of FAD and hemodynamic response

An interesting result that illustrates the value of this approach is shown in Figure 3-30 At this stage of the experiment, rat A was experiencing oscillations in cortical blood flow such that maps of localized increases in blood flow corresponding to stimulation could no longer be seen. Nevertheless, LOT captured responses to a 2 second long stimulation that revealed well localized and temporally correlated increases in FAD, despite the lack of correlating blood flow changes.

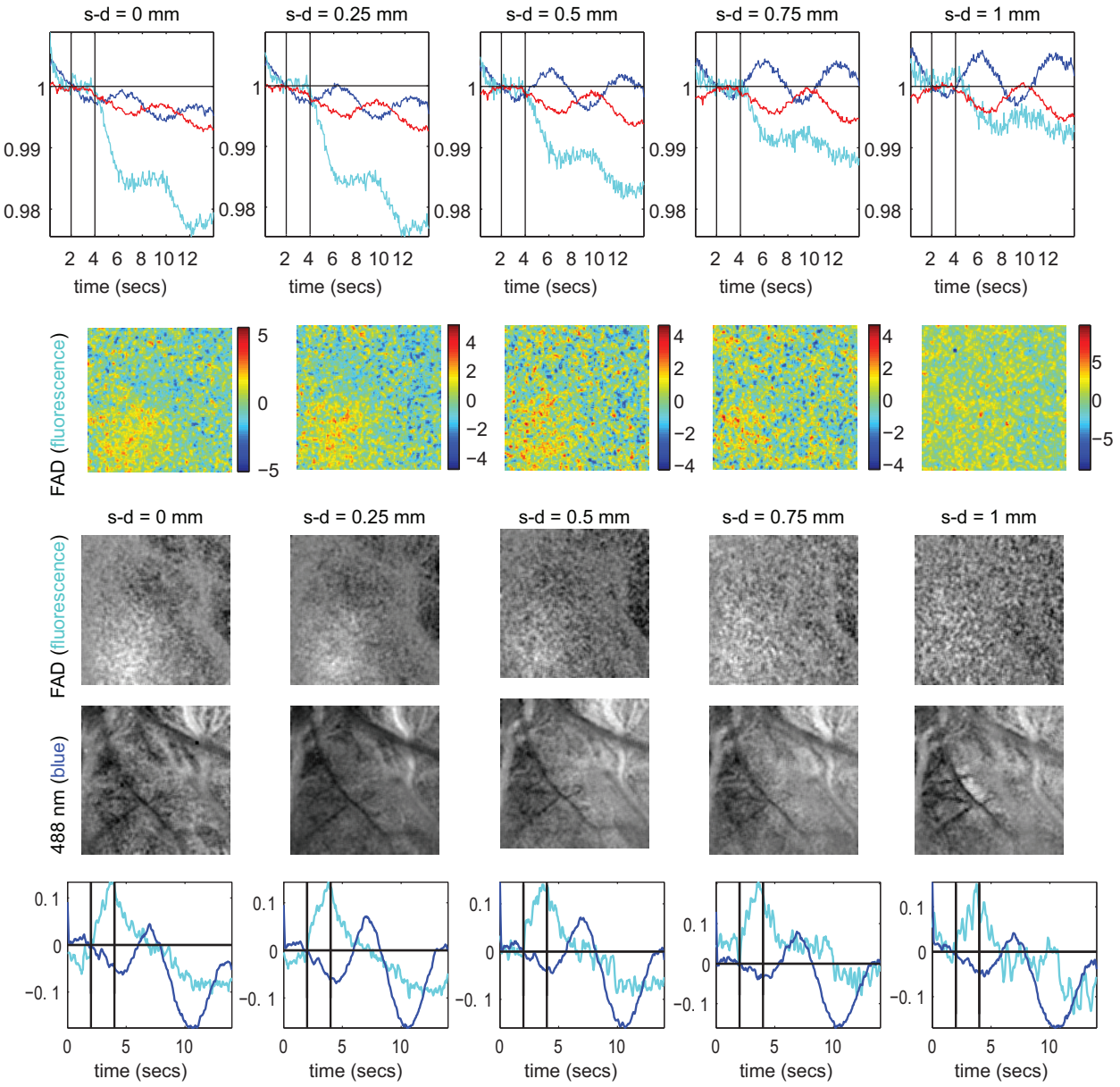

Figure 3-30 Responses from a single run in rat A where cortical blood flow began to oscillate. The top row shows the signal intensity extracted from the same field of view as in Figure 3-28. Red = red reflectance, blue = blue reflectance and cyan = fluorescence. The two vertical black lines denote the onset and cessation of 2 second hindpaw stimulation delivered at 3Hz. Clear oscillations can be seen in the reflectance data, as well as photobleaching in the fluorescence data. However, the second row shows that maps extracted from the fluorescence data still show good localization to the responding region. Maps of the red and blue reflectance data showed no regional localization (not shown). Rows 3-5 show PCA maps and time-courses from the same data, taking the second principal component. In contrast to the results in Figure 3-29, while the fluorescence signal shows a well correlated regional response, the blue reflectance map is neither temporally nor spatially correlated to the stimulus.

This is an exciting finding with respect to neurovascular coupling and interpretation of fMRI data, since it suggests that increases in oxidative metabolism, most likely corresponding to neuronal oxygen consumption, persist in the absence of a controlled local blood flow increase. Furthermore, this result shows that the oscillations in blood flow that are occurring do not correlate to underlying changes in neuronal energy consumption.

What does LOT tell us about the depth-dependence of the FAD signal?

The pilot data shown above demonstrated that LOT can detect meaningful changes in FAD fluorescence during stimulation and simultaneous acquisition of hemodynamic reflectance measurements. However, the eventual goal is to use the depth-discriminating ability of LOT to explore the depth-dependence of FAD changes in the cortex with respect to hemodynamic changes, and also to cortical layer specific dynamics. To explore what this pilot data can reveal about the depth-dependence of the signal, the data can be visualized as shown in Figure 3-31.The data shown is uncorrected for photobleaching.

The most striking trend in these plots is that in the blue and red reflectance measurements, there are fractional changes in reflectance that are larger in amplitude for the wider source-detector separations than for narrower source-detector separations. This is to be expected since wider separations have longer path lengths and, for most distributions of changing absorption, the Beer-Lambert law predicts that the log of fractional changes in intensity would be proportional to path length (x):

$$I(t) = I_0 e^{-\mu_a(t)x} \qquad \textbf{Eq 3-1}$$

$$\frac{I(t)}{I(t=0)} = e^{-(\mu_a(t)-\mu_a(t=0))x} \qquad \textbf{Eq 3-2}$$

$$\log\left(\frac{I(t)}{I(t=0)}\right) = -\Delta\mu_a x \qquad \textbf{Eq 3-3}$$

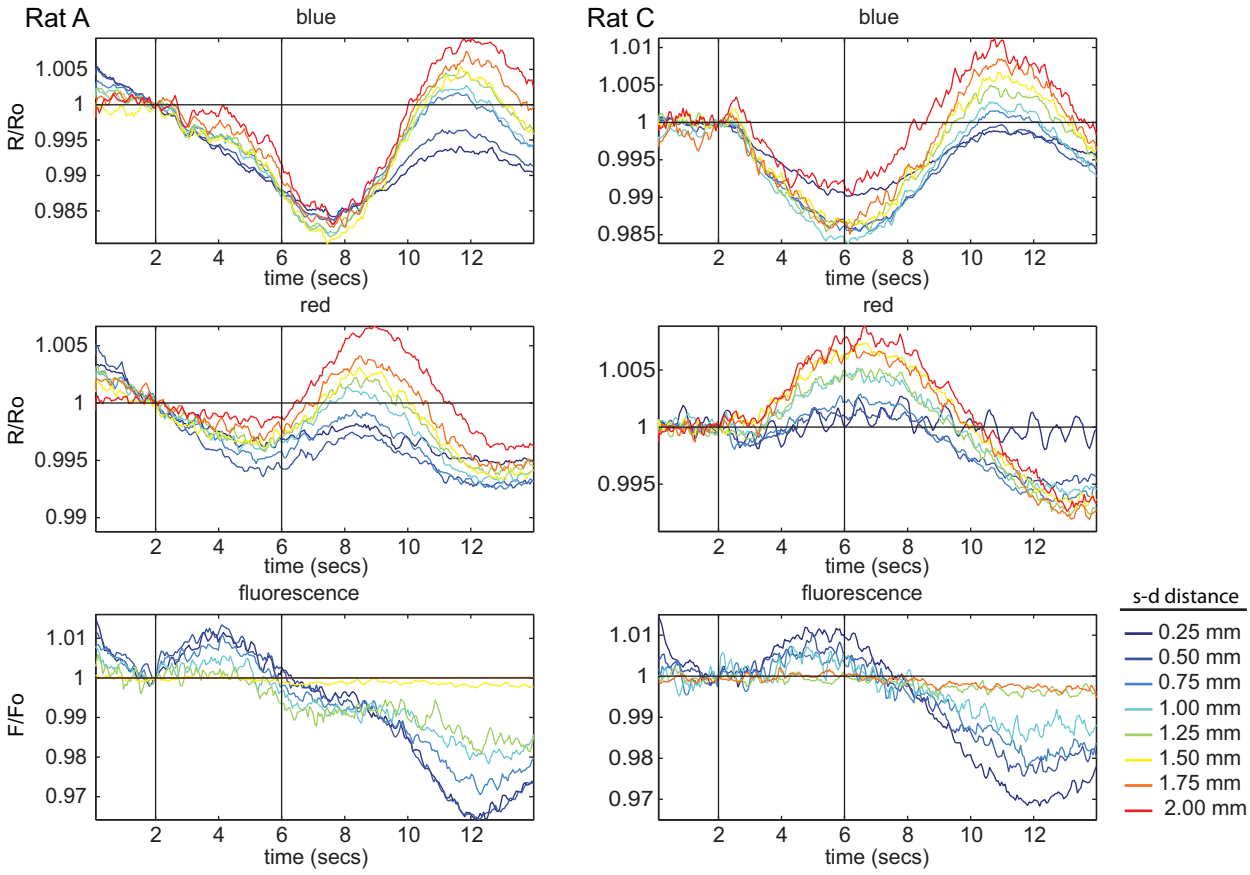

Figure 3-31 Comparison of fractional responses for each source-detector separation for rats A and C. Time-courses were extracted from the responding region and are not corrected for decays or photobleaching.

However, the fluorescence LOT time-courses have the opposite trend; the shorter source-detector separations exhibit the highest fractional change during stimulation than the wider (deeper) sampling source-detector separations. Similar Beer-Lambert analysis predicts that fractional

changes in fluorescence will be proportional to changes in fluorophore concentration but independent of path length as shown below:

$$I_{ex} = I_0 e^{-\mu_{aF} x} \qquad \textbf{Eq 3-4}$$

If I_{ex} is the amount of light absorbed by a fluorophore with quantum efficiency η, then the amount of light produced (ignoring secondary absorption) is:

$$I_{em} = (I_0 - I_{ex})\eta = I_0\left(1 - e^{-\mu_{aF} x}\right)\eta \approx I_0 \eta \mu_{aF} x \qquad \textbf{Eq 3-5}$$

When a change in fluorescence concentration c_F occurs (given by a change in μ_{aF}) the fractional change in emitted light will be:

$$\frac{I_{em}(t)}{I_{em}(t=0)} = \frac{I_0 \eta \mu_{aF}(t) x}{I_0 \eta \mu_{aF}(t=0) x} = \frac{\mu_{aF}(t)}{\mu_{aF}(t=0)} = \frac{c_F(t)}{c_F(t=0)} \qquad \textbf{Eq 3-6}$$

Which is independent of path length x. It is tempting then to interpret the differences in the amplitudes in the early peak and late decay of the fluorescence signal as evidence for depth-dependence in the fluorescence concentration changes of FAD; for example that larger fractional changes are occurring in the superficial layers that are being more probed by narrow source-detector separations. However, numerous other factors are impacting this early pilot data, such as the secondary effects of changing absorption in the brain, photobleaching, or the effects of shadowing from large vessels as described above. The trend in the later fluorescence signals could be accounted for by stronger photobleaching in the most superficial layers, owing to the much higher levels of light exposure that they experience during scanning. Absorption changes

could also account for the reduction in signal amplitude for wider source-detector separations following Equation 3-3 above. Since the blue reflectance decreases initially, the fluorescence signal would be attenuated more in the wider separations, decreasing the detected fluorescence intensity, while during the later phase, the blue reflectance increases, denoting a reduction in absorption, which would cause an increase in detected fluorescence in the wider separation detectors. We conclude that additional analysis is required that fully models both the spatiotemporally evolving fluorescence and absorption changes in the brain for proper interpretation of this data.

3.2.4 Discussion

This chapter detailed the application of our second generation LOT system in a bench-top configuration for imaging the living rat brain. We explored whether it was possible to simultaneously capture changes in absorption at 488 nm and 638 nm alongside green intrinsic fluorescence from FAD, excited by the same 488 nm laser. The results of this pilot study were very positive, suggesting that FAD can be measured with sufficient signal to noise to map the location and extract the temporal behavior of the response in parallel with hemodynamic changes that had different spatiotemporal properties.

Several factors affected the data shown that could be improved upon in future studies. Firstly, we know from our initial in-vitro measurements of FAD excitation and emission that our 488 nm laser is not optimal for exciting FAD. Use of a 473 nm laser would more efficiently excite FAD, providing improved signal to noise with respect to photodamage. We also acquired the data shown with our multi-line dichroic filter in place, which is designed to pass returning 532 nm light to the absorption detection arm of the system. Replacing this dichroic with a two-line

dichroic that passes only 473 / 488 nm and 638 nm would allow more of the peak FAD emission light to be reflected to the fluorescence arm, which would provide improved signal to noise with no change in the level of photodamage. Furthermore, the data shown was only an average of 10 repeated stimulus runs, whereas in previous studies, we have used average of over 100 runs. The current LOT system was only configured to acquire a single run at a time, making duty cycles between scans longer than necessary. This prolonged scanning period meant that fewer scan could be acquired within the window of time that the rats had good systemic physiology and were responding well to stimulus. Modifications to the LOT software could readily allow 10 stimulus runs to be acquired within one sequence, improving the amount of averaging that could be performed. The scanning speed chosen for these studies was limited only by disk-write speed, not hardware or signal, so faster frame rates can also be achieved with only small modifications to the current system.

Photobleaching is an important problem identified in these pilot data. The hardware modifications above will allow for improved excitation and detection efficiency, which should lead to improvements. Further experiments are required to explore additional strategies such as modifying scan patterns to reduce the density of measurements (depending on the data required) or to visit slightly different locations in successive scans. PCA showed promise for removing the impact of the baseline trends, although investigations of this analysis are also required to ensure that results are not being misinterpreted. Independent component analysis (ICA) could be explored as an alternative, more robust approach [117, 118]. More complex modeling and 3D reconstruction methods are likely to be required to allow more accurate.

This demonstration that the newest bench-top configuration of our LOT system can capture the dynamics of very weak autofluorescence in the brain opens up a wide range of additional studies that could be performed. These could include simultaneously capturing the depth-dependent dynamics of calcium sensitive dyes in parallel with hemodynamic changes (analogous to Figure 4). Since calcium sensitive dye fluorescence is much stronger, photobleaching would be less of an issue, with the only challenge to overcome being the uniformity of staining that can be achieved, since most calcium sensitive dyes must be cortically injected. A growing range of transgenic mice are now being developed that have active fluorescent proteins that are responsive to environmental changes including intracellular calcium, but also compounds such as glucose. Our results suggest that LOT could potentially capture the depth-resolved dynamics of a wide range of fluorescent reporters, alongside parallel changes in absorption. The importance of FAD in oxidative metabolism also makes it a promising intrinsic target for cancer staging and delineation [119, 120]. Our demonstration that LOT can capture FAD fluorescence, and small dynamic changes in FAD related to changes in oxidative metabolism suggests that using LOT to map FAD for delineation of lesions, for example in the cervix, oral mucosa or intestine is a possibility.

Chapter 4

Summary and Future Directions

This thesis was devoted to the development, testing, evaluation and applications of laminar optical tomography. The purpose was to provide substantial improvements to the first generation system through novel design and implementation in order provide a tool that offers unique measurements of biological tissues *in vivo*. We then sought to utilize the new capabilities of the system to study skin cancer lesions and the rodent brain.

The system resulting from this work is superior to the first generation LOT system owing to improvements that include faster speed, higher measurement density, and simultaneous multispectral and fluorescence capabilities. The newly developed system is fast compared to any other tomography-like system. When compared to the first generation system, the system presented here can easily acquire the same data set at 6x the speed without having to push any parameters to their limits. An additional advantage of the new system is that multispectral and fluorescence data are collect at the exact same time which has two important implications: (1) spectroscopic measurements can be acquired without adversely affecting imaging frame rate and (2) imaging multiple contrast sources allows for a wider range of experiments with which to study a biological system.

The clinical skin study presented in Section 3.1.3 required us to overcome many challenges associated with setting up a trial and developing a clinically compatible system. While the data

collected during the clinical study was unable to provide a definitive evaluation of utility of LOT measurements for skin cancer screening or surgical planning, valuable lessons were learned that can be considered for a *clinical* LOT system. A clinical system would greatly benefit from miniaturization. Hand held confocal microscopes are now commercially available. Given the similar instrumentation geometries, miniaturized hand held LOT seems feasible. Another future direction for a clinical LOT implementation that offers great promise is the use of contact LED/photdetector arrays that can serve as both source and detectors [121]. Such a configuration would eliminate most of the optical components in the current system including the lasers offering the potential to be a very cost effective implementation.

The pilot studies investigating LOT imaging of FAD and hemodynamics in the rat brain only touch upon the surface of the possible research applications of LOT. The data presented was pilot data that would likely be improved by optimizing the excitation wavelength. The possibility of imaging other sources of fluorescence contrast such as calcium sensitive dyes in addition to the hemodynamic measures makes LOT a powerful tool for functional brain imaging.

Since its development in 2004, LOT has been used to investigate a range of tissues including rat brain [1, 67], rat heart [68], rat spinal cord, and now human skin. The value of LOT imaging has been recognized by several other research groups who have implemented LOT [122] and multimodal LOT systems [54]. There are many more potential applications in which LOT could be of use owing to the relatively unexplored region in which LOT images (the space in which light propagation is not ballistic and not diffuse). The advances in LOT imaging and applications described in this thesis will contribute to the ongoing needs of a growing LOT user base as they explorer additional implementations and applications of LOT.

References

1. Hillman, E.M.C., et al., *Laminar optical tomography: demonstration of millimeter-scale depth-resolved imaging in turbid media.* Opt Lett, 2004. **29**(14): p. 1650-2.

2. de Leeuw, J., et al., *Fluorescence detection and diagnosis of non-melanoma skin cancer at an early stage.* Lasers Surg Med, 2009. **41**(2): p. 96-103.

3. Stenquist, B., et al., *Bispectral fluorescence imaging of aggressive basal cell carcinoma combined with histopathological mapping: a preliminary study indicating a possible adjunct to Mohs micrographic surgery.* Br J Dermatol, 2006. **154**(2): p. 305-9.

4. Kiesslich, R., et al., *Confocal laser endoscopy for diagnosing intraepithelial neoplasias and colorectal cancer in vivo.* Gastroenterology, 2004. **127**(3): p. 706-13.

5. Dunbar, K.B., et al., *Confocal laser endomicroscopy in Barrett's esophagus and endoscopically inapparent Barrett's neoplasia: a prospective, randomized, double-blind, controlled, crossover trial.* Gastrointest Endosc, 2009. **70**(4): p. 645-54.

6. Kiesslich, R., et al., *In vivo histology of Barrett's esophagus and associated neoplasia by confocal laser endomicroscopy.* Clin Gastroenterol Hepatol, 2006. **4**(8): p. 979-87.

7. Haxel, B.R., et al., *Confocal endomicroscopy: a novel application for imaging of oral and oropharyngeal mucosa in human.* Eur Arch Otorhinolaryngol. **267**(3): p. 443-8.

8. Schwarz, R.A., et al., *Noninvasive evaluation of oral lesions using depth-sensitive optical spectroscopy.* Cancer, 2009. **115**(8): p. 1669-1679.

9. Tan, J., et al., *Detection of cervical intraepithelial neoplasia in vivo using confocal endomicroscopy.* BJOG, 2009. **116**(12): p. 1663-70.

10. Corlu, A., et al., *Diffuse optical tomography with spectral constraints and wavelength optimization.* Appl Opt, 2005. **44**(11): p. 2082-93.

11. Prahl, S.A., *Online resource: http://omlc.ogi.edu/spectra/hemoglobin/summary.html.*

12. Jobsis, F.F., *Noninvasive, infrared monitoring of cerebral and myocardial oxygen sufficiency and circulatory parameters.* Science, 1977. **198**(4323): p. 1264-7.

13. Brenner, M. and V.J. Hearing, *The protective role of melanin against UV damage in human skin.* Photochem Photobiol, 2008. **84**(3): p. 539-49.

14. Mourant, J.R., et al., *Light scattering from cells: the contribution of the nucleus and the effects of proliferative status.* J Biomed Opt, 2000. **5**(2): p. 131-7.

15. Mourant, J.R., et al., *Mechanisms of light scattering from biological cells relevant to noninvasive optical-tissue diagnostics.* Appl Opt, 1998. **37**(16): p. 3586-93.

16. Backman, V., et al., *Measuring cellular structure at submicrometer scale with light scattering spectroscopy.* Selected Topics in Quantum Electronics, IEEE Journal of, 2001. **7**(6): p. 887-893.

17. Hebden, J.C., et al., *Simultaneous reconstruction of absorption and scattering images by multichannel measurement of purely temporal data.* Opt Lett, 1999. **24**(8): p. 534-6.

18. Rector, D.M., et al., *Spatio-temporal mapping of rat whisker barrels with fast scattered light signals.* Neuroimage, 2005. **26**(2): p. 619-27.

19. Cheong, W.F., S.A. Prahl, and A.J. Welch, *A Review of the Optical Properties of Biological Tissues.* IEEE J. Quantum Electron., 1990. **26**: p. 2166-2185.

20. Richards-Kortum, R. and E. Sevick-Muraca, *Quantitative optical spectroscopy for tissue diagnosis.* Annu Rev Phys Chem, 1996. **47**: p. 555-606.

21. Gryczynski, Z., I. Gryczynski, and J.R. Lakowicz, *Fluorescence-sensing methods.* Methods Enzymol, 2003. **360**: p. 44-75.

22. Patterson, G.H., et al., *Separation of the glucose-stimulated cytoplasmic and mitochondrial NAD(P)H responses in pancreatic islet beta cells.* Proc Natl Acad Sci U S A, 2000. **97**(10): p. 5203-7.

23. Esmaeili Iv, A., et al., *Imaging Techniques for the In Vivo Diagnosis of Melanoma.* Seminars in Cutaneous Medicine and Surgery, 2008. **27**(1): p. 2-10.

24. McCaslin, A.F., et al., *In vivo 3D morphology of astrocyte-vasculature interactions in the somatosensory cortex: implications for neurovascular coupling.* J Cereb Blood Flow Metab, 2011. **31**(3): p. 795-806.

25. Zipfel, W.R., R.M. Williams, and W.W. Webb, *Nonlinear magic: multiphoton microscopy in the biosciences.* Nat Biotechnol, 2003. **21**(11): p. 1369-77.

26. Wang, X., et al., *Astrocytic Ca2+ signaling evoked by sensory stimulation in vivo.* Nat Neurosci, 2006. **9**(6): p. 816-823.

27. Winship, I.R., N. Plaa, and T.H. Murphy, *Rapid Astrocyte Calcium Signals Correlate with Neuronal Activity and Onset of the Hemodynamic Response In Vivo.* J. Neurosci., 2007. **27**(23): p. 6268-6272.

28. Drexler, W., *Ultrahigh-resolution optical coherence tomography.* J Biomed Opt, 2004. **9**: p. 47-74.

29. Costa, R.A., et al., *Retinal assessment using optical coherence tomography.* Progress in Retinal and Eye Research, 2006. **25**(3): p. 325-353.

30. Townsend, K.A., G. Wollstein, and J.S. Schuman, *Imaging of the retinal nerve fibre layer for glaucoma.* British Journal of Ophthalmology, 2009. **93**(2): p. 139-143.

31. Zhang, E., J. Laufer, and P. Beard, *Backward-mode multiwavelength photoacoustic scanner using a planar Fabry-Perot polymer film ultrasound sensor for high-resolution three-dimensional imaging of biological tissues.* Applied Optics, 2008. **47**: p. 561-577.

32. Zhang, H.F., K. Maslov, and L.V. Wang, *In vivo imaging of subcutaneous structures using functional photoacoustic microscopy.* Nat Protoc, 2007. **2**(4): p. 797-804.

33. Boas, D.A., et al., *Imaging the body with diffuse optical tomography.* Signal Processing Magazine, IEEE, 2001. **18**(6): p. 57-75.

34. Gibson, A.P., J.C. Hebden, and S.R. Arridge, *Recent advances in diffuse optical imaging.* Phys Med Biol, 2005. **50**(4): p. R1-43.

35. Hielscher, A.H., et al., *Near-infrared diffuse optical tomography.* Dis Markers, 2002. **18**(5-6): p. 313-37.

36. Ntziachristos, V., et al., *Diffuse optical tomography of highly heterogeneous media.* IEEE Trans Med Imaging, 2001. **20**(6): p. 470-8.

37. Pogue, B.W., et al., *Image analysis methods for diffuse optical tomography.* Journal of Biomedical Optics, 2006. **11**(3): p. 033001-16.

38. Boas, D.A., et al., *Improving the diffuse optical imaging spatial resolution of the cerebral hemodynamic response to brain activation in humans.* Opt Lett, 2004. **29**(13): p. 1506-8.

39. Joseph, D.K., et al., *Diffuse optical tomography system to image brain activation with improved spatial resolution and validation with functional magnetic resonance imaging.* Appl Opt, 2006. **45**(31): p. 8142-51.

40. White, B.R. and J.P. Culver, *Quantitative evaluation of high-density diffuse optical tomography: in vivo resolution and mapping performance.* J Biomed Opt, 2010. **15**(2): p. 026006.

41. Arridge, S.R., *Optical tomography in medical imaging.* Inverse Problems, 1999. **15**: p. 41-93.

42. Zeff, B.W., et al., *Retinotopic mapping of adult human visual cortex with high-density diffuse optical tomography.* Proceedings of the National Academy of Sciences, 2007. **104**(29): p. 12169-12174.

43. Franceschini, M.A., et al., *On-line optical imaging of the human brain with 160-ms temporal resolution.* Optics Express., 2000. **6**(3): p. 49-57.

44. Schmitz, C.H., et al., *Dynamic studies of small animals with a four-color DOT imager.* Rev. Sci. Instrum, 2005. **76**(9): p. 094302.

45. Dunn, A.K. and D.A. Boas, *Transport-based image reconstruction in turbid media with small source–detector separations.* Opt. Lett., 2000. **25**(24): p. 1777-1779.

46. Wang, L.-H., S.L. Jacques, and L.-Q. Zheng, *MCML - Monte Carlo modeling of photon transport in multi-layered tissues.* Computer Methods and Programs in Biomedicine, 1995. **47**: p. 131-146.

47. Kak, A.C. and M. Slaney, *Principles of computerized tomographic imaging*. 1987, New York: IEEE Press.

48. Arridge, S.R., M. Cope, and D.T. Delpy, *The theoretical basis for the determination of optical pathlengths in tissue: temporal and frequency analysis.* Phys Med Biol, 1992. **37**(7): p. 1531-60.

49. Wang, L.V. and S.L. Jacques, *Source of error in calculation of optical diffuse reflectance from turbid media using diffusion theory.* Comput Methods Programs Biomed, 2000. **61**(3): p. 163-70.

50. Hillman, E.M.C., et al., *Laminar Optical Tomography: demonstration of millimeter-scale depth-resolved imaging in turbid media.* Opt. Lett., 2004. **29**(14): p. 1650-1652.

51. Hillman, E.M.C., et al., *Laminar optical tomography: high-resolution 3D functional imaging of superficial tissues.* Proc. SPIE (Medical Imaging), 2006. **Vol. 6143**: p. 61431M.

52. Hillman, E.M.C., et al., *Depth-resolved optical imaging of transmural electrical propagation in perfused heart.* Optics Express, 2007. **15**(26): p. 17827-17841.

53. Hillman, E.M.C., et al., *Depth-resolved Optical Imaging and Microscopy of Vascular Compartment Dynamics During Somatosensory Stimulation.* Neuroimage, 2007. **35**(1): p. 89-104.

54. Yuan, S., et al., *Three-dimensional coregistered optical coherence tomography and line-scanning fluorescence laminar optical tomography.* Opt Lett, 2009. **34**(11): p. 1615-7.

55. Hillman, E.M.C., et al., *Calibration techniques and datatype extraction for time-resolved optical tomography.* Rev. Sci. Instrum., 2000. **71**(9): p. 3415-3427.

56. Hillman, E.M.C., et al., *Differential imaging in heterogeneous media: limitations of linearization assumptions in optical tomography.* Proc SPIE., 2001. **4250**: p. 327-338.

57. Hielscher, A.H., A.D. Klose, and K.M. Hanson, *Gradient-based iterative image reconstruction scheme for time-resolved optical tomography.* IEEE Trans. Med. Imag., 1999. **18**: p. 262-271.

58. Arridge, S.R. and W. R. B. Lionheart, *Nonuniqueness in diffusion-based optical tomography.* Opt. Lett., 1998. **23**: p. 882 -884.

59. Burgess, S.A., et al., *Simultaneous multiwavelength laminar optical tomography.* Opt Lett, 2008. **33**(22): p. 2710-2.

60. Klose, A.D. and A.H. Hielscher, *Iterative reconstruction scheme for optical tomography based on the equation of radiative transfer.* Med Phys, 1999. **26**(8): p. 1698-707.

61. Ren, K., et al., *Algorithm for solving the equation of radiative transfer in the frequency domain.* Opt Lett, 2004. **29**(6): p. 578-80.

62. Gonzalez-Rodriguez, P., A.D. Kim, and M. Moscoso, *Reconstructing a thin absorbing obstacle in a half space of tissue.* JOSA A, 2007. **24**: p. 3456-3466.

63. Gonzalez-Rodriguez, P. and A.D. Kim, *Reflectance optical tomography in epithelial tissues.* Inverse Problems, 2009. **25**: p. 015001.

64. Wang, L., S.L. Jacques, and L. Zheng, *MCML--Monte Carlo modeling of light transport in multi-layered tissues.* Comput Methods Programs Biomed, 1995. **47**(2): p. 131-46.

65. Hyatt, C.J., et al., *Reconstructing subsurface electrical wave orientation from cardiac epi-fluorescence recordings: Monte Carlo versus diffusion approximation.* Opt Express, 2008. **16**(18): p. 13758-72.

66. Hillman, E.M.C. and S.A. Burgess, *Sub-millimeter resolution 3D optical imaging of living tissue using laminar optical tomography.* Laser & Photonics Review, 2009. **3**(1-2): p. 159-179.

67. Hillman, E.M.C., et al., *Depth-resolved optical imaging and microscopy of vascular compartment dynamics during somatosensory stimulation.* Neuroimage, 2007. **35**(1): p. 89-104.

68. Hillman, E.M.C., et al., *Depth-resolved optical imaging of transmural electrical propagation in perfused heart.* Opt Express, 2007. **15**(26): p. 17827-41.

69. Semrock. *Typical Measured Spectrum of Semrock Di01-T488/532/638*. Available from: http://www.semrock.com/_ProductData/Spectra/Di01-T488_532_638_spectrum.txt.

70. Flock, S.T., et al., *Optical properties of Intralipid: a phantom medium for light propagation studies.* Lasers Surg Med, 1992. **12**(5): p. 510-9.

71. van Staveren, H.J., et al., *Light scattering in Intralipid-10% in the wavelength range of 400-1100 nm.* Appl Opt, 1991. **30**(31): p. 4507-14.

72. Lualdi, M., et al., *Optical devices used for image analysis of pigmented skin lesions: a proposal for quality assurance protocol using tissue-like phantoms.* Phys Med Biol, 2006. **51**(23): p. N429-40.

73. Dunn, A. and D. Boas, *Transport-based image reconstruction in turbid media with small source-detector separations.* Opt Lett, 2000. **25**(24): p. 1777-9.

74. Bevilacqua, F., et al., *In vivo local determination of tissue optical properties: applications to human brain.* Appl Opt, 1999. **38**(22): p. 4939-50.

75. Sung, K.B., et al., *Fiber-optic confocal reflectance microscope with miniature objective for in vivo imaging of human tissues.* IEEE Trans Biomed Eng, 2002. **49**(10): p. 1168-72.

76. Juškattis, R., T. Wilson, and T.F. Watson, *Real-time white light reflection confocal microscopy using a fibre-optic bundle.* Scanning, 1997. **19**(1): p. 15-19.

77. Allard, F.C., *Fiber optics handbook : for engineers and scientists*. Optical and electro-optical engineering series. 1990, New York: McGraw-Hill. 549 p. in various pagings.

78. Hillman, E.M.C. and S.A. Burgess, *Sub-millimeter resolution 3D optical imaging of living tissue using laminar optical tomography.* Laser Photon Rev, 2009. **3**(1-2): p. 159-179.

79. Juscaronkattis, R., T. Wilson, and T.F. Watson, *Real-time white light reflection confocal microscopy using a fibre-optic bundle.* Scanning, 1997. **19**(1): p. 15-19.

80. American Cancer Society. *Cancer Facts & Figures*. 2010; Available from: http://www.cancer.org/acs/groups/content/@nho/documents/document/acspc-024113.pdf.

81. Jimbow, K., et al., *Some aspects of melanin biology: 1950-1975.* J Invest Dermatol, 1976. **67**(1): p. 72-89.

82. Marks, M.S. and M.C. Seabra, *The melanosome: membrane dynamics in black and white.* Nat Rev Mol Cell Biol, 2001. **2**(10): p. 738-48.

83. Freinkel, R.K. and D. Woodley, *The biology of the skin*. 2001, New York: Parthenon Pub. Group. 432 p.

84. Nouri, K., *Skin Cancer*. 2007, Blacklick, OH, USA: McGraw-Hill.

85. Kumar, V., et al., *Robbins and Cotran pathologic basis of disease*. 7th ed. 2005, Philadelphia: Elsevier Saunders. xv, 1525 p.

86. National Cancer Institute, *Surveillance Epidemiology and End Results Cancer Statistics Review 1975-2008*.

87. Armstrong, B.K. and A. Kricker, *How much melanoma is caused by sun exposure?* Melanoma Res, 1993. **3**(6): p. 395-401.

88. Tierney, E.P. and C.W. Hanke, *Cost effectiveness of Mohs micrographic surgery: review of the literature.* J Drugs Dermatol, 2009. **8**(10): p. 914-22.

89. Breslow, A., *Thickness, cross-sectional areas and depth of invasion in the prognosis of cutaneous melanoma.* Ann Surg, 1970. **172**(5): p. 902-8.

90. Clark, W.H., Jr., et al., *The histogenesis and biologic behavior of primary human malignant melanomas of the skin.* Cancer Res, 1969. **29**(3): p. 705-27.

91. Rass, K. and W. Tilgen, *Treatment of Melanoma and Nonmelanoma Skin Cancer*, in *Sunlight, Vitamin D and Skin Cancer*. 2008. p. 296-318.

92. Sober, A.J., et al., *Guidelines of care for primary cutaneous melanoma.* J Am Acad Dermatol, 2001. **45**(4): p. 579-86.

93. Benelli, C., et al., *The dermoscopic versus the clinical diagnosis of melanoma.* Eur J Dermatol, 1999. **9**(6): p. 470-6.

94. Chen, C.S., et al., *Multimodal in vivo optical imaging, including confocal microscopy, facilitates presurgical margin mapping for clinically complex lentigo maligna melanoma.* Br J Dermatol, 2005. **153**(5): p. 1031-6.

95. Marghoob, A.A., et al., *Instruments and new technologies for the in vivo diagnosis of melanoma.* J Am Acad Dermatol, 2003. **49**(5): p. 777-97; quiz 798-9.

96. Scope, A., et al., *In vivo reflectance confocal microscopy of shave biopsy wounds: feasibility of intraoperative mapping of cancer margins.* Br J Dermatol, 2010. **163**(6): p. 1218-28.

97. Gambichler, T., et al., *In vivo optical coherence tomography of basal cell carcinoma.* J Dermatol Sci, 2007. **45**(3): p. 167-73.

98. Mogensen, M., et al., *In vivo thickness measurement of basal cell carcinoma and actinic keratosis with optical coherence tomography and 20-MHz ultrasound.* Br J Dermatol, 2009. **160**(5): p. 1026-33.

99. Gambichler, T., et al., *Preoperative ultrasonic assessment of thin melanocytic skin lesions using a 100-MHz ultrasound transducer: a comparative study.* Dermatol Surg, 2007. **33**(7): p. 818-24.

100. Marmur, E.S., et al., *Use of high-frequency, high-resolution ultrasound before Mohs surgery.* Dermatol Surg, 2010. **36**(6): p. 841-7.

101. Abbas, Q., I.F. Garcia, and M. Rashid, *Automatic skin tumour border detection for digital dermoscopy using a new digital image analysis scheme.* Br J Biomed Sci, 2010. **67**(4): p. 177-83.

102. Lorber, A., et al., *Correlation of image analysis features and visual morphology in melanocytic skin tumours using in vivo confocal laser scanning microscopy.* Skin Res Technol, 2009. **15**(2): p. 237-41.

103. Lazova, R. and J.M. Pawelek, *Why do melanomas get so dark?* Experimental Dermatology, 2009. **18**(11): p. 934-938.

104. Barnhill, R.L., et al., *Angiogenesis and tumor progression of melanoma. Quantification of vascularity in melanocytic nevi and cutaneous malignant melanoma.* Lab Invest, 1992. **67**(3): p. 331-7.

105. Trotter, M.J. and V.A. Tron, *Dermal vascularity in lentigo maligna.* The Journal of Pathology, 1994. **173**(4): p. 341-345.

106. Hillman, E.M., *Optical brain imaging in vivo: techniques and applications from animal to man.* J Biomed Opt, 2007. **12**(5): p. 051402.

107. Blood, A.J., N. Pouratian, and A.W. Toga, *Temporally staggered forelimb stimulation modulates barrel cortex optical intrinsic signal responses to whisker stimulation.* J Neurophysiol, 2002. **88**(1): p. 422-37.

108. Grinvald, A., et al., *Functional architecture of cortex revealed by optical imaging of intrinsic signals.* Nature, 1986. **324**(6095): p. 361-4.

109. Vanzetta, I., R. Hildesheim, and A. Grinvald, *Compartment-resolved imaging of activity-dependent dynamics of cortical blood volume and oximetry.* J Neurosci, 2005. **25**(9): p. 2233-44.

110. Bouchard, M.B., et al., *Ultra-fast multispectral optical imaging of cortical oxygenation, blood flow, and intracellular calcium dynamics.* Opt Express, 2009. **17**(18): p. 15670-8.

111. Ramón y Cajal, S., *Histology of the nervous system of man and vertebrates*. History of neuroscience. 1995, New York: Oxford University Press.

112. Shibuki, K., et al., *Dynamic imaging of somatosensory cortical activity in the rat visualized by flavoprotein autofluorescence.* J Physiol, 2003. **549**(Pt 3): p. 919-27.

113. Silva, A.C. and A.P. Koretsky, *Laminar specificity of functional MRI onset times during somatosensory stimulation in rat.* Proc Natl Acad Sci U S A, 2002. **99**(23): p. 15182-7.

114. Attwell, D., et al., *Glial and neuronal control of brain blood flow.* Nature, 2010. **468**(7321): p. 232-43.

115. Fox, P.T. and M.E. Raichle, *Focal physiological uncoupling of cerebral blood flow and oxidative metabolism during somatosensory stimulation in human subjects.* Proc Natl Acad Sci U S A, 1986. **83**(4): p. 1140-4.

116. Hillman, E.M. and A. Moore, *All-optical anatomical co-registration for molecular imaging of small animals using dynamic contrast.* Nat Photonics, 2007. **1**(9): p. 526-530.

117. Liu, X., et al., *Unmixing Dynamic Fluorescence Diffuse Optical Tomography Images With Independent Component Analysis.* IEEE Trans Med Imaging, 2011.

118. Liu, X., et al., *Principal component analysis of dynamic fluorescence diffuse optical tomography images.* Opt Express, 2010. **18**(6): p. 6300-14.

119. Skala, M.C., et al., *In vivo multiphoton microscopy of NADH and FAD redox states, fluorescence lifetimes, and cellular morphology in precancerous epithelia.* Proc Natl Acad Sci U S A, 2007. **104**(49): p. 19494-9.

120. Levitt, J.M., et al., *Intrinsic fluorescence and redox changes associated with apoptosis of primary human epithelial cells.* J Biomed Opt, 2006. **11**(6): p. 064012.

121. Cox, M.P., et al., *LED-Based Optical Device for Chronic In Vivo Cerebral Blood Volume Measurement.* IEEE Transactions on Electron Devices, 2010. **57**: p. 174-177.

122. Ouakli, N., et al., *Laminar optical tomography of the hemodynamic response in the lumbar spinal cord of rats.* Opt Express, 2010. **18**(10): p. 10068-77.